Alma Mater Studiorum – Università di Bologna

DOTTORATO DI RICERCA IN FISICA

Ciclo XXIII

Settore scientifico-disciplinare:
Scienze matematiche fisiche ed astronomiche

FIS/07: FISICA APPLICATA

Ph.D. Thesis

Performance evaluation of detectors for digital radiography

by:

Stefano Rivetti di Val Cervo

Coordinator:

Prof. Fabio Ortolani

Advisor:

Dott. Nico Lanconelli

March, 2011

FOREWARD

The research this thesis is based on has been performed during the last three years. I become interested in digital detectors at the end of the degree course, in 2000, and since then I have worked, most of the time, in a hospital frame, mainly in a Medical Physics Department: for this reason, this paper is characterized by a well defined application oriented format and the results presented issue from a particular attention paid to the cost/benefit ratio of the systems and to the analysis of its procedures.

This work has been accomplished under the continuous supervision of Dr. Nico Lanconelli to which I am greatly indebted for his high human and professional guidance and for being so patient with me: I learned a lot.

I wish to express my gratitude to Dr. G. Borasi for his guidance during all these years and for his precious encouragement and advices and to Prof. D. Bollini for the imprinting he gave me on medical technologies.

Finally, I would like to thank the institutions that, during these years, have provided me intellectuals and financial supports: they include University of Bologna, AUSL of Modena, Ospedale di Sassuolo S.p.A., FUJIFILM Medical Systems S.p.A. and “The FAMILY”.

Bologna, march 2011 Stefano Rivetti

ABSTRACT

To date the hospital radiological workflow is completing a transition from analog to digital technology. Since the X-rays digital detection technologies have become mature, hospitals are trading on the natural devices turnover to replace the conventional screen film devices with digital ones. The transition process is complex and involves not just the equipment replacement but also new arrangements for image transmission, display (and reporting) and storage.

This work is focused on 2D digital detector's characterization with a concern to specific clinical application; the systems features linked to the image quality are analyzed to assess the clinical performances, the conversion efficiency, and the minimum dose necessary to get an acceptable image.

The first section overviews the digital detector technologies focusing on the recent and promising technological developments.

The second section contains a description of the characterization methods considered in this thesis categorized in physical, psychophysical and clinical; theory, models and procedures are described as well.

The third section contains a set of characterizations performed on new equipments that appears to be some of the most advanced technologies available to date.

The fourth section deals with some procedures and schemes employed for quality assurance programs.

KEYWORD: digital radiography, digital mammography, physical characterization, flat panel detector, photostimulable phosphor

Contents

OVERVIEW

This thesis will illustrate some methods used in evaluating the physical and the psychophysical performance of digital detectors dedicated to radiography and mammography.

To assess the image quality of the various systems, spatial resolution and noise properties can be evaluated, using metrics such as the Modulation Transfer Function (MTF), Noise Power Spectra (NPS), Noise Equivalent Quanta (NEQ), and Detective Quantum Efficiency (DQE). Image quality of different systems may be characterized using these objective measures, however medical diagnosis also involves the perception by the observer.

Since an image is, by definition, a means for visually representing the clinical information captured by the equipment, at some stage quality must be based on the judgment of a human observer. A more direct image-based method of evaluating overall system performance is by using contrast-detail (CD) phantoms. These phantoms contain test objects of different size and contrast and are traditionally used to determine the boundary between visible and invisible objects represented by the imaging system.

A good quality image is of major importance to assure an accurate diagnosis and this is – in general – determined by three primary physical image quality parameters: contrast, spatial resolution and noise. These quality parameters can be evaluated by objective image quality measurements such as signal-to-noise ratio (SNR), MTF and NPS. Together they form a basis for description of image quality which encompasses the three primary physical image quality parameters. These factors contribute to the measurement of DQE which is well established as the most suitable parameter for describing the imaging performance of an X-ray digital imaging device [1,2,3]. DQE is the measure of the combined effect of the noise and contrast performance of an imaging system, expressed as a function of object detail.

Parameters such as NEQ and DQE have the potential for providing objective assessments of imaging performance for an image as viewed by an ideal observer. Measurements of this type allow objective comparisons to be made between different systems. More research is required to establish mathematical relationships between these measures of performance and the requirements for clinical examinations. Some studies have investigated the relationship between physical performance characteristics (MTF, NPS, DQE), and psychophysical performance (such as those derived from CD analysis) [4,5].

The relationship between the results of physical measurements, phantom evaluations and clinical performance is not fully understood. Object detectability could be directly linked to the DQE, although the response of the human eye, the system noise, and the variation of the DQE as a function of the exposure need to be taken into account.

Image quality could be evaluated combining the physical characteristics of the imaging system, the overall system performance and observer performance studies. Table 1 shows a wide spectrum of methods for image quality evaluation. Some of these methods focuses on the physical characteristics of the imaging systems and others on subjective assessment of image quality; some are used for the whole imaging chain including the human observer (observer performance) while others are used for parts of the system (typically physical measurements).

To discuss image quality, “quality” needs to be defined. Images are used for various purposes and this suggests that, in order to define the concept of image quality in a reasonable manner, the underlying task of using the image should be specified: an image can be defined to be of "good quality" if it well fulfills its intended task. Image quality then becomes a task-dependent quantity; images ranked by one imaging task will not necessarily rank similarly in another task.

For example, if the visibility of small-sized details is important, imaging system performance at high spatial frequencies may be a more important factor than imaging system performance at low spatial frequencies, and vice versa if the visibility of large, low-contrast objects is required.

Level of ambition	**Investigation**	**Measurement**
Lowest	Radiographic technique	✓ Equipment characteristics ✓ Exposure parameters
	Primary physical characteristics	✓ Contrast ✓ Spatial resolution (MTF) ✓ Signal-to-Noise Ratio (SNR)
	Overall system performance	✓ DQE ✓ Image quality index ✓ Contrast-detail resolution
	Images of anthropomorphic phantoms	✓ ROC ✓ ROC related methods ✓ Visual grading analysis
Highest	Images of patients	✓ ROC ✓ ROC related methods ✓ Visual grading analysis ✓ Image criteria

Table 1. Methods for quality evaluation of diagnostic imaging procedures

Image quality is then not solely dependent on image properties, but also on the detection task, the observer's a-priori information on the task and the observer's ability to use both the prior information and the image information for his decisions. This apparent difficulty cannot be avoided, but it can be dealt with, by specifying the task and the observer in detail.

THESIS STRUCTURE

The thesis is structured in major two parts: in the first one we will describe technologies and methods implemented both - in general radiography and mammography; in second part we will describe the results obtained - during the doctoral work – in the course of experiments on clinical prototype and on new, recently marketed devices.

Clinical details linked to the radiological and mammographic task have been overlook on not overload the reader which on the other side is supposed to be familiar with such matters as the working of a radiographic device, the specificities of breast radiography (mammography), the meaning of “image quality” from a clinical point of view, and the X-ray biological effects.

The work is organized as follows:

Chapter 1 - In this section will be given an overview of digital detectors technologies focusing on the X-rays conversion process and readout methods. It is paid attention on the most recent and promising detector technologies.

Chapter 2 - In this section are described the methods used for detector characterization. The methods are divided in three different categories: physical, psychophysical and clinical. Here are described theory, models and procedures.

Chapter 3 - The third section contains a set of characterizations made on new equipment that represent, up to date, some of the most promising technologies available: that are three characterizations made on new clinical device or clinical prototype (i.e. technologies just marketable but non still completely configured in the clinical workflow) and a clinical comparison between a digital mammographic (CR) unit versus the analog gold standard. In each sub-section the equipment and materials & methods description is limited to the specificity of each experiment since the details are described in the first two chapters of this thesis.

Chapter 4 - In the section are described few procedures and schemes employed for quality assurance programs implemented to guarantee the constancy of a digital detector quality imaging i.e. to verify the best digital images level obtainable through an acceptable patient doses.

PUBLICATIONS

Most of the material presented in this thesis appears in the following publications:

- ✓ Lanconelli N and Rivetti S, "Evaluating the performance of digital mammography systems: physical and psychophysical characterization"; in "Diagnostic and therapeutic breast cancer imaging"; Suri J S, Sree S V, Kwan-Hoong Ng, and Rangayyan R M Editors, SPIE PRESS (2011 – in press)
- ✓ Nitrosi A, Bertolini M, Rivetti S, Botti A, Barani A, Lanconelli N, Borasi G, "Physical characterization of a novel wireless detector for digital radiography", Proc. ECR, Vienna, (2010)
- ✓ Rivetti S, Lanconelli N, "Contrast detail performance analysis in medical displays", Hospital Imaging & Radiology Europe Vol 5 No 2 - Summer (2010)
- ✓ Donini B, Rivetti S, Bertolini M, Lanconelli N and Acchiappati D, "An ImageJ plugin for performing physical analysis on digital systems for medical imaging", Proc ImageJ Conference, Luxembourg, (2010)
- ✓ Lanconelli N, Rivetti S, Bertolini M, Borasi G, Golinelli P, Gallo E "Characterization of a novel clinical unit for full-field digital mammography based on amorphous Selenium and optical switching", Proc. RSNA, Chicago (I), USA, (2009)
- ✓ Nitrosi A, Bertolini M,. Borasi G, Botti A, Barani A, Rivetti S, and Pierotti L, "Application of QC_DR Software for Acceptance Testing and Routine Quality Control of Direct Digital Radiography Systems: Initial Experiences using the Italian Association of Physicist in Medicine Quality Control Protocol," J Digit Imaging (2009)
- ✓ Lanconelli N, Rivetti S, Bertolini M, Golinelli P, Serafini M, Bertolini M, Donini B, "Comparison of human observers and ideal observe reading for contrast detail images", Proc. SIIM, Charlotte (N.C.), USA, (2009)

Not everything from these publications is included here. Some topics were purposely discarded as they were only marginally relevant to the general idea of the presented approach. Instead, here we expand those aspects that are believed to be more useful for a clear understanding of the proposed method. In particular Chapter 3 contains the off prints of the following papers:

- ✓ Rivetti S, Lanconelli N, Bertolini M, Borasi G, Acchiappati D, Burani A, "Comparison of different Computed Radiography systems: physical characterization and contrast detail analysis", Med. Phys. 37 (2), February 2010
- ✓ Rivetti S, Lanconelli N, Bertolini M, Donini B, Burani A, Acchiappati D, "Characterization of a New Flat Panel Detector Based on 1000 um Thick Amorphous Selenium", Proc. RSNA, Chicago (I), USA (2010)

- ✓ Rivetti S, Lanconelli N, Bertolini M, Borasi G, Golinelli P, Gallo E, “Physical and psychophysical characterization of a novel clinical system for digital mammography”, Med. Phys. 36 (11), November 2009
- ✓ Mauri C, Bellelli V, Rivetti S, Lanconelli N, Bertolini M, Nocetti L, Acchiappati D, Gallo E, “Evaluation of a full field digital mammography system with a new dual aSe layer Detector: Optical Switch”, Proc. ECR, Vienna, (2010)
- ✓ Rivetti S, Canossi B, Battista R, Lanconelli N, Vetruccio E, Danielli C, Borasi G, Torricelli P “Physical and clinical comparison between a screen-film system and a dual side reading mammography dedicated computed radiography system”, Acta Radiol (10) 1109-1118 (2009)

GLOSSARY

- **a-Se:** amorphous selenium
- **a-Si:** amorphous silicon
- **AEC (Automatic Exposure Control):** Operation mode of an X-ray machine by which the tube loading is Control (AEC) automatically controlled and terminated when a preset radiation exposure to a dose detector located under the image receptor is reached. Some more sophisticated equipment also allow the automatic selection of tube potential (kV), target and filter materials
- **AGD (Average Glandular Dose):** Reference term (ICRP 1987) for radiation dose estimation from X-(AGD) ray mammography i.e. the average absorbed dose in the glandular tissue in a uniformly compressed breast. AGD value depends on X-ray beam quality (HVL), breast thickness and composition. If breast thickness and composition are not known, AGD can be referred to a standard breast
- **AMA:** Active Matrix Array
- **Breast Compression:** Application of a compression force to the breast during image acquisition. This immobilizes the breast, which limits motion artifacts, and reduces breast thickness, which limits scatter effects and makes breast thickness approximately uniform
- **Compression Paddle:** Thin device (few millimeters) rectangular shaped, made of plastic material (typical PMMA or polycarbonate) that can be positioned parallel to and above the breast table of a mammography apparatus.
- **CCD:** Charge coupled device
- **Contrast threshold**: Contrast level that produces a just visible difference between an object and the background.
- **CR:** Computed Radiography
- **DE:** Detective Efficiency
- **DQE:** Detective Quantum Efficiency
- **DR:** Digital Radiography
- **ESAK (Entrance Surface Air Kerma) or Air KERMA (Air Kinetic Energy Released per unit Mass):** is a measure of the amount of radiation energy, in the unit of joules (J), actually deposited in or absorbed in a unit mass (kg) of air. Therefore, the quantity, kerma, is expressed in the units of J/kg which is also the radiation unit, the Gray (Gy)
- **FFDM:** Full Field Digital Mammography
- **FP:** Flat Panel detector
- **HVL (Half Value Layer):** thickness of absorber which attenuates the air kerma of non-monochromatic X-ray beams by half. The absorber normally used to evaluate HVL of low energy X-ray beams, such as mammography beams, is high purity aluminum (. 99.9%). It should be noticed that a correct measurement of HVL requires ‘good geometry’ conditions (proper distances among source, attenuator and image receptor, collimation and perpendicular incidence at image receptor entrance), rather far from geometry imposed by mammography equipment. Thereby, the HVL measurement is a sort of verification about the compatibility of radiation spectra with standard values measured with calibrated beams. Sometimes is named “radiation quality”
- **Heel effect:** Decreasing optical density measurable on a film in the cathode-anode direction, caused by the non-uniform intensity distribution of the X-ray beam. It is due to the geometric setup of the X-ray tube
- **Image quality:** There is not a definition of image quality univocally accepted. Commonly, it is possible to define quality indices representing the information content of the image; this is often done by test objects including details whose visibility can be quantified by means of proper scoring criteria.
- **MTF:** Modulation Transfer Function
- **NEQ:** Noise Equivalent Quanta
- **NPS:** Noise Power Spectrum
- **OD (Optical density):** Logarithm of the ratio between light intensity produced by a visible light source and perpendicularly incident on a film (Io), and light intensity transmitted by the film (I): OD = log10 (Io/I) Optical density is measured by an instrument named densitometer, that measures transmitted light intensity into an area of the order of mm2. Variations in optical density should be measured along a direction parallel to the major axis of image receptor (perpendicular to cathode-anode direction), to avoid influences by the angular distribution of X-ray intensity (heel-effect).

- **PMMA (Polymethylmethacrylate):** Trade names include Lucite, Perspex and Plexiglas.
- **PMT**: Photomultiplier Tube
- **QA (Quality Assurance):** Quality assurance As defined by the WHO (1982): “All those planned and systematic actions necessary to provide adequate confidence that a structure, system or component will perform satisfactorily in service (ISO 6215-1980). Satisfactory performance in service implies the optimum quality of the entire diagnostic process i.e., the consistent production of adequate diagnostic information with minimum exposure of both patients and personnel”
- **QC (Quality Control):** As defined by the WHO (1982): “The set of operations (programming, coordinating, carrying out) intended to maintain or to improve [..] (ISO 3534-1977). As applied to a diagnostic procedure, it covers monitoring, evaluation, and maintenance at optimum levels of all characteristics of performance that can be defined, measured, and controlled.”
- **ROI (Region of Interest):** Measurement area of optical density whose boundaries can be virtually defined on an image.
- **RSD:** Relative Standard Deviation
- **SID:** Source to Image Distance
- **SNR:** Signal to Noise Ratio
- **TFT:** Thin Film Transistor

1. CHAPTER 1: DETECTOR TECHNOLOGIES

The term digital radiography (DR) refers to any technology that is used to detect, display, archive, and communicate radiographic or mammographic electronic images. Digital radiography encompasses a widespread range of detector technologies that are used for digital X-ray imaging and is commonly named full field digital mammography (FFDM) when used for mammographic application.

Many approaches have been investigated and, up to date, there is a great variability among the detector types used in practical clinical systems - accordingly performance specifications vary widely among different technologies [6]. An outline of the current technologies for DR is shown in Figure 1.

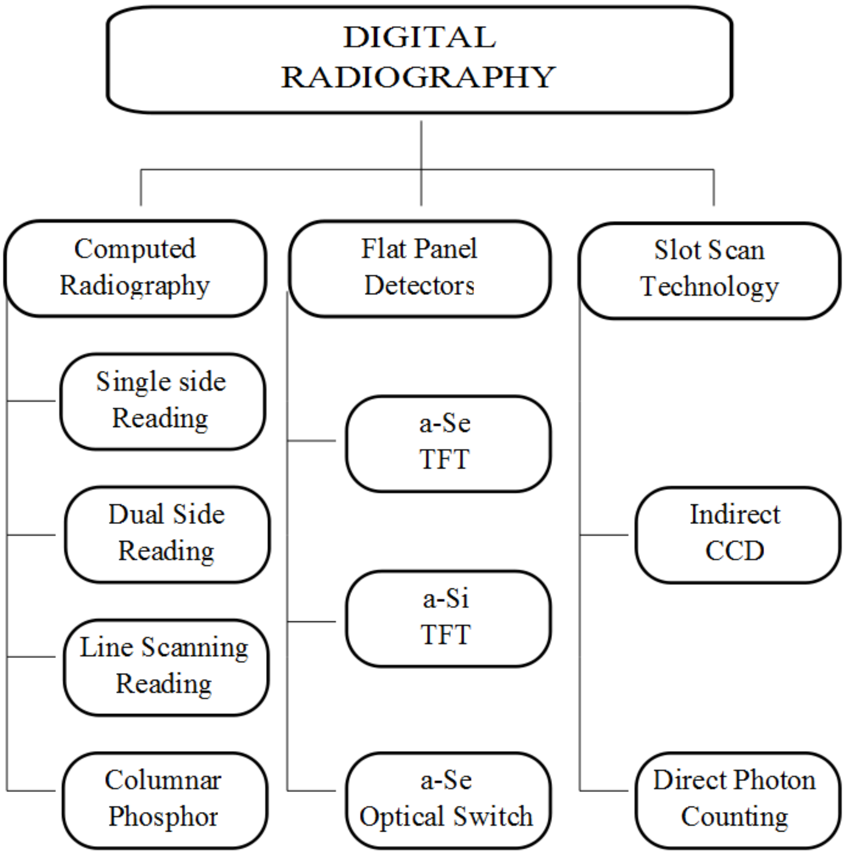

Figure 1. Current approaches to digital radiography.

Digital detectors can be categorized into three major types on the basis of the technologies used [7]:

1) "Removable detector" technologies based on photostimulable phosphor (PSP) plates typically named computed radiography (CR). CR technology is intended to replace the screen film cassette in a conventional screen film system.

2) Flat panel (FP) detectors, which, depending on the mechanism involved in the X-ray detection, can be grouped into direct and indirect conversion. "Direct conversion" is commonly used for the photoconductor type detection; this technology employs a photoconducting layer (such as amorphous selenium layer, a-Se) that converts X-ray energy to

electrons without the intermediate step of scintillation. In these detectors the readout is usually achieved through arrays of thin film transistors (TFT) or in the recent applications through optical switch. "Indirect conversion" detectors are commonly used for the scintillator type detection of X-rays. Indirect conversion FP detectors employ a scintillator as the primary detector of X-rays and a photodetector, such as an amorphous silicon (a-Si), that is optically coupled to the scintillator such as structured thallium activated cesium iodide (CsI-Tl). The readout is commonly achieved through arrays of TFT.

3) Slot-scan systems that use a fan beam geometry and linear detectors. As well as FP detectors, slot-scan systems can be grouped into direct and indirect conversion although the read out technology is typically based on charge couple device (CCD) or photon counting electronics.

1.1. Computed radiography

Computed radiography (CR) technology has many of the advantages of the digital detectors, such as high dynamic range, contrast enhancement, archival and the ability to provide DR FFDM with a conventional system that was originally designed for screen film use. CR is based on photostimulable luminescence [8]: in this technique an image phosphor plate crystals, typically barium fluoro bromide or iodide compound doped with trace amounts of europium ($BaFBr:Eu^{2+}$, $BaFI:Eu^{2+}$), is laid on a suitable substrate in the form of a portable cassette.

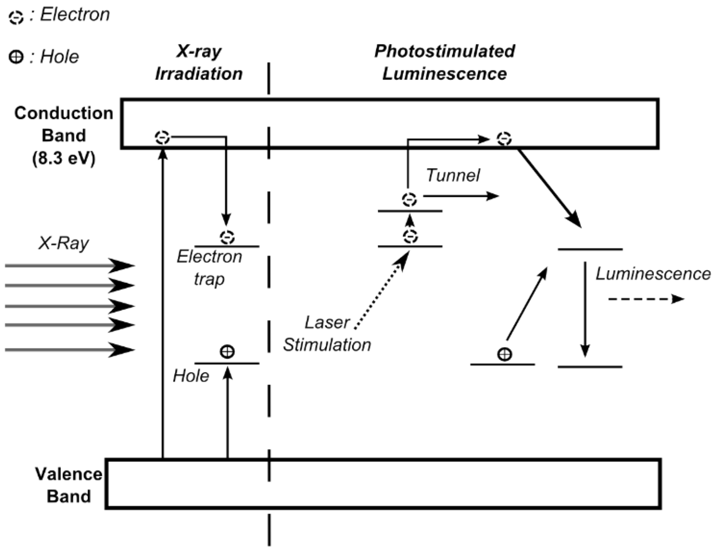

Figure 2. Simplified energy levels diagram illustrating the photostimulated luminescence mechanism.

During exposure to X-rays, the bromine vacancies act as traps for the electrons that migrate to the conduction band of the crystal as a result of X-ray interaction with the phosphor. A latent image remains stable for several hours, which is due to the trapping effect of the electrons, and the number of trapped electrons is proportional to the X-ray exposure at any particular location of the image phosphor plate (IP). As schematically shown in Figure 2 this stored signal can be read out stimulating the image phosphor plate with a laser beam (typically red light) that scans the entire image phosphor plate point by point. During this stimulation, electrons return to their original resting state by emitting light near the blue region (photostimulated luminescence). The amount of emitted light can be detected by an optical collecting system and a photomultiplier tube (PMT) thereby generating an image (Figure 3).

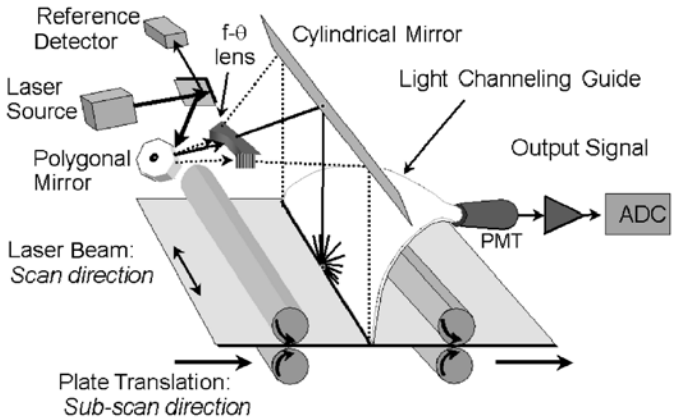

Figure 3. A scheme of the readout process of a photostimulable image plate. Components include the stimulating laser source, a beam splitter, oscillating beam deflector lens, stationary reflecting mirror, light collection guide, photomultiplier tube, and analog to digital converter system.

A filter in the optical chain prevents the stimulating light from interfering with the measurement. The time at which the laser beam strikes a given location on the screen gives the coordinates of each image location. The spatial sampling is determined by the size of the laser spot and the distance between sample pitch.

The readout of computed radiography plates presents considerable challenges when high spatial resolution and detective quantum efficiency are needed. The scattering of light within the phosphor layer produces a waste of the spatial resolution: in the standard implementation of this system, the pixel size is around 100 μm, and the readout of emitted light was only from the upper surface of the plate: with this readout approach, the typical limiting spatial resolution has been about 3.5 lp/mm.

1.1.1. Dual-side reading

Recently some CR systems dedicated to mammography has enhanced the efficiency of phosphor plates readout applying a dual-side reading approach [9]. This technology uses a clear support medium, allowing the light emitted during the scanning process to be detected on the ‘‘back side” of the storage phosphor plate (Figure 4). Here a second light guide coupled to a second photomultiplier tube are used to collect this “back” light improving the spatial resolution and the detective quantum efficiency [10] - comparing to the single side reading and bearing a relatively low cost. The two images simultaneously acquired by the CR reader are added together to produce a single image prior to image export. A further advantage of this technology is the reduction of the nominal pixel size at 50 μm [11,12].

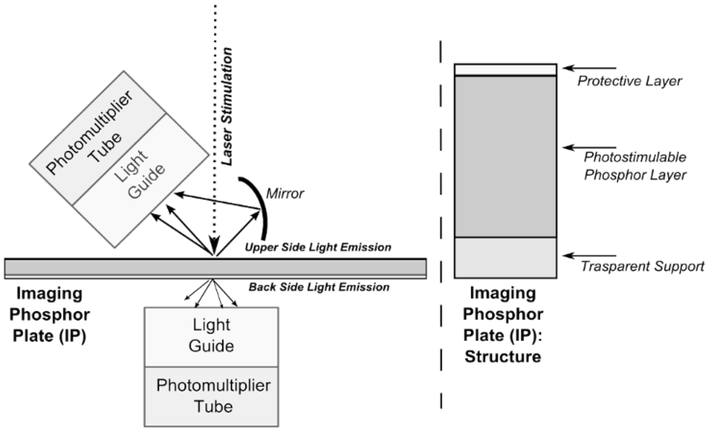

Figure 4. Simplified schematic of the double-readout process of a photostimulable image plate.

The additive process where the “front” and “back” images are added have to be optimized for all spatial frequencies. The filter shape must be chosen in order to maximize the efficiency throughout all frequencies, resulting in substantially improved image quality compared with that of the conventional single side light collection IP image reading system.

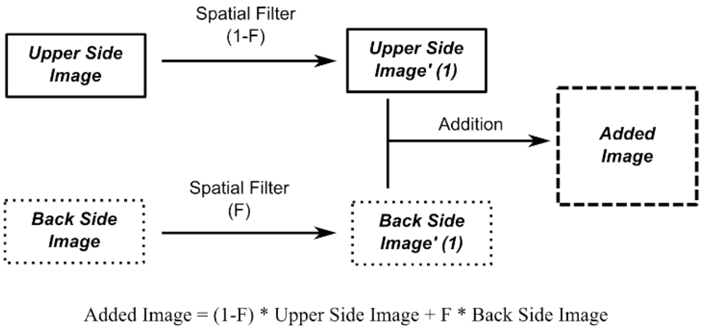

Figure 5. Dual-side images frequency addition using a spatial filter.

1.1.2. Line-scan reading

A line by line phosphor plate scanning and imaging technology has been developed to obtain a faster reading. It is based on stimulation of the phosphor plate one line at a time, and then the photoluminescence signal is acquired by a CCD linear array of photodetectors. A scanning module contains: 1) several linear laser units, 2) an array of optical light collection lenses deployed along the length of the scan unit, and 3) a high sensitivity CCD photosensitive array placed so as to capture the resultant photostimulated luminescence signal simultaneously, one row at a time. Unlike the point scan system the line scan system has a lens array to focus the light along each point of the stimulated IP to a corresponding point on the CCD array (Figure 6).

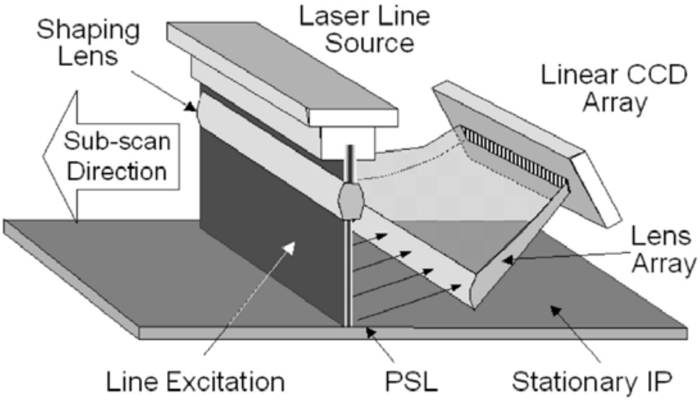

Figure 6. Component-level illustration of a line-scan CR detector. The laser source, shaping lens, PSL lens array, and CCD array move as a unit over the stationary imaging plate. The lens array focuses the light emerging from the IP onto the corresponding detector elements of the CCD array.

1.1.3. Columnar photostimulable phosphor

To reduce the light spread in the photostimulated luminescence emission another development in CR dedicated to mammography has been made using columnar structured storage phosphor based on cesium bromide [13,14] (Figure 7). It provides a good combination both of detection efficiency and spatial resolution - characteristics that are usually a trade off within unstructured phosphor materials.

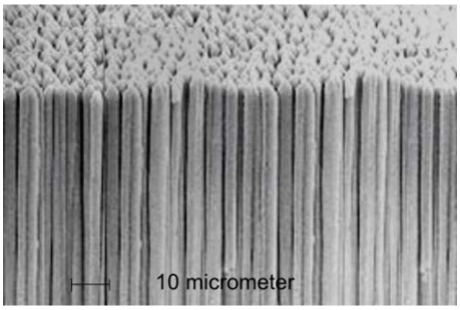

Figure 7. CsI (Tl) needle structure: scanning electron microscopic image.

1.2. Flat panel detectors (FP)

Flat panel detectors based on a large area TFT active matrix array (AMA) are very widespread and typically classified in direct or indirect conversion [15]. The combination of an AMA and an X-ray photoconductor (a-Se) constitutes a direct conversion detector. Instead the term indirect conversion refers to the fact that the X-rays are converted in light using a scintillator phosphor and then in charges using a photodiode. The key factor in these kinds of FP detectors is the development of TFT arrays. In both direct and indirect technology, the latent image is a charge distribution on the panel’s pixels. The charges are read out by scanning the arrays row by row using the peripheral electronics and multiplexing the parallel columns to a serial digital signal as illustrated in Figure 8. This signal is then transmitted to an analog to digital converter and then processed by a dedicated system. An AMA consists of millions of individual storage capacitor electrodes connected to TFTs (one for each pixel) through which charges a read out [16].

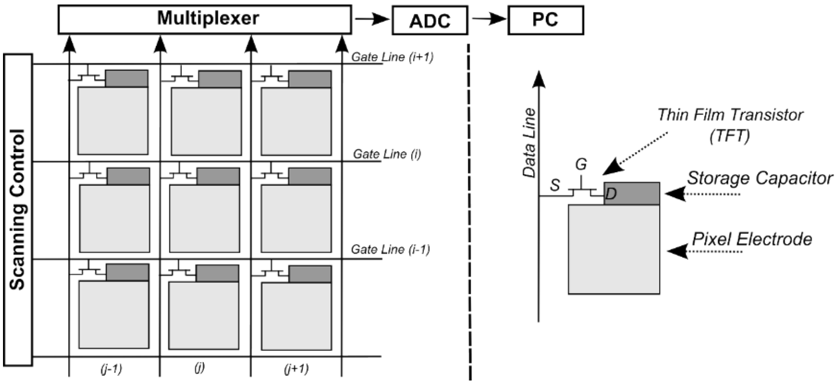

Figure 8. ***Schematic diagram of a generic TFT readout. Charge distribution residing on the panel's storage capacitor is simply readout by scanning the arrays row by row using the peripheral electronics multiplexing the parallel columns to a serial digital signal.***

1.2.1. Indirect conversion detectors: FP based on TFT readout

After X-rays have interacted with the scintillator, the emitted scintillations are detected by a-Si photodiodes and then read trough the TFT switch. The scintillator used in DR is typically thallium-activated cesium iodide (CsI-Tl) layer. Scintillator based FPs employed in FFDM use 100 µm pixel size [17,18,19]. The scintillator can contribute considerably to degradation of the spatial resolution and as the phosphor thickness is high in order to increase the X-rays absorption efficiency, the emitted light can spread from the interaction point before exiting the photosensitive storage element. To optimize this trade off in between efficiency and resolution the phosphor is deposited in a columnar structure that acts as a fiber optic light guide because of the difference in refractive index and the air (around 15%) which fills the space between columns and suppresses lateral light diffusion reducing degradation of spatial resolution (Figure 9).

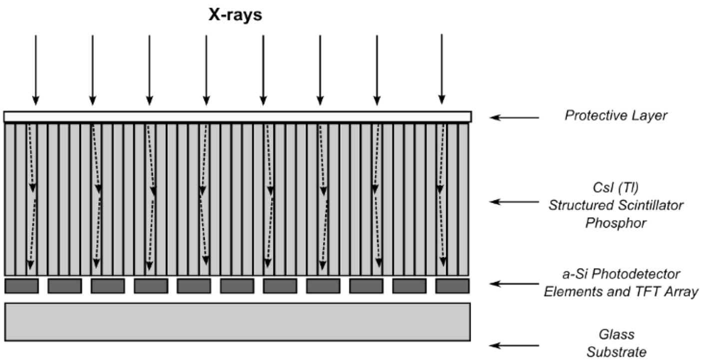

Figure 9. ***Simplified schematic of a structured scintillator-based detector (indirect-conversion) imaging detector. Lateral light diffusion is suppressed by the use of a structured phosphor CsI:Tl (thallium-activated cesium iodide).***

In some implementation this kind of detector are also equipped with a battery power and wireless connection: it permits to use indirect conversion FP (typically coupled with oxysulphide gadolinium instead the thallium-activated cesium iodide) as “removable detector”.

1.2.2. Direct conversion detectors: FP based on TFT readout

Direct detection does not make use of the scintillator, and the conversion is made directly from X-rays to electrons after interaction in a photoconductive layer (Figure 10). When amorphous selenium absorbs X-rays, an electric charge is created in the material in the form of electron-hole pairs [20]. Applying an electric field between the electrodes placed on the upper and lower surfaces of the selenium, the charge signal can be collected onto the readout surface. This surface can be created as a plate of amorphous silicon in a manner similar to that of the phosphor flat-plate system, where the photodiodes are replaced by a set of simple electrode pads to collect the charge. A bias voltage is applied to the photoconductor, and the migrating charges are collected in a micro capacitor element within each pixel and are read out by the AMA. The elimination of the intermediate scintillator layer, which is prone to light diffusion and to some degradation of the spatial resolution, has enabled a-Se detectors to attain excellent spatial-resolution characteristics. In recent years, substantial progress has been made in the manufacturing of a-Se and, most importantly, in advanced charge-readout methods. Up to date AMA is a widespread reading out approach in DR and FFDM systems.

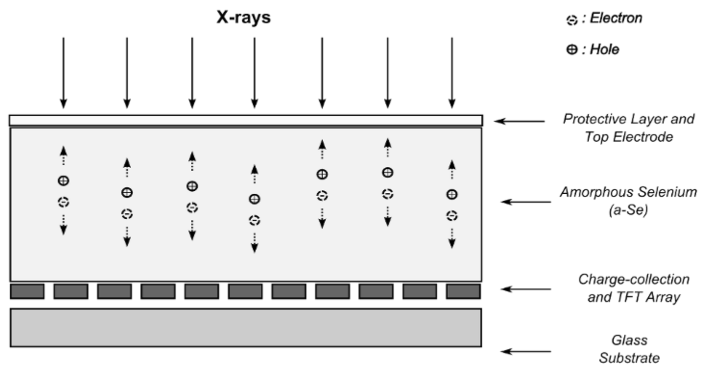

Figure 10. Simplified scheme of an amorphous selenium (a-Se) (direct-conversion) imaging detector. High spatial resolution is attained because of the inherent nature of the direct-conversion process.

In DR systems a pixel size of 150-200 μm is easily attainable for indirect detection systems and 100-150 μm for direct detection systems. In FFDM the implemented pixel size are a little bit smaller (as well the photoconductor thickness) that is around 100 μm for indirect detection systems and 50-80 μm for direct detection systems

The imaging characteristics of the direct and indirect FPs can differ noticeably, seeing as the image formation process in the two detectors is considerably different. On one hand, direct conversion systems based on a-Se present an excellent spatial resolution and appears to be the more promising for any application below 100 keV, according to Hajdok *et al*. [21]. On the other hand, usually a-Se detectors show worse noise characteristics, with respect to other systems [9,18,22]. Most of the noise introduced by the detector is due to the electronic readout. Many approaches have been explored for reading out signals in a-Se plates [23,24,25] and up to 2009 all the commercial FFDM systems consisting on a-Se detectors employ a readout based on an active matrix array of Thin Film Transistors (TFT) [26].

1.2.3. Direct conversion detectors: FP based on optical readout

A recent (2009) relevant approach in the amorphous selenium readout is the optical switch instead of the typical TFT readout. The detector consists of six main components as illustrated in Figure 11: a negative top electrode, a thick X-ray photoconducting layer (PCL), an electron trapping layer (ETL), a thin readout PCL, stripe electrodes, and an optical source. The X-ray PCL is made of a layer of a-Se with a thickness of less than 200 μm [25,27,28]. In this setup, X-ray photons are directly converted into electron-hole pairs.

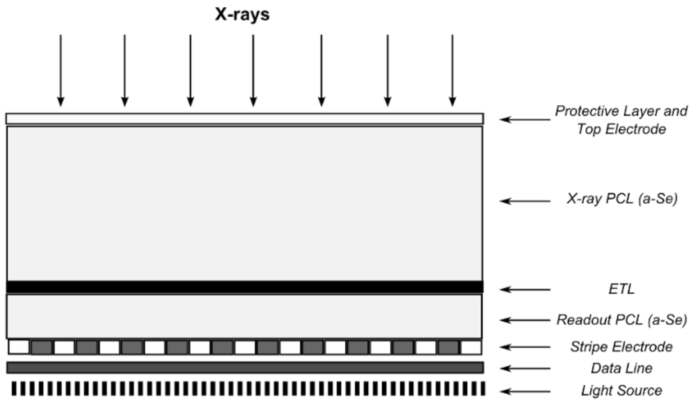

Figure 11. Sketch of the detector of a FP system based on optical readout. The main components of the detector are a negative top electrode, a thick X-ray PCL, an ETL, a thin readout PCL, stripe electrodes, and an optical source.

Using a strong electric field, the generated electrons are accumulated on the ETL, where a latent electron image is formed. After X-ray exposure, the negative voltage is turned off and the top electrode becomes grounded. Trapped electrons induce positive charges on the stripe electrodes and an electric field in the readout PCL. In the subsequent readout phase, light is irradiated from a linear optical source, which generates electron-hole pairs in the readout PCL. These electrons are drifted and collected on the stripe electrodes, where they are detected as signal charges (Figure 12). The line source moves along a direction perpendicular to the direction of the stripe electrodes, while for each position of the line source, data are readout on the direction indicated.

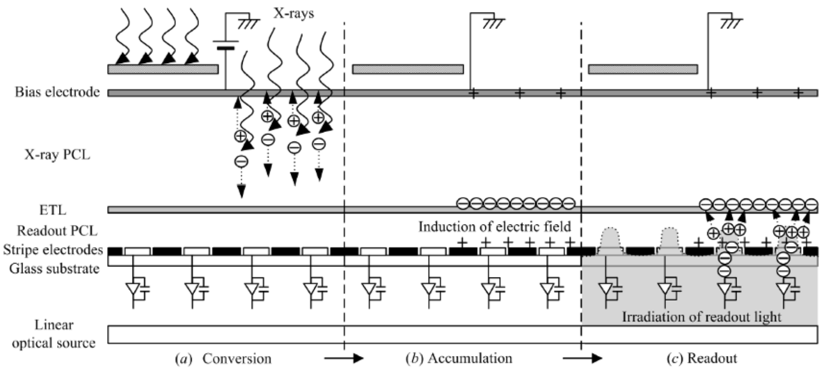

Figure 12. Optical switch scheme imaging processes from (a) conversion, (b) accumulation to (c) readout and behaviors of charges in the detector.

1.3. Slot-scan Technology

Some FFDM devices use a slot-scan projection geometry; in this approach the image acquisition is performed by a narrow beam that scans the breast. Despite a long acquisition time the slot-scan geometry provides excellent and efficient scatter removal through the breast. The time required for a complete scan is few seconds and so problems associated with mechanical movement issues, artifacts and X-ray tube heating arise. In slot-scan technology X-ray tubes with a tungsten target is preferred to the typical molybdenum or rhodium thanks to the higher melting point. Due to the big matrix size slot-scan projection geometry isn't used in DR.

1.3.1. Indirect conversion approach: CCD

In this approach a slot-scan detector uses a CsI(Tl) scintillator coupled to an array of CCDs through fiber optic tapers and operate in time delay integration mode [29,30,31]. As in indirect conversion the scintillator convert X-rays in visible light and the CCD array converted light into charge signals, which are shifted along each row in alignment with the scanning direction to allow the exposure signals to be integrated on each detector element [32,33]. The size of the detector is around 20 cm x 1 cm and the X-ray beam is collimated into a narrow slot to match the detector size.

1.3.2. Crystalline silicon strip: photon counting

Another slot-scan approach uses X-ray photon counting detector [34]. In this approach, an X-ray sensitive solid state device, typically linear silicon strip detectors in an edge-on geometry connected to photon counting electronics is used [35], and the X-ray energy is converted directly into electrons. Prototypes based on high-pressure gaseous ionization chamber and on GaAs are, up to date, work in progress [36].

The unique feature of this approach is the ability to count individual X-ray photons. The counting of individual X-ray photons enables the measurement of the pulse height generated by each detected X-ray. It is possible to reject pulses of low amplitude that are generated from noise in the detector or in the electronic components. Moreover photon counting approach provides the possibility to eliminate the noise due to variation in the amount of charge produced per quanta at the different spectrum's energy. Instead of accumulating charge from multiple X-rays, the absorbed X-ray quanta are simply counted and each photon produces one count, regardless of its energy or how much charge it actually deposits on the detector.

The ability to perform pulse height analysis may provide some interesting options for image processing. Images corresponding to a particular energy can be generated, or the images can be weighted according to energy content. For example, X-rays with high energy may be assigned a lower weighting, while those with lower energy may be assigned a higher weighting for improved contrast.

A system's sketch is shown in Figure 13, the X-ray beam is collimated to a fan beam matching the pre-collimator. This fan beam is enclosed in a scatter protection device that blocks secondary radiation from the air volume before the pre-collimator to reach the breast. The pre-collimator transforms the beam to few equidistant linear beams. Beneath the breast support there is post-collimator and few linear silicon strip detectors matching the linear beams exiting the breast. The fan beam, pre-collimator, post-collimator and silicon strip detectors move, with a continuous motion, along an arc with the axis of rotation collinear with the X-ray tube focal spot in order to scan the breast in a direction perpendicular to the chest wall.

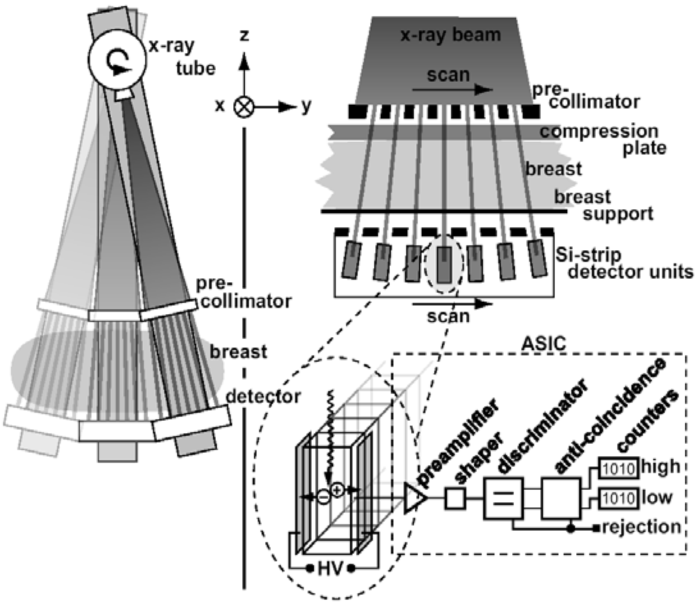

Figure 13. ***Sketch of a slot-scan projection geometry FFDM: he arm is rotated around the center of the source to acquire an image. On the left the mammographic X-ray tube; on the right (up) the X-ray collimation and down a simplified detection head's scheme.***

2. CHAPTER 2: CHARACTERIZATION METHODS

2.1. Physical characterization

There is growing consensus that the DQE is the most suitable parameter for describing the imaging performance of an X-ray imaging device. Basically, the DQE describes the ability of the imaging device to preserve the SNR from the radiation field to the resulting digital image data. It may said that the DQE combines the effect of the contrast and the noise performance of an imaging system, expressed as a function of object size. In practice, DQE considers both spatial resolution (i.e. MTF) and image noise (i.e. NPS) to provide a measure of the SNR of the various frequency components of the image.

The spatial resolution concept refers to the ability of the system to represent distinct features within the object being imaged. It could be defined as the ability of the system to distinguish neighboring features of an image from each other and is connected to sharpness. Sharpness of an image is very important feature and is related to various factors:

✓ the intrinsic sharpness of the detector employed

✓ the subject contrast, as determined by object characteristics, beam quality, and scatter, as well as the blur caused by the finite size of the X-ray focal spot

✓ the patient motion during the acquisition

The sharpness of an imaging detector can be characterized in terms of its MTF. MTF gives an idea of a deeper and more objective conception about spatial resolution. The MTF of an imaging system is defined as the absolute value of its optical transfer function (i.e. the ratio of relative image contrast divided by relative object contrast). It is calculated as a function of the spatial frequencies and is normalized to unity at spatial frequency zero. The essential meaning of MTF is rather simple. At frequencies where the MTF of an imaging system is 100%, the contrast of the object is unattenuated - it retains full contrast. At the frequency where MTF is 50%, the contrast half its original value, and so on. MTF represents how well an imaging system reproduces high contrast objects of different size in the resulting image, and, therefore, represents the relationship between contrast and spatial resolution [37].

The noise is recognized as an important factor in determining image quality. Noise comes up from a number of sources that produce random variations of signal. These fluctuations can obscure useful information's in a diagnostic image. The two major groups of sources generating noise are quantum and electronic noise. Random noise means fluctuations of the signal over an image. When we consider uniform exposures, the noise can be characterized by the standard deviation of the signal variations. The Fourier spectrum can be used to get a more complete description of the spatial correlation of the noise and its distribution over the spatial frequencies. This spectrum, also known as Wiener spectrum or Noise Power Spectrum, measures the noise power as a function of spatial frequency [38]. In other words, it can be seen as the noise variance of the image, expressed as a function of spatial frequency. NPS provides the means of characterizing image noise and plays a central role in the ultimate measure of image quality. Noise is a major limiting factor in object detection and in a given system is strongly dependent on the exposure values, and, consequently, on the dose to patients.

Physical measurements of SNR, MTF and NPS form together a basis for the description of image quality which encompasses the three primary physical image quality parameters. Establishing a complete characterization of the physical properties of the digital image system requires the determination of MTF, SNR, NPS, and DQE. DQE is defined as the squared ratio of the spatial frequency dependent SNR at the output to the SNR at the input of the detector. It can be studied as a function of spatial frequency, thereby providing information on the overall signal and noise performance of an imaging detector. The experimental determination of the DQE is usually done by measurements of the MTF and the NPS, the results of which are, after proper normalization, combined to obtain the DQE. Figure 14 summarizes main attributes and quantitative parameters involved in the physical characterization of a digital imaging system.

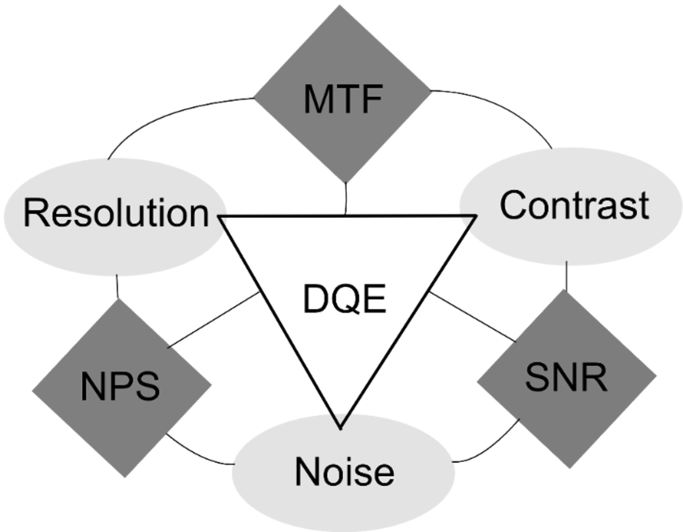

Figure 14. The relationships between different image attributes and measurement of image quality: signal-to-noise ratio (SNR), modulation transfer function (MTF), Noise Power Spectrum (NPS), and Detective Quantum Efficiency (DQE).

Before performing the physical characterization images are usually linearized, by using a suitable conversion function (i.e. response curve). The conversion function is basically the detector output level as a function of number of the exposure. For measuring this function, some steps must be completed:

1. irradiation of the detector using the standard spectrum and geometry;
2. measurement of the air kerma at the detector surface for each exposure;
3. plotting the average detector output level of a selected Region of Interest (ROI) vs the exposure;
4. fitting a curve to the data.

The outcome of the fitting is the response curve of the detector. The inverse of the response curve is used to transform the images used for MTF and NPS to units that are linear with respect to the exposure.

The following linear and image-independent corrections of the raw date should be done, before the processing of the data for the determination all the parameters (MTF, NPS). All the following corrections, if used, shall be made as in normal clinical use.

✓ Replacement of the raw data of bad or defective pixels by appropriate data.

✓ A flat-field correction comprising corrections for the non-uniformity of the radiation field, the offset of the individual pixels, gain correction for the individual pixels, and a correction for geometrical distortions.

2.1.1. Modulation Transfer Function (MTF)

Every image can be described in terms of the amount of energy in each of its spatial frequency components. MTF describes the fraction of each frequency component that will be preserved in the captured image. In other words, MTF is a measure of the ability of an imaging detector to reproduce image contrast from subject contrast at various spatial frequencies.

Blurring and unsharpness introduced by the imaging system results in higher spatial frequencies not being transmitted as well as lower spatial frequency information. As a result, the MTF progressively decreases with increasing spatial frequency. In fact, the MTF is normalized to unity at zero spatial frequency by convection. For ideal imaging systems, the MTF remains constant at 1 for the entire range of spatial frequencies. On the other hand, real systems are characterized by having a MTF close to 1 (or 100%) at low spatial frequencies, and generally falls as the spatial frequency increases until it reaches zero (Figure 15). The contrast values are lower for higher spatial frequencies. As spatial frequency increases, the MTF curve falls until it reaches zero. This is the limit of resolution for a given system. When the contrast value reaches zero, the image becomes a uniform shade of grey.

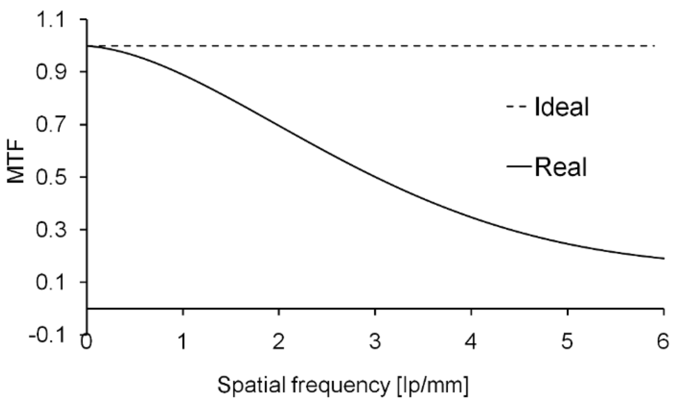

Figure 15. Comparison of real and ideal MTFs.

Image spatial resolution can vary substantially, depending on physical detector characteristics. Limiting spatial resolution is determined by the pixel spacing in the detector. The frequency that characterizes this limiting resolution is known as the Nyquist frequency. It is simply the inverse of twice the pixel spacing.

The most common way to measure the MTF of a system for digital detector is based on the use of a sharp edge phantom [1]. This phantom is imaged to produce an Edge Spread Function (ESF). The ESF is then differentiated to obtain the Line Spread Function (LSF), from which the MTF is calculated by a Fourier transform. However, in some cases different phantoms were used (e.g. single slit devices [39]) for achieving the pre-sampling MTF of digital mammography detectors. According to International Standards (IEC), the edge phantom for the determination of the MTF shall consist of a stainless steel (or tungsten) plate with minimum dimensions: 0.8 mm thick, 120 mm long and 60 mm wide, covering half the irradiated field. The edge phantom is placed on the detector surface, tilted (1.5°-3°) to detector axis to measure MTF perpendicular to that axis. The centre of the edge should be placed in the detector surface centre (or 50 mm from the centre of the chest wall side of the detector in FFDM). The irradiated area of the detector surface shall be 100 mm by 100 mm with the centre of this area 50 mm from the centre of the chest wall side of the detector.

2.1.2. Noise analysis

Noise is one the major factors impairing the quality of digital images. One of the simplest way to characterize the noise is through the SNR. It represents the relationship between contrast and noise in an image for large scale objects. While contrast and image noise properties are important by themselves, it is really the ratio between them that carries the most significance and constitutes the most significant indicator of image quality. The SNR describes the ability of a detector to differentiate a signal from random fluctuations in signal intensity or noise in an image. In digital X-ray systems, as noise decreases and SNR increases, object detection increases very rapidly.

The amount of noise present within an image strongly depends on the level of the exposure used for acquiring the image itself. Thus, one has to determine carefully the exposure value associated to the measured noise. The exposure at the detector surface must be measured with an appropriate radiation meter. For this purpose, the digital X-ray detector should be removed from the beam and the detector of the radiation meter should be placed in the detector surface plane. Care shall be taken to minimize the back-scattered radiation. It is recommended to repeat each measurement about five times and to use the average for the correct exposure. If it is not possible to remove the digital X-ray detector out of the beam, the exposure at the detector surface may be calculated via the inverse square distance law. For that purpose, the exposure is measured at different distances from the focal spot in front of the detector surface. For this measurement, radiation, back-scattered from the detector surface, shall be avoided. The irradiated area is the same considered for MTF calculation. A square area of approximately 50 mm × 50 mm located centrally in the 100 mm × 100 mm irradiated area is used for the evaluation of an estimate for the noise analysis.

Mathematically, the image noise of stationary imaging systems can be characterized by the noise power spectrum (NPS, or Wiener spectrum). NPS represents the relationship between noise and spatial resolution. The NPS can be defined as the variance per frequency bin of a stochastic signal in the spatial frequency domain. In fact, it represents the noise power in an image as a function of spatial frequency. More specifically, NPS may be thought of as the variance of image intensity (i.e., image noise) distributed among the various frequency components of the image. NPS is computed from uniformly exposed images acquired at different exposure levels. At least four images are considered for each exposure level; and for each image a fixed-size ROI is extracted, Fourier transformed and averaged, to compute the 2D NPS. The NPS is then normalized for the squared mean signal value of the ROI. The 1D NPS was obtained by excluding the principal axes and by averaging the 2D spectrum along a radial line (Figure 16A and B).

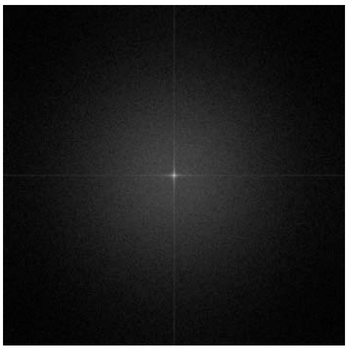

A

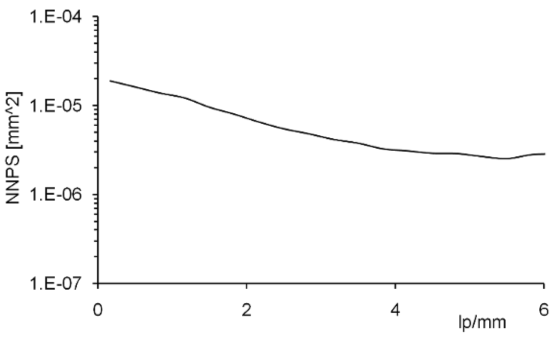

B

Figure 16. Comparison of a 2D NPS (A) and the corresponding 1D NPS (B) used for DQE calculation, estimated along a radial line of the 2D spectrum.

The variance of an image is connected to the amount of noise of the image. The variance can be described as the sum of three terms related to Poisson, multiplicative, and additive noise. The three components result to be proportional to exposure (Poisson noise) and to the square of exposure (multiplicative noise) and exposure independent (additive noise). Relative Standard Deviation (RSD, i.e. standard deviation divided by average signal value) provides a way to estimate the different components of the noise. RSD can be calculated within a chosen ROI. To get a significant estimate of the noise, a number of ROIs from different images acquired at the same exposure is usually considered. The average RSD over the ensemble of ROIs can then computer fit using the following function:

$$RSD(x) = \frac{1}{x} \cdot \left(\alpha \cdot \sqrt{x} + \beta \cdot x + \gamma\right) \qquad \text{Eq.1}$$

The term in parentheses represents the absolute standard deviation and α, β, and γ, represent the contributions of the quantum-statistical (Poisson) noise source, of a dose related (multiplicative) noise source, and of a dose independent (additive) noise source, respectively. The additive component is usually related to electronic noise, whereas the multiplicative component could be a fixed pattern noise not removed by flat-fielding. The same ROIs used for NPS calculation can also be used to perform the RSD analysis. To obtain a thorough characterization of the system noise, both NPS and Relative Standard Deviation (RSD) analysis can be performed.

2.1.3. Noise equivalent quanta and detective quantum efficiency

The NEQ concept was introduced by Shaw in 1963 [40] to analyze the photographic process in terms of the SNR in independent spatial frequency channels. It removed much of the ambiguity from image assessment, allowing a straightforward analysis of photography, electronic imaging, and many other modalities. NEQ can be interpreted as the number of quanta at the input of an ideal detector that would yield the same SNR, as a function of spatial frequency, as the real detection system under consideration. In other words, NEQ expresses the quality of the image data by the photon fluence that the image is worth at each spatial frequency. Once MTF and NPS are known, the NEQ can be computed by the following formula:

$$NEQ(f) = \frac{MTF^2(f)}{NPS(f)} \qquad \text{Eq.2}$$

DQE is one of the best and most widely accepted overall measures of detector image-quality performance. DQE characterizes the efficiency of information transfer from the input to the output of the system. The information available in any image is limited by the finite number of X-ray quanta incident upon the imaging detector, which in turn is related to patient dose. The information limit results directly from the inherent statistical nature of X-ray quanta. An ideal imaging system accurately records every incident X-ray quantum and is characterized by a DQE of 100%. On the other hand, real imaging systems always have a DQE of less than 100% because of inefficiencies in detecting the incident X-ray quanta and internal sources of noise. In fact, the DQE of real detectors does not have a single value, but varies depending on the X-ray beam used, exposure values, and the spatial frequency. Further, several factors strongly influence the DQE of a detector. These include less than complete X-ray absorption, factors which reduce the amplitude of the signal profile (as measured by MTF), and additional sources of noise.

For calculating the DQE, the photon fluence of the X-ray beam considered must be estimated. For standard X-ray beams, data are available in IEC standard [41]. Alternatively, HVL measurements can be made from logarithmic interpolation of the measured exposure values when different aluminum foils are placed through the beam. The photon fluence for the considered X-ray beam must then be estimated, and the number of photons per unit area at the measured exposure computed. DQE can then be calculated as:

$$DQE(f) = \frac{NEQ(f)}{q} \qquad \text{Eq.3}$$

where q is the number of photons per unit area.

2.2. Psychophysical characterization

Image noise and image signal power are recognized as fundamental components of image quality for all imaging modalities. Therefore image quality is frequently described in terms of image contrast, resolution and noise. Images are a means for visually representing the clinical information captured by the digital mammography units. Consequently, it is expected that image quality should also be based on the judgment of a human observer. It is well known that image assessment is task dependent, so it is necessary to specify a task for the observer. In fact, in the clinical setting image quality is most commonly evaluated by visual observations of images of test objects, such as a resolution test pattern or a phantom with low contrast details. To this purpose, contrast-detail phantoms are often used. The measurement result is obtained as the faintest detectable object in the image.

Low spatial frequencies are usually important for low-order imaging tasks, such as detecting simple objects in uniform backgrounds. An example of a low-order imaging task would be the scoring of contrast-detail test objects. However, for higher-order imaging tasks that require localizing and characterizing complex objects in non-uniform background, high frequencies become more important. Many clinical tasks require localization and characterization of small anatomical structures. These are examples of high-order imaging tasks. Thus, having high DQE over the entire diagnostic range of visual information is necessary for optimal performance in the wide range of imaging tasks found in clinical practice.

There are several ways with which a visual evaluation of image quality can be made – with a varying degree of sophistication. Presently, the Receiver Operating Characteristic (ROC) and Multiple Alternative Forced Choice (MAFC) tests are considered to be the best methods of obtaining quantitative and objective results of human observers' ability to detect signals in the images. There is also a variety of theoretical models that can be used for estimating the performance of digital systems on well-defined tasks. The pioneering work of Rose has a fundamental role in setting performance limits for detectability of objects [42,43]. Rose's SNR approach is still used in attempts to evaluate or describe image quality or the performance of imaging system components.

2.2.1. Theoretical models

Rose in his seminal publications proposed and described the use of an absolute scale (quantum efficiency) for evaluating imaging system performance, and a simple model of signal detectability by human observers. Rose used a particle-based fluctuations theory to compare real devices with an ideal device, with the performances of both being assumed to be limited only by photon fluctuations. The relationship between the number of image quanta and perception of detail is embodied in the "Rose Model," as it has come to be known, that describes the SNR for the detection of a uniform object in a uniform background.

It would not be of much interest to study how an unskilled or inefficient observer would succeed in detecting the signal: the results would describe more the observer's (in)ability than the actual information in the images. In order to get a unique performance figure which describes the actual quality of the image data in an absolute scale one uses the best possible observer (the ideal observer) for observing the images. This observer uses all the information in the images and all available prior information in the optimal way to make its decision. The ideal observer then achieves the lowest detection error rate that is possible by using the image data. Therefore, the performance of the ideal observer is a measure of the amount of information in the image which is relevant to the specified imaging task. Often, we consider the detection of a signal with known parameters (size, shape, location) in additive, uncorrelated Gaussian noise on a known background. This is usually referred to as the signal-known-exactly (SKE), background-known exactly (BKE) detection task. Rose's model is a useful approximation for SKE and BKE detection of a limited subset of signals and noise. In an SKE/BKE task any decision errors that the ideal observer makes result from the image quality not being perfect; full prior data is given to the observer. One must be cautious in interpreting the SKE/BKE data, however, because sometimes the detection task may become too tightly specified and not anymore correspond to the actual detection task of interest.

Rose used his model to assess the detectability of signals, by estimating the minimum SNR required in order to detect a signal. His approach was to use a constant, *k*, defined as the threshold SNR, and to suggest that the value of *k* must be determined experimentally. The signal was expected to be reliably detectable if its SNR were above this threshold. Once *k* is selected, for a circular target of diameter α the corresponding contrast threshold C_{TR} can be expressed as:

$$C_{TR} = \frac{2k}{\alpha\sqrt{\pi \cdot q \cdot DQE(0)}} \qquad \text{Eq.4}$$

where *DQE(0)* is the DQE at zero spatial frequency, and *q* represents is the number of photons per unit area, as defined in section 2.1.3.

In measuring the SNR, it may not always be necessary to consider the strict ideal observer. Other computational observers, such as the non pre-whitening matched filter [44], perceived statistical decision theory model [45], the NPWE model [46], the Hotelling Observer [47], the channelized ideal observer [48], the DC-suppressing observer [49] have been suggested for sub-optimal alternatives, among others. A number of publications have shown the close relationship between the performance of such observers and human observers.

2.2.2. Contrast-detail phantoms

Phantoms can be manufactured with a variable amount of anatomical detail, but usually simple homogeneous phantoms that mimic the radiation attenuation and scattering properties of the human body will be adequate. Common test details consist of disks of various contrasts and diameters for measuring the low-contrast-detail detectability (contrast resolution) or contrast-detail performance. These phantoms consist in a number of objects with different size and thickness. They are used for individuating the boundary between visible and invisible objects acquired by the detectors. CD analysis is a step towards the examination of details resembling clinical lesions, even if one has to be aware that results obtained with CD studies could not be directly extended to clinical detection tasks. The main limitations of most of the currently available phantoms are their short dynamic range compared to a real breast and their uniform background, very different from the typical structured backgrounds of breast patterns. Further, high inter- and intra-observer variability can affect the effectiveness of the subjective observations obtained with CD analyses.

The CDRAD 2.0 phantom (Artinis, Medical Systems B.V., Zetten, Netherlands), shown in Figure 17A, is one of the most common phantoms and is specially developed to facilitate the monitoring of image quality in digital radiography. Such a phantom, made in polymethylmethacrylate, is developed with the purpose of estimating the perception of details on a range of sizes and contrasts and is composed of 225 squared cells organized as an array of 15 rows and 15 columns. Each cell contains two identical holes, one in the center and one in a randomly chosen corner. The size of the disks varies logarithmically from 0.3 to 8 mm in both diameter and depth. The observer (human or automatic) has to indicate the corner where the eccentric disk is located.

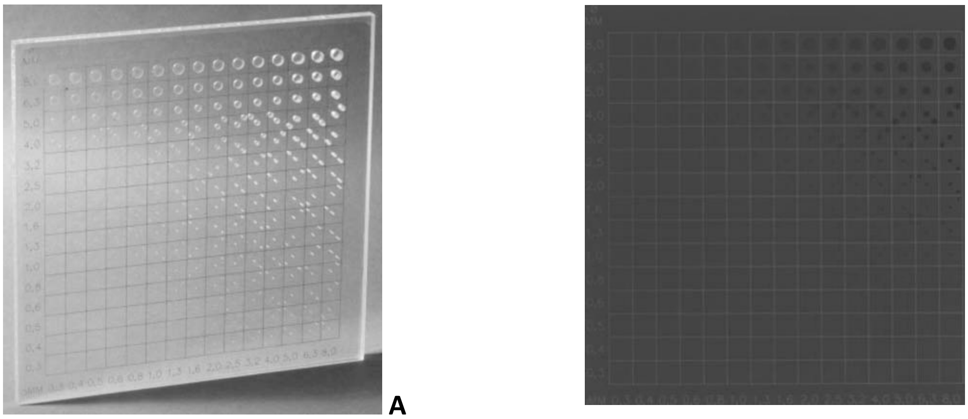

A B

Figure 17. The CDRAD 2.0 Phantom (A) and a radiographic image (B).

The CDMAM 3.4 phantom, shown in Figure 18A, is another very common phantoms, similar to the CDRAD but developed for monitoring mammographic detectors. The CDMAM, made of aluminum and gold, consists of a matrix of squares (16 rows and 16 columns), each square containing two identical gold disks of given thickness and diameter. One disk is placed in the center and the second in a randomly chosen corner. The observer (human or automatic) has to indicate the corner where the eccentric disk is located. The phantom covers a range of object sizes and thicknesses representing microcalcifications and small masses. The object diameters range between 60 microns and 2 mm. The object thicknesses range between 0.03 and 2 microns of gold, resulting in a radiation contrast range of about 0.5-30% at standard mammography exposure conditions (28 kVp, Mo-Mo). Within a row, the disk thickness is constant with logarithmically varying diameter. The phantom is usually placed with the smaller details close to the chest wall side. It is better to reposition it after each exposure, in order to get images with various phantom-object positions with respect to the pixels of the detector and to avoid that a small detail always remain in the same detector area.

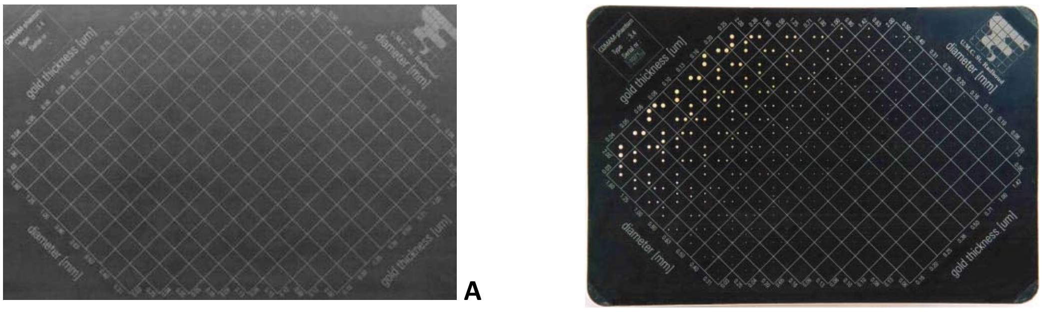

A B

Figure 18. The CDMAM 3.4 Phantom (A) and a radiographic image (B).

Reading CD phantoms by human observers is a very tedious and time consuming task. To overcome this shortcoming, automatic methods have been developed and evaluated [50]. Such methods reduce *inter* and *intra* observer subjective variability, and dramatically decreases the time needed to analyze scores of images. Our group has developed a software that automatically reads the CDRAD images[51] which is written in IDL™ (RSI, Pearl East Circle Boulder, CO) and can be freely downloaded at the *Medical Imaging Group at University of Bologna* (http://www.df.unibo.it/medphys/). Figure 19 shows the main panel of this software.

First of all, the software requires a manual registration of the phantom. The software scans all the cells of the phantom. For each cell shown in the left part of the graphical user interface (GUI) a few parameters for the central disk are estimated for obtaining the CD curve. Specifically, a few ROIs positioned within the central details and on the background of the cell are used to calculate the Signal-to-Noise Ratio (SNR) for each cell of the phantom. The noise is computed as the fluctuations of the background. After having calculated the SNR for each cell of the CDRAD phantom, we computed a detectability index based on SNR and contrast, according to the ideal observer model in a SKE/BKE task. In practice, the detectability of the system is estimated as the ratio between the intrinsic contrast of the object and the estimated SNR. We did not fix a threshold on SNR, we just estimated the contrast threshold of the CD curve as the abovementioned ratio, as derived by fitting the experimental data (SNR vs intrinsic contrast) for each diameter. For each exposure a CD curve is obtained by averaging results of the four images acquired with that specific exposure.

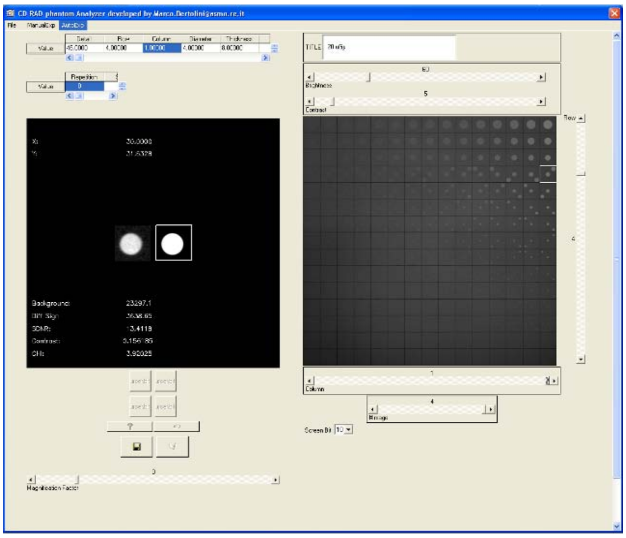

Figure 19. The main panel of the GUI developed for the automatic reading of the CDRAD phantom images. The software scans all the cells of the CDRAD phantom, each time estimating some parameters for calculating the contrast-detail curve.

Also for CDMAM images can be use automatic reading: nowadays software are available for the automatic reading of the CDMAM images. For instance, CDCOM is a well-know and freely available software (www.euref.org) developed by the Radiology Department of the University Medical Centre in Nijmegen [52]. CDCOM achieves the automatic reading of the CDMAM phantoms by performing various steps. The first process consists in the detection of the borders of the phantom by using the Hough transform and the subsequent estimation of the centre of each cell. The average pixel value of four ROIs located near the corners is then calculated for each cell. The position of the eccentric disk is supposed to be within the ROI with the highest average value. The detection fraction of each cell is then calculated by using a set of images acquired at the same exposure. In this work we first fitted these results with the same psychometric curve used with human observers (Weibull function). In addition, we also reported CD curves obtained with the CDMAM Analyser software (Artinis, Medical Systems B.V., Zetten, The Netherlands). This program gives the user reports of the quality of the images obtained starting from the same CDCOM readings. In this work we averaged the results obtained from the six images acquired for each exposure. A comparison between the CD curves obtained and theoretical data estimated from the Rose model was also evaluated [53]. According to this model, for a circular target of diameter α, the contrast threshold (C_{TR}) can be assessed as in Eq.4.

2.2.3. Contrast-detail curves

Several parameters can be extracted from a CD analysis. First, a CD curve can be derived, which shows the minimum detected contrast for each object diameter. Further, other more compact figures can be estimated, such as Correct Observation Ratio (COR), and Image Quality Figure (IQF) and Inverse Image Quality Figure (IQF_{inv}) defined as follows:

$$COR = \frac{Correct\ observations}{Total\ number\ of\ squares} \cdot 100\% \qquad \text{Eq.5}$$

$$IQF = \sum_{i=1}^{n} C_i \cdot D_{i,\min} \qquad \text{Eq.6}$$

$$IQF_{inv} = \frac{100}{\sum_{i=1}^{n} C_i \cdot D_{i,\min}} \qquad \text{Eq.7}$$

where $D_{i,min}$ denotes the threshold diameter in contrast column *i*, n is the number of column in the phantom. Summation over all contrast columns yields the IQF.
There are two major problems with these kinds of measurements. The first is related to the clinical significance of the measurement results: gold disks are not clinically meaningful objects. This situation could be improved by designing various test details that simulate actual important anatomical details in different examinations. The second problem is the subjectivity of the test, which results in considerable intra-observer and inter-observer variability and may make the detection of image quality differences or changes uncertain [54]. This situation can be improved if the measurement is made relative by comparing the image with a previously taken reference image. Precision can also be improved using several independent observers and/or images. A further possibility, especially useful for constancy testing of digital imaging equipment, is to design computer programs that evaluate the test images using suitable algorithms [52].

2.2.4. ROC curves

In signal detection theory, a Receiver Operating Characteristic [55,56], or simply ROC curve, is a graphical plot of the sensitivity versus. false positive rate for a binary classifier system as its discrimination threshold is varied. A ROC can also be represented equivalently by plotting the fraction of true positives out of the positives versus the fraction of false positives out of the negatives.

Receiver operating characteristic (ROC) analysis defines the medical image quality in terms of the ability of human observers (or a computer algorithm) to use image data to classify patients as positive or negative with respect to any particular disease.

Examples of diagnostic-accuracy measures include percent correct, sensitivity and specificity, and ROC curves. ROC curves provide the most comprehensive description, because they indicate all of the combinations of sensitivity and specificity that a diagnostic test is able to provide as the test's "decision criterion" is varied. Figure 21 shows a typical ROC curve, which plots true positive fraction (TPF) as a function of false positive fraction (FPF). TPF is equivalent to the sensitivity index often reported in the clinical literature. Higher ROC curves indicate better diagnostic accuracy, because the probability of detecting the disease in question is then greater at each possible false-positive rate.

The *Confusion Matrix* (also called *contingency table*) [57] shown in Figure 20 is useful visualization tool to see if the system is confusing two classes: each column of the matrix represents the instances in a predicted class, while each row represents the instances in an attended class.

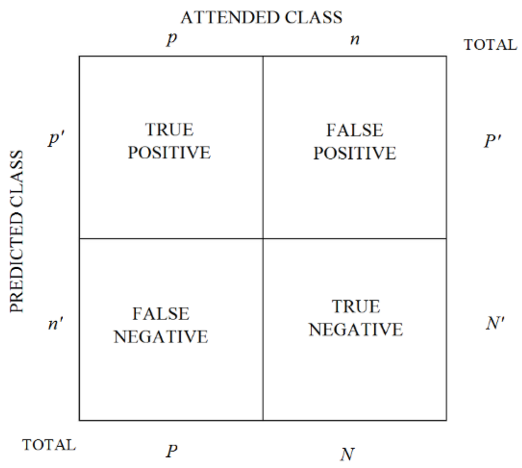

Figure 20. The Confusion Matrix

From the *Confusion Matrix* comes the following two metrics: TPF is define as:

$$TPF = \frac{Positives \cdot Correctly \cdot Classified}{Total \cdot Positives} \qquad \text{Eq.8}$$

Analogously, FPF is define as:

$$FPF = \frac{Negatives \cdot Incorrectly \cdot Classified}{Total \cdot Negatives} \qquad \text{Eq.9}$$

Two further associated to those discussed above are the sensitivity, which corresponds to TPF:

$$Sensitivity = TPF \qquad \text{Eq.10}$$

and the specificity which is given by:

$$Specificity = \frac{True \cdot Negatives}{False \cdot Positives + TrueNegatives} = 1 - FPF \qquad \text{Eq.11}$$

Those metrics are fundamental in order to define ROC curves and to understand how they work in for diagnostic systems classification.

The essential requirement in collecting image-reading data for an ROC study is to allow each observer to report his confidence that each case is "positive" or "negative" on a scale that includes more than two alternatives [58]. Either a discrete ordinal category scale (usually with five categories) may be used. In principle, both kinds of scales can yield similar results [59]. However, a discrete ordinal scale can produce biased and/ or highly variable results if it is not used optimally by the observer, so continuous scales are now recommended by many ROC methodologists.

Most ROC studies in medical imaging fit a smooth ROC curve to the ''operating points'' that can be calculated directly from raw confidence-rating data. This allows reliable interpolation between the empirical combinations of FPF and TPF that are found in the data, and it often increases the precision of summary indices of diagnostic accuracy that are derived from the data [60].

After two or more ROC curves have been estimated, the investigator must address the question of whether any difference between the curve estimates is statistically significant — i.e., whether the observed difference can be explained by statistical variations in the data from which the curves were estimated or, instead, it is so unlikely to have arisen only from statistical variations in the data that the investigator must conclude that the difference is real. This question can be addressed by calculating either a "P value" or a "confidence interval" for the difference. In general, confidence intervals are more meaningful, because they provide not only the same information as a P value but also additional information that is especially useful when a difference is tested and found not to be statistically significant. Testing the statistical significance of differences between ROC curves is a complicated subject that requires

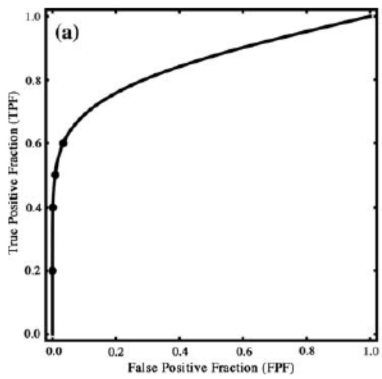

Figure 21. A ROC curve example

ROC analysis provides tools to select possibly optimal models (in this context detectors) and to discard suboptimal ones independently from (and prior to specifying) the cost context or the class distribution. ROC analysis is related in a direct and natural way to cost/benefit analysis of diagnostic decision making.

3. CHAPTER 3: RESULTS

3.1. COMPARISON OF CR SYSTEMS DEDICATED TO CONVENTIONAL RADIOGRAPHY

Abstract

In this section, five different units based on three different technologies—traditional computed radiography (CR) units with granular phosphor and single-side reading, granular phosphor and dual-side reading, and columnar phosphor and line-scanning reading—are compared in terms of physical characterization and contrast detail analysis.

The physical characterization of the five systems was obtained with the standard beam condition RQA5. The quantitative comparison is based on the calculation of MTF, NPS, DQE. Noise investigation was also achieved by using RSD analysis. Psychophysical characterization is assessed by performing a contrast detail analysis with an automatic reading of CDRAD images.

The most advanced units based on columnar phosphors provide MTF values in line or better than those from conventional CR systems. The greater thickness of the columnar phosphor improves the efficiency, allowing for enhanced noise properties. In fact, NPS values for standard CR systems are remarkably higher for all the investigated exposures and especially for frequencies up to 3.5 lp/mm. As a consequence, DQE values for the three units based on columnar phosphors and line-scanning reading, or granular phosphor and dual-side reading, are neatly better than those from conventional CR systems. Actually, DQE values of about 40% are easily achievable for all the investigated exposures.

This study suggests that systems based on the dual-side reading or line-scan reading with columnar phosphors provide a remarkable improvement when compared to conventional CR units and yield results in line with those obtained from most digital detectors for radiography.

In this section five different systems for digital radiography, based on photostimulable storage phosphor are analyzed. The systems are based on different technologies, such as granular or columnar phosphors, single side, dual side, or line-scanning techniques. Two systems are based on the conventional granular phosphor with a single-side laser scanner technology. Another one utilizes the same granular phosphor and a dual-side reading scanner. The last two systems are based on columnar phosphors and line-scanning technique - the latest technology available. We have assessed the physical characterization, in terms of spatial resolution and noise analysis. Specifically: the MTF, NPS, RSD and DQE have been estimated for all the systems using the same acquisition setup. A contrast-detail analysis has also been performed using an automatic CDRAD phantom reading with a software developed by our group. The overall goal is to provide a characterization for some of the most common photostimulable phosphor based systems available on the market and determine the variations in physical parameters due to the different technologies employed.

3.1.1. Materials and methods

The all five units – namely: three FUJIFILM units (FCR Profect ST-VI, FCR Profect ST-BD, FCR Velocity U FP), one Kodak unit (Direct View CR 975), and one Agfa unit (DX-S) - are currently used in radiology departments and their main characteristics are summarized in Table 2. The FCR ST-VI and CR 975 units are based on the well-known CR technology consisting of granular phosphors and single-side flying spot readers. The FCR ST-BD unit applies a dual-side reading system to the same granular phosphor cassettes used in the previous two systems. The last two systems (ST-BD & DX-S) are based on columnar phosphors and line-scanning readers, the best technology available today. All measurements were made using a common radiographic technique. Specifically a fixed tube voltage equal to 70 kVp and additional filtering with 21 mm of Aluminum (standard beam condition RQA5) have been used. In all image acquisitions, the exposure to the detector was measured using desmodronic ionization chamber (UNFORS Xi, Unfors Instruments, Sweden). The SID distance is nearly 180 cm for all the systems.

Manufacturer	**FUJIFILM**	**FUJIFILM**	**Eastman Kodak**	**FUJIFILM**	**Agfa HealthCare**
Model	*FCR Profect ST-VI*	*FCR Profect ST-BD*	*CR975*	*FCR Velocity FP*	*DX-S*
Phosphor type	*Granular: BaFBr(Eu^{2+})*	*Granular: BaFBr(Eu^{2+})*	*Granular: BaFBr(Eu^{2+})*	*Columnar: CsBr(Eu^{2+})*	*Columnar: CsBr(Eu^{2+})*
Phosphor thickness [μm]	*230*	*320*	*300*	*650*	*450*
Reader type	*Single-side reading*	*Dual-side reading*	*Single-side reading*	*Line Scanning*	*Line Scanning*
Imaging area [cm×cm]	*24×30*	*24×30*	*35×43*	*43×43*	*35×43*
Array size	*2364×2964*	*2364×2964*	*2048×2500*	*4280×4280*	*3408×4200*
Pixel pitch [micron]	*100*	*100*	*168*	*100*	*100*
Image depth [bits]	*10*	*10*	*12*	*10*	*14*

Table 2. The investigated CR imaging systems and their principal characteristics.

The response curve of all the systems was determined by exposing the detector to a wide range of uniform X-ray exposures. At each exposure, we estimated the average pixel values from a ROI located near the chest wall. The five clinical CR systems' physical characteristics were then analyzed in terms of MTF, NPS, and DQE. Pre-sampling MTF was measured adopting the well-known edge technique [61,62]. An oversampled line spread function was derived by slightly rotating (≈ 2-4°) a tungsten edge test device (TX 5, IBA Dosimetry, Schwarzenbruck, Germany) with respect to the direction along which the MTF was being measured. The MTFs were measured in both the horizontal and vertical directions. For DQE calculation, the average of the MTF along the two directions was considered. NPS was computed by using flat field images at three different exposure levels (≈2.5 µGy, ≈ 5µGy, ≈ 10µGy). For each exposure level four images were acquired, from each image a fixed ROI was extracted and subdivided in 256 × 256 regions, the 2D normalized noise power spectrum (NNPS) was then derived by averaging square modulus of the Fourier transform of each sub ROI, and the resulting was normalized for the square mean signal value of the ROI. The 1D NNPS were then extracted from the 2D NNPS on a radial direction at 45°, excluding the values along the axes. Noise was also studied through an RSD analysis [9]. We estimated the RSD on the same ROIs used for NNPS calculation. We then fitted the experimental RSD data computed over all the ROIs.

The photon number per unit area *q* was derived from tabulated values for the standard RQA5 beam. We then calculated DQE combining 1D NNPS curves with the fluence measures and the corresponding MTFs, in order to get the final DQE.

The CD analysis was done using the CDRAD 2.0 phantom employing the procedure described in Chapter 2 at the Contrast-detail phantoms paragraph; for each exposure a contrast detail curve is obtained, by averaging results of the four images acquired with that exposure. We tested the statistically significantly difference of two CD curves by performing a non parametric test (Mann-Whitney). We tested both the curves consisting of all the phantom details together, and also the subset of data including only details with a diameter greater than 1 mm. A p-value of less than 0.05 was considered to indicate a statistically significant difference between two curves.

3.1.2. Results

The response curves of the five systems are reported in Figure 22.

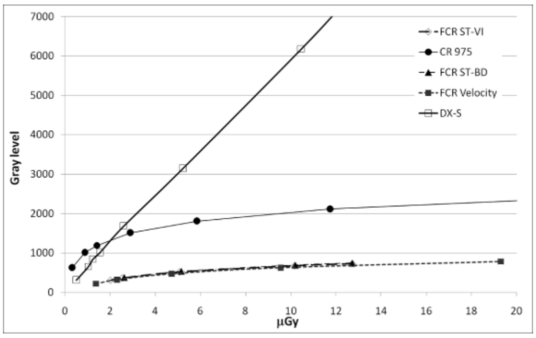

Figure 22. Response curves for the five analyzed CR systems. The Agfa unit has a linear response, whereas all other systems present a logarithmic response. Fitting curves used for linearizing the CR responses are shown in Table 3.

The fitting curves used to linearize CR response and the corresponding goodness of fit (R^2) are shown in Table 3.

All systems presented a logarithm response, except the Agfa unit, which showed a linear behavior over the entire range of investigated exposure levels. All the systems manufactured by FUJIFILM basically present the same curve, whereas the CR975 has still a logarithmic response, but it can provide a wider dynamic range, thanks to the 12 bit quantization.

CR system	**Fitting function**	**R^2 value**
FCR Profect ST-VI	*y = 229 log(x) + 142.8*	*0.9999*
FCR Profect ST-BD	*y = 233 log(x) + 146.5*	*0.9999*
CR975	*y = 421 log(x) + 1069*	*0.9989*
FCR Velocity FP	*y = 214 log(x) + 141.4*	*0.9995*
DX-S	*y = 588 x + 76.1*	*0.9998*

Table 3.Function used for fitting the response curves shown in Figure 22 with the corresponding R2 value for quantifying the goodness of the fit. For all the functions, "y" stands for the Gray Level value of the images, whereas "x" stands for exposure (measured in uGy).

We can also note that the two systems based on CCD detectors (FCR Velocity and DX-S) have a different response curve. In fact, the DX-S unit preserves the linear response typical of CCD detectors, whereas for the FCR Velocity systems a logarithmic transform is applied during the reading step. We considered the fitting functions shown in Figure 22, for linearizing all the images used for the physical characterization.

Presampling MTF curves resulting from the average of the horizontal and vertical directions for the five CR systems are shown in Figure 23.

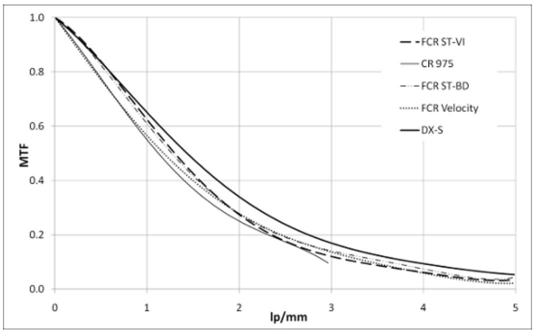

Figure 23. Presampling MTF curves for the five CR systems. The plot shows the MTF as resulting from the average of the two directions (horizontal and vertical).

No appreciable variations in MTF were found when changing the exposure value. It is worth noting that the best MTF is that obtained by the DX-S unit. In fact, even if the phosphor layer used for this system is thicker than in most of the other systems there is no appreciable deterioration of the MTF thanks to its columnar structure. This suggests that it is possible to improve efficiency and noise properties, without reducing too much the spatial resolution. On the other hand, the even thicker phosphor used for FCR Velocity does not allow for MTF values comparable to those from the DX-S. Most likely, the thickness of the phosphor for FCR Velocity unit was chosen to give spatial resolutions comparable to those of the standard CR systems.

The unit based on dual-side reading presents basically the same MTF of the FCR ST-VI system, in spite of the thicker phosphor employed.

In Figure 24 the differences between the MTFs calculated along the two main directions are plotted. Although all systems use a mechanical scanning along one direction, we note that some of them (*i.e.* Kodak and Agfa units) presented small differences, whereas others (especially FCR ST-VI and FCR Velocity) showed more accentuated variations.

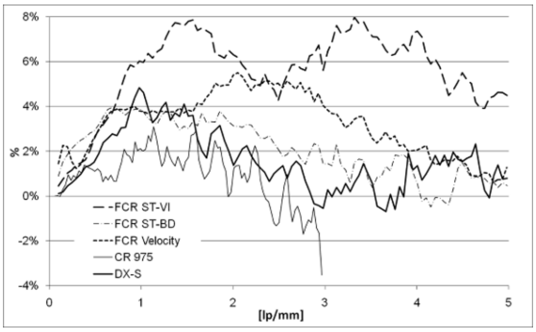

Figure 24. ***Plot showing the difference of the MTF calculated on the two directions for the five CR systems. Some systems shows very small differences whereas other present more clear variations on the MTF in the two directions.***

These results could be also explained by taking into account the 2D NNPS shown in Figure 25 (for an exposure of 5 µGy). All systems except CR975 appears to use a software filtering acting differently on the two directions. In particular, the FCR ST-VI unit have a remarkable difference between the NNPS on the two directions as if a low pass filter has been used only on the horizontal direction. This effect was detectable with lesser intensity in the FCR Velocity system most likely because of the different reading technology (line scan), while it was practically undetectable in the dual-side reading technology (FCR ST-DB). In this case the different behavior along the two directions appears to be due to an anti-aliasing filter used in the majority of FUJIFILM systems, as noted in other studies [63,64,65]. The FCR Velocity spectrum shows very low values along the horizontal axis: we believe that this contribution is lowered through a software filtering process. The Kodak and Agfa systems have an almost perfectly isotropic response, as shown also by the small differences of their MTF along the two directions. The DX-S unit has a spectrum with some equispaced hollows along the vertical axis that could be caused by a sort of notch filtering applied during the reading process.

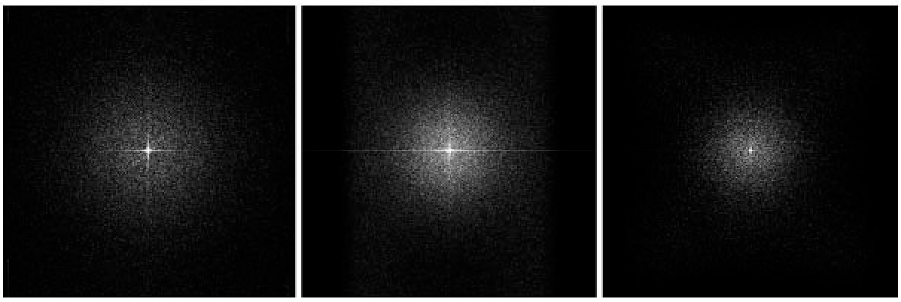

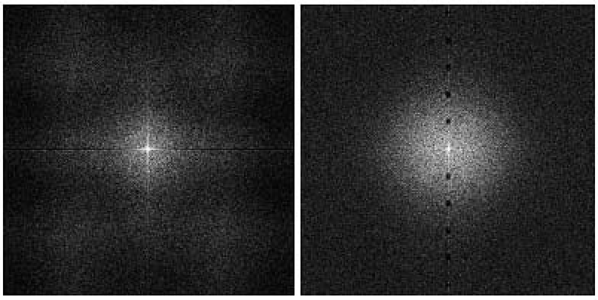

Figure 25. ***Example of 2D NNPS image for the five systems. Top row: CR975 (left), FCR ST-VI (center), and FCR ST-BD (right). Bottom row, FCR Velocity (left), DX-S (right). All systems, except CR975, seem to present a software filtering acting differently on the two directions. This effect can be observed undoubtedly for the FCR ST-VI unit: it shows a clear difference between the NNPS on the two directions. A slighter but marked difference is present also for FCR Velocity. The different behavior for the two directions should be due to the fact that FUJIFILM systems use an anti-aliasing filter. The DX-S unit presents some frequencies missing along one axis, probably caused by a sort of notch filter applied to the images.***

Figure 26 shows the 1D NNPS results obtained on the radial direction from the 2D NNPS, ignoring values along the principal axes. It is worth noting as the two systems based on the dated technology (FCR ST-VI and CR975) have a remarkably higher noise for all the investigated exposures. This difference is evident at frequencies up to about 3.5 lp/mm, while it diminishes at higher frequencies. Again, we note that this is connected to the improved detection efficiency of the three advanced systems, as a result of the greater thickness of the phosphor layer (for FCR Velocity and DX-S) and the dual-side reading (for FCR ST-BD).

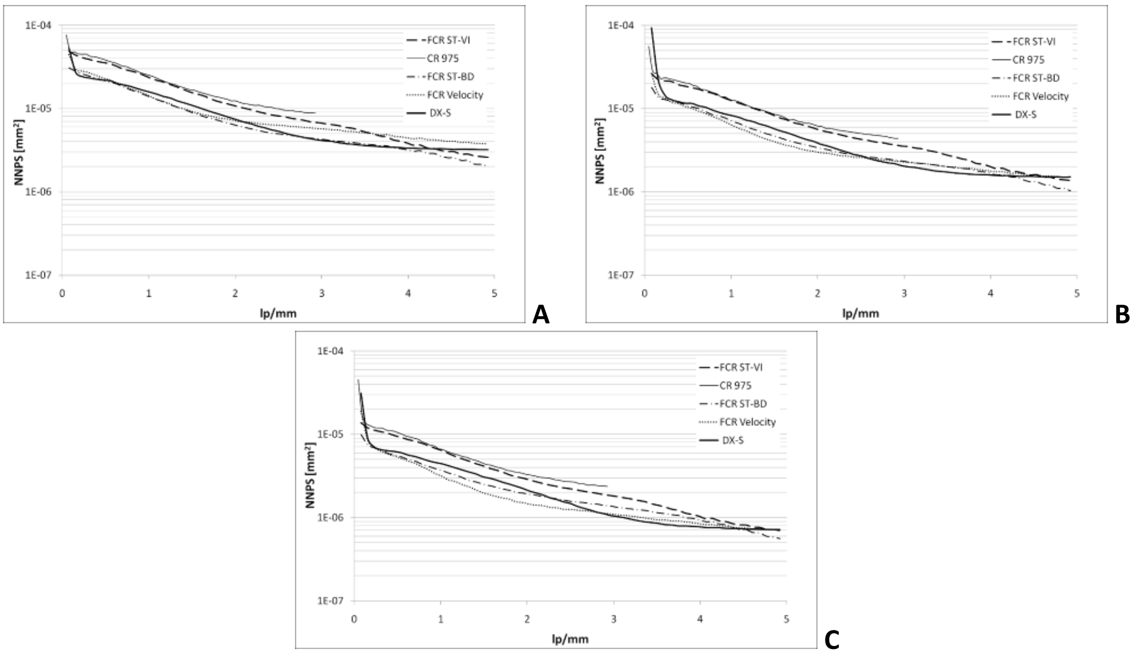

Figure 26. ***1D NNPS for the five systems at the three investigated exposures: 2.5 µGy (A), 5 µGy (B), and 10 µGy (C). 1D NNPS is obtained on the radial direction from the 2D NNPS.***

Figure 27 shows the RSD plotted as a function of the air kerma for the five systems. The experimental data are fitted with the function given in Eq.1 and the fitting functions coefficients are summarized in Table 4.

Components	FCR Profect ST-VI	FCR Profect ST-BD	CR975	FCR Velocity FP	DX-S
Poisson: α	*$1.5 \cdot 10^{-3}$*	*$1.1 \cdot 10^{-3}$*	*$1.4 \cdot 10^{-3}$*	*$1.2 \cdot 10^{-3}$*	*$1.2 \cdot 10^{-3}$*
Multiplicative: β	*$6.6\ 10^{-5}$*	*$6.8\ 10^{-5}$*	*$1.2\ 10^{-4}$*	*$1.7\ 10^{-5}$*	*$3.0\ 10^{-5}$*
Additive: γ	*$1.0\ 10^{-10}$*	*$8.9\ 10^{-6}$*	*$1.0\ 10^{-8}$*	*$3.2\ 10^{-4}$*	*$5.2\ 10^{-4}$*

Table 4. ***VALUES OF THE MAIN NOISE COMPONENTS FOR THE FIVE SYSTEMS, AS ESTIMATED BY RSD ANALYSIS.***

These parameters can help to understand the different components of the noise. A major outcome of this analysis is that for all the systems the statistical noise is dominant: in fact, the multiplicative and additive components are always smaller and often negligible, with respect to the statistical noise. As a consequence, this suggests that all the CR systems examined in this study are able to work in quantum noise limited condition. We also note that the two units based on the latest technology present an higher additive noise and a smaller multiplicative noise, with respect to the other systems. The high additive noise should be related to the CCDs used in line scanning technology, whose additive noise is intrinsically higher than that of the PMTs used in the standard CR systems [8,13].

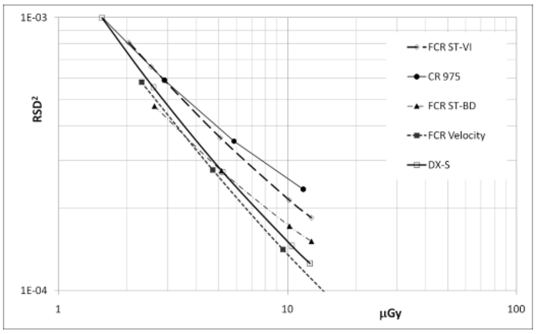

Figure 27. RSD analysis: experimental data for RSD2 values (points on the graph) and the fitting curves used for estimating the various components of the systems' noise, as described in Eq.1. The coefficients of the fitting functions are summarized in Table 4.

Figure 28 shows the product of NNPS multiplied by the exposure (air kerma), as a function of the spatial frequency. This product remains constant for every exposure, when a detector is quantum noise limited. In fact, we notice that all the systems, thanks to their low additive noise, are limited by statistical noise for the entire range of investigated exposures. Further, at the highest exposure (10 µGy) a slightly worse response is observed in detectors with higher multiplicative noise (FCR ST-VI, FCR ST-BD, and CR975) due to the overwhelming multiplicative component.

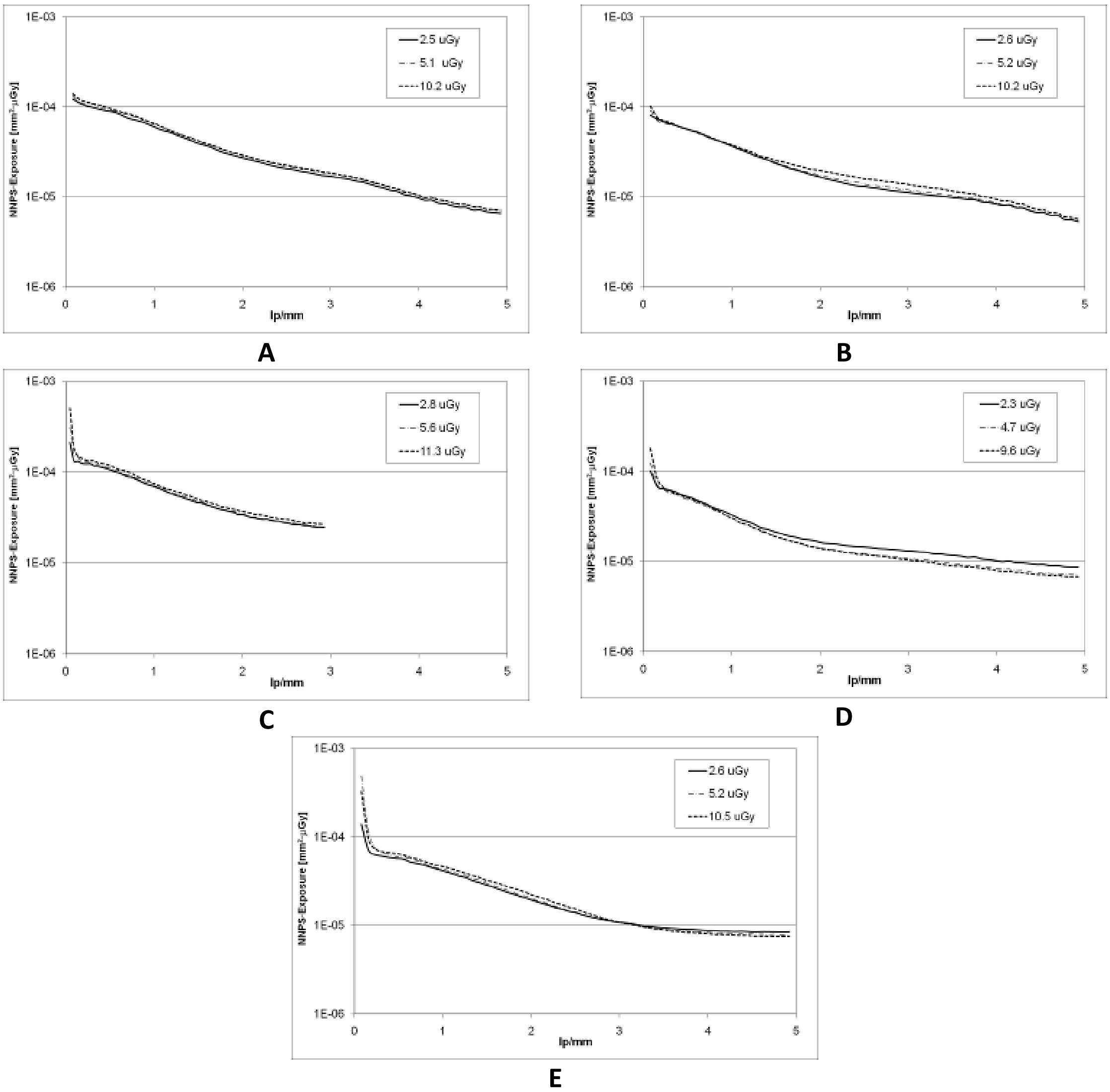

Figure 28. NNPS multiplied by air kerma for the five systems and three different exposures (2.5, 5, and 10 µGy). The five plots represent the investigated systems: FCR ST-VI (A), FCR ST-BD (B), CR975 (C), FCR Velocity (D), and DX-S (E).

DQE results are shown in Figure 29 for the three exposures. Systems based on the new technologies show DQE values roughly twice as better than those for standard CR units - especially at low frequencies - as a consequence of the overall improved efficiency due to increased thickness of the columnar phosphor (FRC Velocity and DX-S), and to the dual-side reading (FCR ST-BD). All detectors have the typical behavior of CR systems, namely DQE increases with decreasing exposures [66]. As for the line scanning technology, at low exposures the DX-S showed a slightly better performance compared to FCR Velocity, whilst results are inverted for high exposures, especially at middle-low frequencies. This could be related to the thicker phosphor used in FCR Velocity and to the fact that the higher multiplicative noise of DX-S increases its weight at high exposures. Dual-side reading and line scanning systems are quite similar, but the latter technology show an improvement at frequencies higher than 1.5 lp/mm. It is worth remarking that at low frequencies the units based on columnar phosphors have DQE values quite similar to those of the dual-side reading, whereas differences appear at high frequencies, especially for the DX-S unit. This improvement is due to the better response, in terms of spatial resolution of the needle-shaped scintillator.

As already noted, all the systems have DQE almost independent from the exposure, revealing a quantum noise limited condition for all the investigated exposures. These results agree reasonably with other results obtained for the same systems in similar conditions [13,65,67]. The improved DQE can be exploited either to enhance the image quality, or to reduce the dose to the patients, as already assessed by other researchers [68]. The DQE of the three best systems investigated in this paper is also comparable to some of the flat-panel detectors for radiography available on the market [15,69,70].

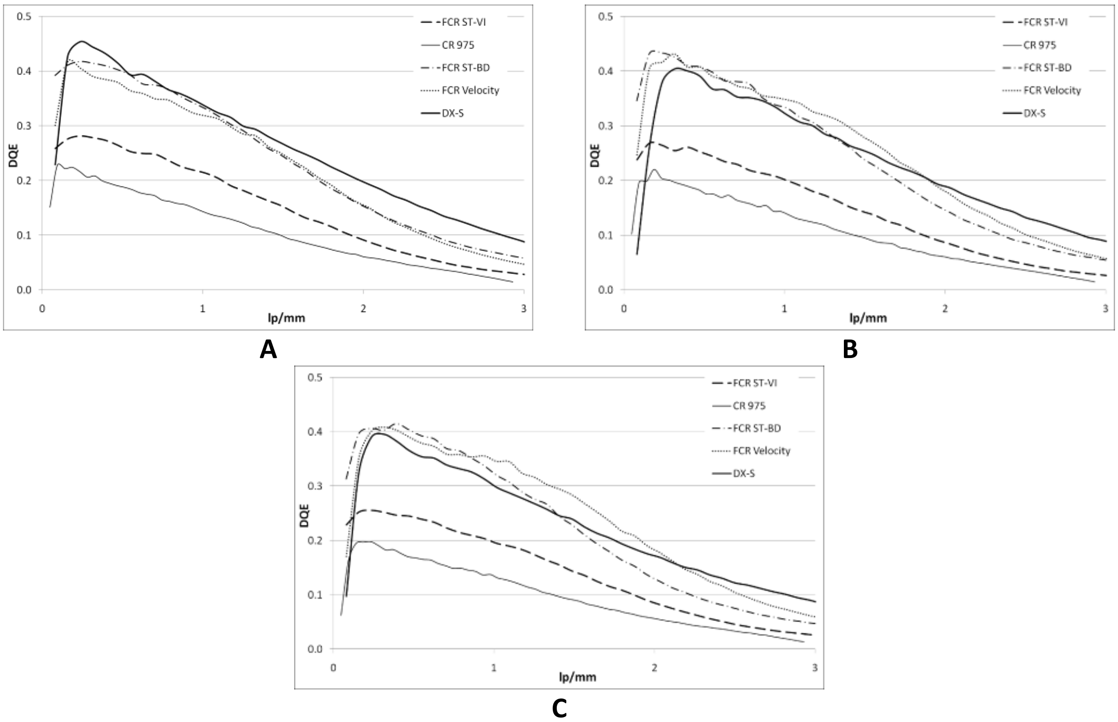

Figure 29. ***DQE for the five systems at the three investigated exposures: 2.5 µGy (A), µGy (B), and 10 µGy (C). The two systems based on the more outdated technology (granular phosphor with single-side reading) present DQE values worse than the other systems in the entire range of frequencies for all the investigated exposures. All the detectors show DQE nearly independent from the exposure, revealing a quantum noise limited condition.***

Figure 30 shows the CD curves obtained by the five systems at an exposure of 10 µGy. Once again, the systems based on the latest technologies offer better results, with respect to the conventional CR units, especially for medium-large details. That confirms that the improved efficiency helps to achieve a lower contrast threshold. In fact, for details with a diameter greater than 1 mm, the FCR ST-VI and the CR975 systems present a statistically significant different response, with respect of both the FCR Velocity unit (with $p < 0.01$), and the DX-S system ($p < 0.05$). The same trend for the CD curves can be observed at the other two investigated exposures, even if for the lowest exposure no statistically significant differences were observed. Our results agree with other studies that showed that CR systems with needle phosphors have superior image quality when compared with the conventional ones [71,72].

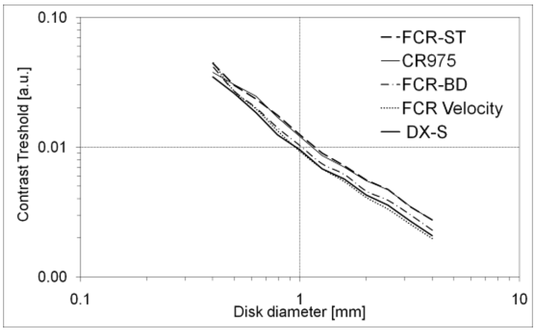

Figure 30. ***Contrast detail curves for the five CR systems at an exposure of 10 µGy . The trend of the CD curves for the other exposures is similar to this one. The three CR systems based on the latest technologies show a better response also in terms of CD visibility.***

3.1.3. Discussion

The most advanced units based on columnar phosphors provide spatial resolutions not lower to those obtained with conventional CR systems, in spite of their thicker phosphors. On the other hand, the greater thickness of the columnar phosphor allows for an improved efficiency and hence better noise properties. In fact, the standard CR systems present a remarkable higher NNPS at all investigated exposures, especially at frequencies up to 3.5 lp/mm. As a consequence, the three units based on columnar phosphors and line-scanning reading, or granular phosphor and dual-side reading, provide DQE values noticeably better than the conventional CR systems. Actually, DQE of about 40% are easily achievable at all the investigated exposures. These values are comparable to those obtained with some of the flat-panel detectors for radiography available on the market. The contrast detail analysis by means of an automatic reading of the CDRAD phantom basically confirms the superiority of the most advanced systems.

In conclusion, this analysis suggests that CR systems based on the most advanced technologies (dual-side or line scanning reading, columnar phosphors) provide a remarkable improvement of performance, with respect to conventional CR units, giving results comparable to those achieved by most flat-panel detectors for radiography.

3.2. CHARACTERITAZION OF A THICK a-Se FP DEDICATED TO RADIOGRAPHY

Abstract

Here is presented a physical and psychophysical characterization of a new clinical unit for digital radiography based on a thick a-Se layer. We also compared images acquired with and without a software filter (named CRF) developed for reducing sharpness and noise of the images and making them similar to images coming from traditional Computed Radiography systems.

The characterization was achieved in terms of physical figures of merit (MTF, NPS, DQE), and psychophysical parameters (contrast-detail analysis with an automatic reading of CDRAD images). We accomplished measurements with four standard beam conditions: RAQ3, RQA5, RQA7, and RQA9.

The system shows an excellent MTF when the CRF filter is disabled and MTF in line with other systems when the filter is activated (about 50% and 20% at the Nyquist frequency, respectively). The DQE is not very much affected by the CRF filter and is about 55% at 0.5 lp/mm and above 20% at the Nyquist frequency. On the other hand, the contrast detail curves are comparable to some of the best published data for other systems devoted to imaging in general radiography.

As normally happens with detector based on direct conversion, the system presents an excellent MTF. The improved efficiency caused by the thick layer allows getting good noise characteristics and DQE results better (about 10% on average) than many of the CR systems and comparable to those obtained by the best systems for digital radiography available on the market.

Systems based on a-Se are excellent for the high spatial frequencies required for mammography. However, their quantum efficiency (QE) is a function of X-ray energy. Chest radiography is performed at high kVp and because of the relatively low atomic number of Se a much thicker layer is required than for mammography, making a-Se systems less suited for chest radiography [73,74].

A new direct conversion detector for digital radiography recently (2010) entered in the market of digital radiography [75]. This system, manufactured by FUJIFILM and named AcSelerate, makes use of a fullerene (C60)-doped polymer layer placed on a thick a-Se layer (1000 μm) coupled to an a-Si TFT array. The C-60 doped polymer layer should lead to improved lag characteristics and is supposed to prevent the crystallization of a-Se. Further, the thick a-Se layer should help to improve the overall efficiency of the system by decreasing its noise and keeping a very good spatial resolution at the same time. The QE of this detector, as derived from Monte Carlo simulations, is 93%, 75%, 58%, and 41%, for the RQA3, RQA5, RQA7, and RQA9 beams, respectively.

The quality of the clinical system (named FUJIFILM FDR AcSelerate) is characterized, from a physical point of view, in terms of MTF, NPS and DQE and , from a psychophysical point of view, in terms of contrast-detail analysis. It is also compared images acquired with and without a new software filter (named CRF) developed by FUJIFILM for reducing sharpness and noise of the images and make them similar to images coming from traditional CR systems.

3.2.1. Materials and methods

Table 5 summarizes the main characteristics of the investigated system. A wide range of uniform exposures were used to calculate the system response curve. The average pixel value was estimated from a Region Of Interest (ROI) located at the center of the detector. We then performed a characterization of the FUJIFILM AcSelerate unit, by measuring both physical properties, such as MTF, NPS, DQE, and psychophysical figures (CD analysis). The DQE was estimated according to the international standard IEC 62220-1 [41]. We acquired images by considering four different standard beam conditions: RQA 3,5,7, and 9, according to IEC-61267 standard [76]. We measured the exposure to the detector with a calibrated ionization chamber (UNFORS Xi, Unfors Instruments, Billdal, Sweden). The source-to-image distance was about 180 cm. AcSelerate employs the usual image processing technology used by FUJIFILM for their CR systems. In fact, users are required to choose among one of the processing methods (automatic, semi-automatic, FIX mode, and others). The FIX-mode is the only one that allows users to select the sensitivity (S) and latitude (L) values, such that the pixel values in the resultant image are directly linked to exposure in a manner that mimics a film screen system. All the images used in this work were acquired with the FIX-mode processing using the following two sets of reading process parameters: S=200 and L=2.

Manufacturer	**FUJIFILM**
System	*AcSelerate*
Detection type	*Direct Conversion*
Detector material	*aSe*
Detector thickness [um]	*1000*
Imaging area [cm×cm]	*43×43*
Array size	*2880×2880*
Pixel pitch [micron]	*150*
Image depth [bits]	*12*

Table 5. *MAIN CHARACTERISTICS OF THE INVESTIGATED SYSTEM.*

Given the very good spatial resolution of a-Se detectors, especially in the high frequency region, AcSelerate images are expected to present a very high sharpness. However, an excellent MTF is not always effective, given the possibility that image information (noise) above the Nyquist frequency could be aliased to frequencies below the Nyquist sampling frequency. Thus, FUJIFILM has developed an appropriate software filter, which aims to modify the sharpness of the images coming from AcSelerate. This has been done in order to make them similar to images coming from traditional CR systems. In fact, the image processing tools available within the AcSelerate workstation are the same present in all the CR manufactured by FUJIFILM, except a new filter named CRF. CRF is supposed to provide better noise properties and same sharpness as CR. For users that prefer traditional CR images and dislike noisy images, the CRF filter should be activated. The default setting is "OFF", thus the CRF filter must be turned on by users through the acquisition console. The filter is integrated in the acquisition software (CRF option), and the user can decide to view images with or without it. The CRF filter is available only on the acquisition console. Once the image is acquired, one can decide to apply or not apply the CRF filter, even afterward the acquisition, provided that this procedure must be done on the acquisition console. Thus, images with or without the CRF filter come out from the same acquisition, and the data can be post-processed at any time on the acquisition console. This filter should influence both signal and noise power spectra in almost the same proportion, leading to small changes on DQE. On the other hand, the visibility of different details could be affected by changing the characteristics of the system. Thus, contrast-detail (CD) results could reveal a different behavior, caused by the software filter.

Firstly we determined the response curve of the system for all the investigated beams by acquiring images within a wide range of uniform X-ray exposures. The response curves were fitted with a logarithmic function and used for linearizing all the acquired images. We measured the pre-sampling MTF with the edge technique: an oversampled Edge Spread Function was obtained by a Tungsten edge test device (TX5, IBA Dosimetry, Schwarzenbruck, Germany). We estimated the MTFs both in the horizontal and vertical directions. We then averaged the MTF along the two directions for calculating the final DQE. NPS was computed by acquiring flood images at various exposure levels ranging from 1 to more than 10 µGy. For each exposure the 2D NPS was obtained from averaging the Fourier transformations of fixed-size ROIs extracted from four different images. The 1D NPS was then extracted from the 2D NPS on a radial direction at 45°, excluding the values along the axes. For a more complete evaluation of the noise properties of the detector, we also implemented the Relative Standard Deviation (RSD) analysis [9]. We estimated the RSD on the same ROIs used for NPS calculation. The RSD squared data measured at each exposure were fitted as in Eq.1. For each considered X-ray beam, we used tabulated data for the photon fluence. The final DQE is then calculated as in Eq.3.

The psychophysical characterization was assessed by performing a contrast-detail analysis with an automatic reading of CDRAD 2.0 (Artinis, Medical Systems B.V., Zetten, The Netherlands) images. For each exposure level four images were acquired. The exposure values were the same as those used for the physical characterization, this with the implicit assumption that the X-Ray absorption for the CDRAD phantom was about 25%. The phantom was repositioned after each exposure.

The CD analysis was carried out in two different ways: with human observers and with software which performs an automatic reading. Human observers evaluated images on two dedicated high resolution reference monitors (Barco MGD521, 2048×2560 matrix, 8 bit, max luminance: 600 cd/m^2). The visualization parameters (brightness, contrast, magnification factor) were fixed at the same value for all the observers. Readers have all the time they need for reading each phantom image. Five experienced operators evaluated the phantom images by using a dedicated software described in section 2.2.2.. For each reading of the phantom a CD curve was computed, by fitting the reading data with a Weibull function. Given that the estimation of CD curves by means of a method based on SNR can be misleading for images when a filtering is applied, in this paper we used the automatic reading only for images obtained without the CRF filter [77]. On the other hand, in some cases a comparison gained with human observers is presented for images with and without the CRF filter. We also estimated the theoretical CD curves, as obtained by the well-known Rose model [53]. According to this model, for a circular target of diameter α, the contrast threshold (C_{TR}) can be calculated as Eq.4.

We conducted a non parametric test (Mann-Whitney) to test if CD curves were significantly different by means of the SPSS package (version 13.0; SPSS Inc., Chicago, IL, USA). A p-value of less than 0.05 was considered to indicate a statistically significant difference between two curves.

3.2.2. Results

For each quality beam in the analyzed dose range the response curves were fitted with a logarithmic function as shown in Figure 31. All fittings were achieved with R^2>0.99. Note that, like most of the systems manufactured by FUJIFILM, the system presents a logarithmic behavior for all four beams [14,28]: all measurements were performed on linearized images.

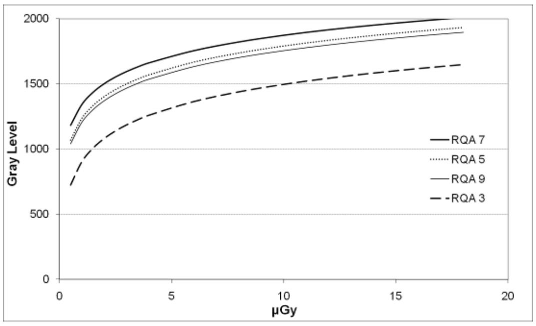

Figure 31. Response curves for the four investigated beams (RQA3, RQA5, RQA7 and RQA9). The response is logarithmic for all the X-ray conditions and fittings were achieved with a R2>0.99.

Figure 32 reports the MTF for the four investigated beams at an exposure of about 6 µGy for images acquired with and without the CRF filter. The plotted curves were obtained as the average of the MTFs estimated on the two orthogonal directions. The MTF was found to be almost independent of the beam quality and exposure level, at least in the range of investigated exposures (from 1 µGy to 20 µGy). To calculate the DQE, the mean of the MTF along the two orthogonal directions was considered.

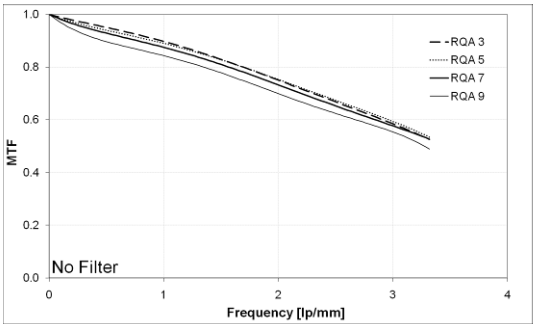

A

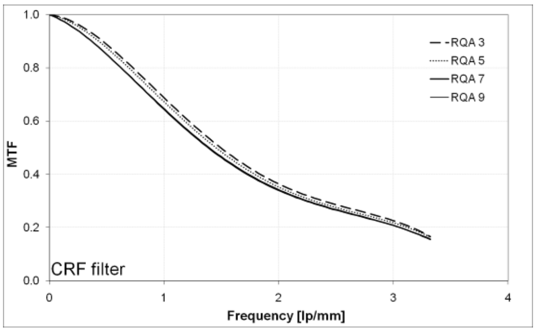

B

Figure 32. MTF estimated with the edge technique for the four investigated beams for images acquired without (A) and with (B) the CRF filter. The four beams provide a similar MTF over the entire range of frequencies. We did not see appreciable differences between the MTF along the horizontal and vertical direction. Here we show the MTF resulting from the average on the two directions. The CRF filter considerably affects the MTF, decreasing the spatial resolution of the system.

In Figure 33 we present a picture of the 2D NPS for images with and without the CRF filter, calculated for RQA5 at 6 μGy. The system presents basically a white noise that becomes a noise decreasing with frequency when the CRF filter is enabled.

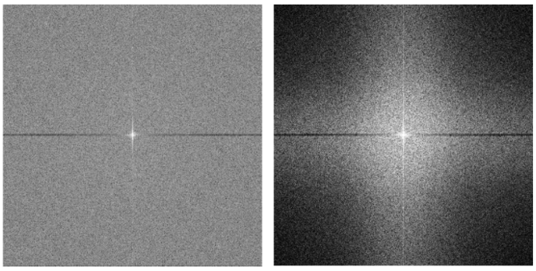

Figure 33. Example of the 2D NPS for the RQA5 beam for images acquired at the same exposure with and without the CRF filter, respectively on the right and on the left. The effect of the filter is to reduce the high-frequency noise. It is worth noting that the contribution along the horizontal axis is lowered at almost all the frequencies.

Figure 34 shows an example of 1D NPS estimated for images acquired with the CRF filter on three different directions: horizontal, vertical, and along a radial line at 45° from the principal axes. While we cannot perceive any differences between the horizontal and vertical direction, the NPS estimated along the radial line is fairly different. For images acquired without the CRF filter, the noise estimated along the three directions is mostly the same. The same behavior can be observed for the other beams and exposure levels. To compute the DQE for images with the filter enabled we used the NPS estimated along the radial direction.

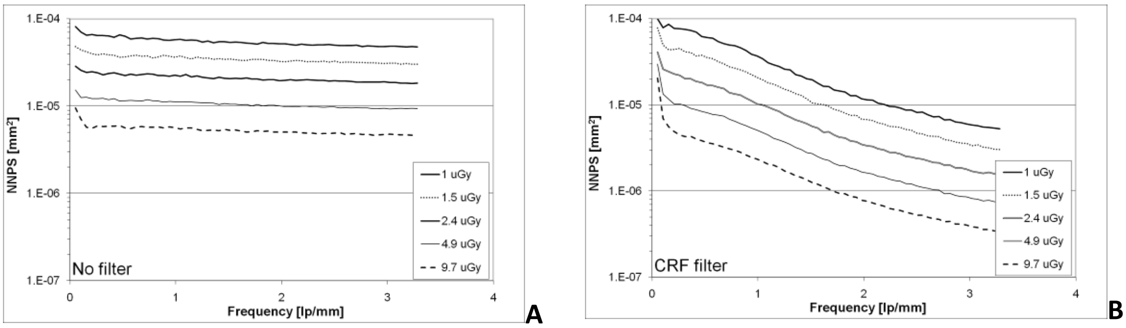

Figure 34. ***NPS for the RQA5 beam at different exposures for images acquired without (A) and with (B) the CRF filter. 1D NPS was computed along a radial line of the 2D NPS. The system presents basically a white noise, which becomes a noise decreasing with frequency when the CRF filter is activated.***

Figure 35 shows the 1D NPS calculated for the RQA5 beam at various exposure levels for images acquired with and without the CRF filter.

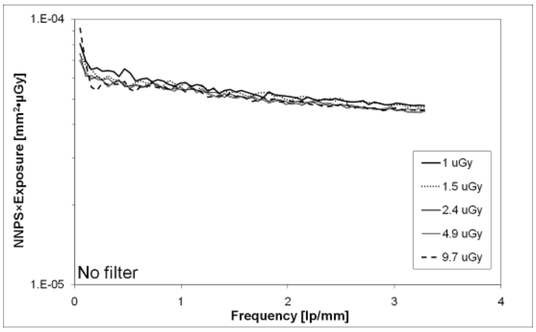

Figure 35. ***NPS multiplied by air kerma for the RQA5 beam for images acquired without the CRF filter. This product should be independent from the exposure, for a strictly quantum noise limited detector.***

For achieving the RSD analysis, we used the same ROIs considered for NPS estimation. The experimental data were fitted with the function given in Eq.1; the coefficients of the fitting functions are summarized in Table 6 for the four beams and images acquired with and without the CRF filter. These parameters correspond to the different component of the noise. The system always presents a very small, in fact almost negligible, multiplicative component with respect to the other components. Even the additive component is smaller than the quantum one (about one order of magnitude lower) in all the investigated conditions. This behavior has been assessed over the entire range of investigated exposures (from about 1 to 10 µGy).

Components	**RQA3**	**RQA5**	**RQA7**	**RQA9**
Poisson: α [µGy]	*$2.2 \cdot 10^{-3}$*	*$2.1 \cdot 10^{-3}$*	*$2.3 \cdot 10^{-3}$*	*$3.2 \cdot 10^{-3}$*
	$4.9 \cdot 10^{-4}$	*$5.2 \cdot 10^{-4}$*	*$4.1 \cdot 10^{-4}$*	*$5.5 \cdot 10^{-4}$*
Multiplicative: β	*$1.0\ 10^{-6}$*	*$1.0\ 10^{-5}$*	*$1.0\ 10^{-7}$*	*$3.6\ 10^{-6}$*
	$7.7\ 10^{-7}$	*$2.0\ 10^{-7}$*	*$1.0\ 10^{-7}$*	*$6.3\ 10^{-6}$*
Additive: γ [µGy]	*$1.2\ 10^{-3}$*	*$6.7\ 10^{-4}$*	*$9.1\ 10^{-4}$*	*$1.1\ 10^{-3}$*
	$6.6\ 10^{-5}$	*$5.0\ 10^{-5}$*	*$2.2\ 10^{-4}$*	*$3.9\ 10^{-4}$*

Table 6. Values of the noise components for the four X-ray beams, as estimated by RSD analysis. The top row represents values for images acquired without CRF, whereas the bottom row represents values for images acquired with CRF enabled.

For a strictly quantum noise limited system, the product of the NPS and the exposure air kerma should remain constant for all exposures. Figures 36 and 37 illustrate this product for images acquired without the CRF filter for the RQA5 beam and for all the beams at an exposure of about 3 μGy, respectively. From Figure 36 we may note that this product is basically constant for all the exposures, revealing that the detector is working in a quantum noise limited condition, at least within the range of investigated exposures.

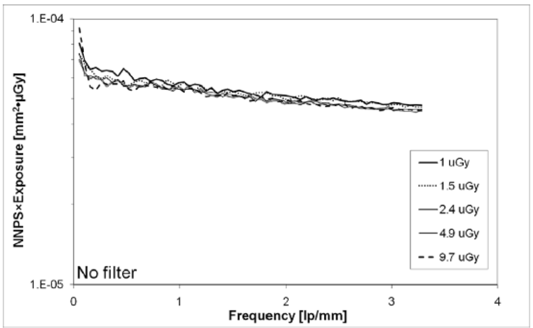

Figure 36. NPS multiplied by air kerma for the RQA5 beam for images acquired without the CRF filter.

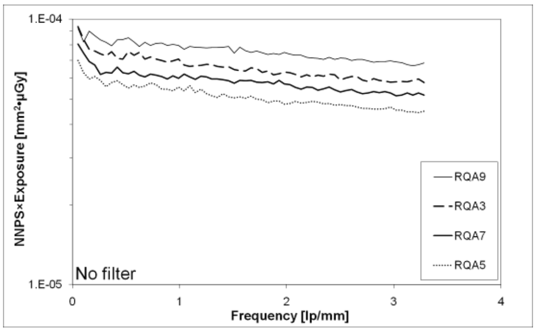

Figure 37. NPS multiplied by air kerma for the four investigated beams at an exposure of about 3 μGy for images acquired without the CRF.

Figure 38 shows that the noise of the system changes with the beam energy. In particular, the most energetic beam (RQA9) presents a worse response. These statements are still valid when the CRF filter is activated.

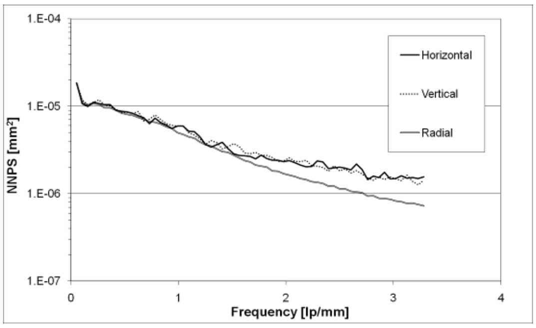

Figure 38. 1D NPS for the RQA3 beam for the same exposure estimated on three different directions: horizontal, vertical, and along a radial line at 45° for images acquired with the CRF filter enabled.

In Figure 39 we show the DQE for the RQA5 beam at various exposures for images acquired with and without the CRF filter. The AcSelerate presents a very high DQE (about 55% at 0.5 lp/mm and above 20% at the Nyquist frequency). Again, the DQE is essentially not affected by exposure, at least when the filter is not enabled, a typical feature of systems working in quantum noise limited conditions. It is worth remarking that, even if the CRF filter affects in a considerable way both the MTF and the NPS, the DQE is basically unaltered by the activation of the filter. In fact, the difference between the DQE with and without filter is also shown in Figure 39C and, apart from the initial low-frequency drop region, it is on the order of some percents.

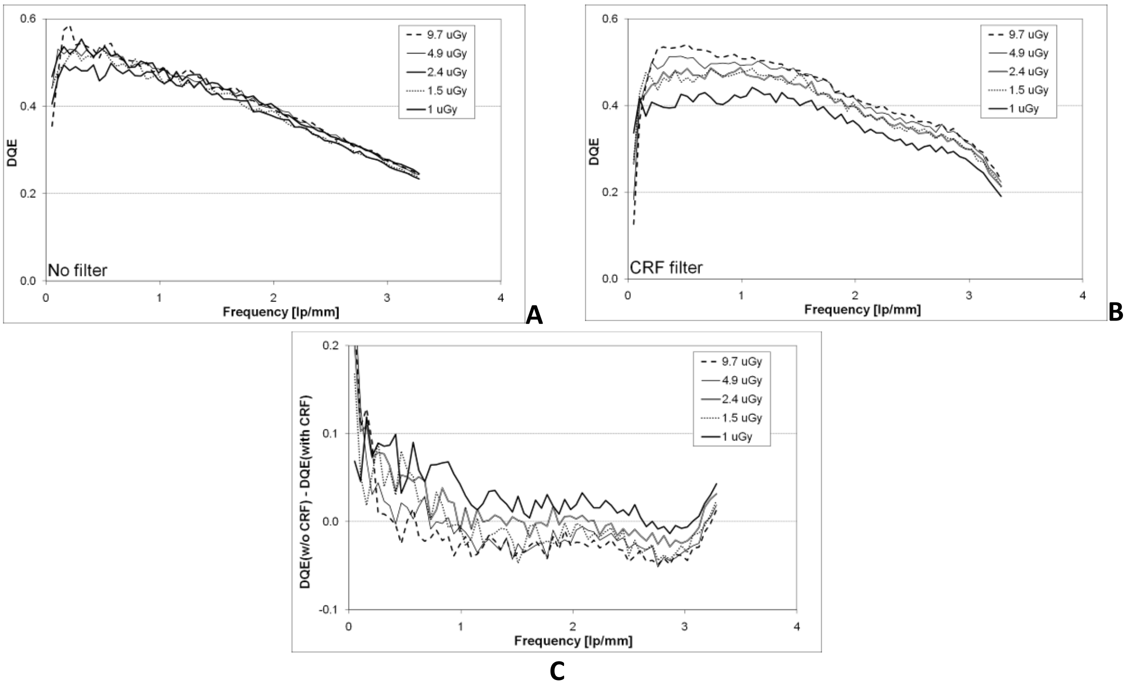

Figure 39. DQE of the AcSelerate system for the RQA5 beam at various exposures without (A) and with (B) the CRF filter. It is worth noting that the CRF filter does not produce a noticeable impact on the DQE outcomes, as shown in (C), which illustrates the point-to-point difference between the DQE without and with the CRF filter.

In Figure 40 we plotted the DQE of the system for the four X-ray beams for images acquired without the CRF filter at an exposure of 3 μGy. As expected, the DQE of the system decreases as the average energy of the beam increases.

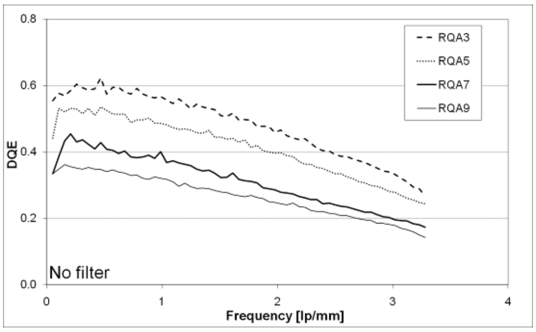

Figure 40. DQE for the four beams for images acquired without the CRF filter at an exposure of about 3 μGy . As expected, the DQE of the system decreases as the energy of the X-ray beam increases.

Figure 41 shown the CD curves calculated with the automatic software for the RQA5 beam for three different exposures (CRF filter not activated). As expected, the visibility of the details increases with exposure. Figure 42 illustrates the CD curves obtained for the four beams at an exposure of about 2.5 μGy (again, with the CRF filter not enabled). Although the difference is not statistically significant, the RQA9 beam provides a slightly worse response, with respect to the other beams.

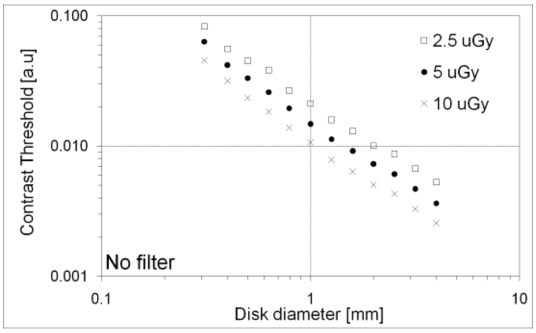

Figure 41. Comparison of CD curves obtained for the RQA5 beam at different exposures for images acquired without the CRF filter.

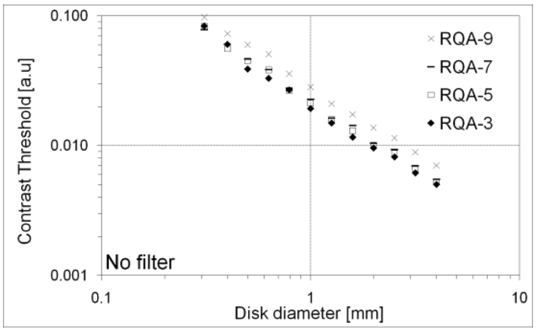

Figure 42. Comparison of the CD curves for the four investigated beams at an exposure of about 2.5 µGy for images acquired without the CRF filter.

Figure 43 shows a comparison of the CD curves estimated by human observers for images acquired with the RQA5 beam at an exposure of about 2.5 µGy with and without the CRF filter. No statistically significant differences can be noticed. We also present results obtained with the automatic method on images without the CRF filter. A good agreement between the automatic and human response can be noticed, especially for small and medium details.

In Figure 44 the effect of the CRF filter on the CD curves is shown. Here we plotted three CD curves: one coming from experimental data for the AcSelerate system (RQA5 at 2.5 µGy without the filter), one theoretical curve calculated with the Rose model, and finally one of the best curve for other systems gathered from recent published data [14]. The CD response of the AcSelerate is in line with the best published data.

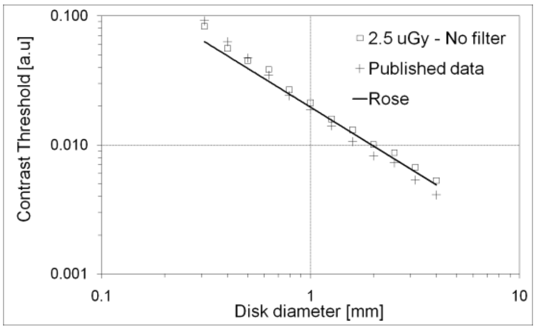

Figure 43. CD curves obtained at an exposure of about 2.5 µGy (RQA5 beam): images acquired without the CRF filter, theoretical Rose model (as described in Eq.4), and best results coming from published data for CR systems.

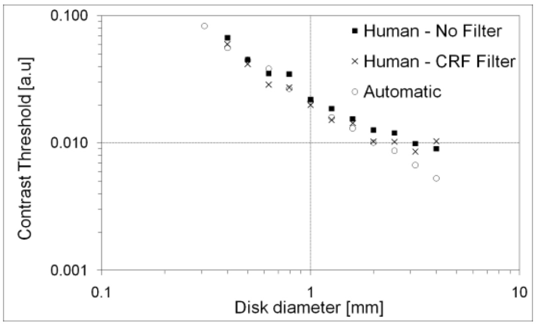

Figure 44. Comparison of the CD curves estimated by human observers for images acquired with the RQA5 beam at an exposure of about 2.5 µGy with and without the CRF filter.

3.2.3. Discussion

Although AcSelerate is a system based on direct conversion, its response curve is logarithmic, just as all the systems manufactured by FUJIFILM. Further, the response curve presents the lowest sensitivity for RQA3 beam and its maximum for RQA7 beam, as already noted and measured for other detectors [15,78].

When images are acquired without the CRF filter, the system shows an excellent MTF, as direct conversion detectors usually do, in spite of the great thickness of its a-Se layer. When the filter is activated, the MTF diminishes considerably and becomes similar to many other systems available on the market [13,64]. Hence, one effect of the CRF filter is to decrease the spatial resolution of the system in a conspicuous way.

All the 2D spectra present very low values along the horizontal principal axis. These values appear along the entire axis, apart from a neighbor of the origin. Usually, for flat panels based on a-Se, at least one of the axes present a higher noise. The noise contribution along the horizontal axis seems to be lowered through a filtering process by software for the AcSelerate system. A similar effect on 2D spectra was already observed in other systems developed by FUJIFILM. Hence, even if we do not have many details from the manufacturer, we believe that this filter was designed to remove banding non uniformities in one of the principal directions. The second point is that, similarly to most of the systems based on direct conversion detectors, the AcSelerate shows a nearly uniform noise across the entire range of frequencies when the CRF filter is not activated. Further, it appears that when the CRF filter is activated the noise is no longer isotropic. In this case the AcSelerate system presents a noise in the proximity of the principal axes which is higher than the noise at frequencies far from the axes. This is true especially for high frequencies. Evidence of this behavior may be observed when one estimates the 1D NPS on two different directions. This behavior is not present when the CRF filter is not enabled. Thus, one of the other effects of the CRF filter is to reduce noise (especially high frequency noise) with a non-isotropic cutting of the frequencies. The RSD analysis revealed that the CRF filter helps to reduce all the noise components, for all the considered X-ray beams. From the plots showing the product of the NPS and the exposure we can recognize that the investigated system is working in quantum noise limited condition within the range of investigated exposures. The tendency of the NPS curves is similar for all the investigated beam qualities. The noise of the system changes with energy, and the RQA9 beam, as expected, shows a slight worse performance probably due to the a-Se lower efficiency at high energies.

Looking at the DQE curves the first thing that is worth pointing out is that the AcSelerate unit, thanks to the great thickness of its a-Se layer, is able to provide very good DQE outcomes. In fact, they resulted to be better than many other systems and comparable to those obtained by the best systems available on the market. These results are slightly affected by the activation of the CRF filter. One important point to keep in mind is that the CRF filter influences both the MTF and the NPS of the system, but in some way it seems not to affect too much its DQE. This means that, through the activation of the CRF filter, AcSelerate is able to provide two different images: one with excellent resolution and high noise (filter not enabled), and one with good resolution and good noise properties (filter enabled). The bottom line is that those two images are characterized by having being processed in two different ways which provide essentially the same DQE. We can note that the DQE of the system decreases as the energy increases, probably caused by the lower efficiency of Selenium at high energies.

CD results are consistent to those obtained for the DQE calculation: for each exposure level the three beams RQA3, 5, and 7 provide comparable results, while RQA9 achieves, as expected, slightly worse results (highest CD curve). It is worth noting that the effect of the CRF filter is not substantial on the visibility of CDRAD details. In fact, for most diameters a slight improvement on the CD curve can be observed, but the difference is not statistically significant.

Finally, the performance of the AcSelerate unit, in terms of CD outcomes, is comparable to some of the best published data for other systems devoted to imaging in general radiography.

3.3. CHARACTERITAZION OF A FFDM SYSTEM BASED ON OPTICAL READOUT

Abstract

To address the FP based on TFT noise problems a novel clinical system for digital mammography has been recently (2009) marketed based on direct conversion detector and optical readout. This unit, named AMULET and manufactured by FUJIFILM, is based on a dual layer of amorphous Selenium which acts both as converter of X-rays (first layer) and optical switch for the readout of signals (second layer), powered by a line light source. The optical readout is supposed to improve the noise characteristics of the detector. As it turns out the combination of optical switching technology and direct conversion with amorphous Selenium provide images both with high resolution and low noise. In this paper, we are presenting a characterization of an AMULET system.

The characterization has been achieved in terms of physical figures (MTF, NNPS, DQE) and contrast-detail analysis. We tested the clinical unit exposing it to two different beams: 28 kV Mo/Mo (namely RQA-M2) and 28 kV W/Rh (namely W/Rh).

MTF values of the system are slightly worse than those had from other direct-conversion flat panels but in range with those from indirect flat panels: the MTF of the AMULET system is about 45% at 5 lp/mm. On the other hand, AMULET NNPS results are consistently better both than those from direct-conversion flat panels (up to 2-3 times lower) and from flat panels based on scintillation phosphors. DQE results about 70% when RQA-M2 beams are used, and approaches 80% in case of W/Rh beams. Contrast detail analysis when performed by human observers on the AMULET system results in values better than those published for other full-field digital mammography systems.

The novel clinical unit based on direct-conversion detector and optical reading presents great results both in terms of physical and psychophysical characterization. The good spatial resolution combined to excellent noise properties allow the achievement of very good DQE, better to those published for clinical FFDM systems The psychophysical analysis basically confirmed the excellent behavior of the AMULET unit.

In order to surpass the noise limits associated to the TFT readout of a-Se detectors, a novel clinical FFDM system (named AMULET) has been manufactured by FUJIFILM and recently introduced in the market. The AMULET detector comprises a direct-conversion, light-reading radiation solid-state detector based on an a-Se plate. The detector basically consists of a dual layer of a-Se: the X-rays are converted into electrical signals in the first layer, and are read out in the second layer by means of an optical switch. As an alternative to the TFT procedure commonly used for FPs, here light is used as a switch for reading out electrical signals. In fact, the detector stores radiation image information based on the radiation that has passed through the breast as an electrostatic latent image, and generates an electric current depending on the latent image when the detector is scanned by a reading light applied from a dedicated source. The reading light source includes a line light source comprising a linear array of LEDs and an optical system for applying a line of reading light to the detector. The line source moves along one direction in such a way that the entire surface of the detector can be scanned. The combination of direct-conversion and the optical switching technology is supposed to provide high resolution images with low noise.

The aim of this analysis is to realize a characterization of a novel clinical FFDM unit based on a direct-conversion detector and optical readout (FUJIFILM AMULET), in terms of physical figures of merit (MTF, NPS, DQE), and psychophysical parameters (CD analysis).

3.3.1. Materials and methods

A wide range of uniform exposures were used to calculate the system response curve. From a ROI close to the chest wall section of the detector the average pixel intensity was computed. We then performed a characterization of the FUJIFILM AMULET unit, by measuring both physical properties, such as MTF, NPS, DQE, and psychophysical figures (CD analysis). All acquisitions were obtained on a clinical unit without compressor and anti-scatter grid. We acquired images by using two different spectra: 28 kVp Mo/Mo (Molybdenum anode with 30 μm Molybdenum filter, namely RQA-M2, according to IEC-61267 standard) and 28 kVp W/Rh (Tungsten anode with 50 μm Rhodium filter) [76]. We attached a 2 mm thick foil of Aluminum to the X-ray tube for simulating a low scatter condition. The exposure to the detector was measured for each investigated condition with a calibrated ionization chamber (UNFORS Xi, Unfors Instruments, Billdal, Sweden). The source-to-image distance is nearly 65 cm.

The readout system generates 16 bit linear data, and a subsequent logarithmic transform is applied to the data, giving rise to a 12 bit image. The 16 bit linear image is not accessible to users, whereas the 12 bit data is made available through one of the processing modes. All the images used in this work were acquired with the FIX-mode processing with parameters S and L equal to 121 and 2, respectively. The system was calibrated with the standard clinical procedures.

Manufacturer	**FUJIFILM**
System	*AMULET*
Detection type	*Direct Conversion*
Readout	*Optical reading*
Detector material	*aSe*
Imaging area [cm×cm]	*18×24*
Array size	*3540×4740*
Pixel pitch [micron]	*50*
Image depth [bits]	*12*

Table 7. *MAIN CHARACTERISTICS OF THE INVESTIGATED* ***FFDM*** *SYSTEM.*

The main characteristics of the investigated FFDM system are summarized in Table 7. The relevant advancement is in the combination of a direct-conversion detector based on a-Se, and an optical readout system, instead of the typical TFT readout used for FFDM detectors. Figure 45 shows a sketch of the dual layer detector employed in the AMULET system.

The detector consists of six main components: a negative top electrode, a thick X-ray photoconducting layer (PCL), an electron trapping layer (ETL), a thin readout PCL, stripe electrodes, and an optical source. The X-ray PCL is made of a layer of a-Se with a thickness of less than 200 μm [27]. Here, X-ray photons are directly converted into electron-hole pairs. Under a strong electric field, the generated electrons are then accumulated on the ETL, where a latent electron image is formed. After X-ray exposure, the negative voltage is turned off and the top electrode comes to be grounded. Trapped electrons induce positive charges on the stripe electrodes and an electric field in the readout PCL. In the subsequent readout phase, a light is irradiated from a linear optical source, which generated electron-hole pairs in the readout PCL. The so generated electrons are drifted and collected on the stripe electrodes, where they are detected as signal charges. The line source moves along a direction perpendicular to the direction of the stripe electrodes (scan direction), whereas for each position of the line source, data are readout on the direction indicated in Figure 45 (data line direction).

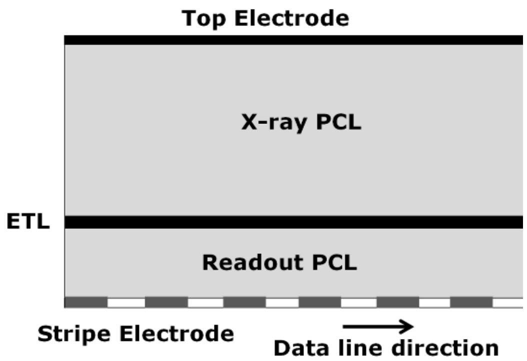

Figure 45. ***Sketch of the detector of the AMULET system. The main components of the detector are: a negative top electrode, a thick X-ray photoconducting layer (PCL), an electron trapping layer (ETL), a thin readout PCL, stripe electrodes, and an optical source.***

Pre-sampling MTF was measured by using the edge technique: an oversampled Edge Spread Function was obtained by a tungsten edge test device (TX5, IBA Dosimetry, Schwarzenbruck, Germany). The NPS was computed according to the international standard IEC 62220-1-2 at different exposure levels. The mammographic unit was characterized on a wide range of air kerma (20-150 μGy). This range was chosen to be considerably below and above the typical mammographic detector exposure range, which have a median of about 120 μGy, according to other studies [79,80]. For each exposure the 2D NPS was obtained from averaging the Fourier transformations of fixed-size ROIs extracted from four different images. The 1D NPS was then extracted from the 2-D NPS on a radial direction (at 45°) and was then normalized for the squared mean signal value of the ROI, obtaining the Normalized NPS (NNPS). The same ROIs used for calculating the NNPS were also considered to achieve the RSD analysis.

RSD (i.e. standard deviation divided by average signal value) was calculated inside the ROIs. We then fit the average RSD squared over all the ROIs using the Eq.1.

The X-ray photon fluence has been gathered from tabulated data; we then calculated the number of photons per unit area at the measured exposure. The DQE is then calculated as Eq.3.

Contrast detail analysis was carried out using the CDMAM 3.4 phantom (Artinis, Medical Systems B.V., Zetten, The Netherlands). It consists of a matrix of squares, each one containing two identical gold disks of given thickness and diameter. One disk is placed in the center and the second in a randomly chosen corner. The observer has to indicate the corner where the eccentric disk is located. The phantom covers a range of object sizes and thicknesses representing microcalcifications and small masses. The object thicknesses range between 0.03 and 2 microns of gold, resulting in a radiation contrast range of about 0.5-30% at standard mammography exposure conditions. Images were acquired in the same conditions used for the DQE calculation. We put no additional Plexiglas plates, neither below, nor above the phantom. The smallest details of the CDMAM were placed close to the chest wall side. The CD analysis was carried out in two different ways: with human observers and with software which performs an automatic reading (CDCOM). Human observers evaluated images on two dedicated high resolution reference monitors (Barco MGD521, 2048×2560 matrix, 8 bit, max luminance: 600 cd/m2). We presented the images on the dedicate monitors with the room light off and overall conditions for all the readers. The visualization parameters (brightness, contrast, magnification factor) were fixed at the same value for all the observers. Readers have all the time they need for reading each phantom image. Five experienced operators evaluated the phantom images by using a dedicated software developed by our group already tested for the evaluation of FFDM systems, and freely available at the University of Bologna Medical Imaging website (http://www.df.unibo.it/medphys/).

We acquired six images for each exposure and presented them randomly to the observers. For obtaining different realizations of the non stochastic noise, we decided to change the position of the CDMAM phantom after each acquisition. For the two investigated spectra, we read images acquired at an exposure of 70 μGy (air kerma at the detector entrance). For each reading of the phantom a CD curve is estimated, by fitting the reading data with a Weibull function. Further, we also calculated three different figures for describing the performance of the readers: COR (Eq.5), IQF (Eq.6) and IQF_{inv} (Eq.7).

We achieved statistical analysis of the CD curves by using the SPSS package (version 13.0; SPSS Inc., Chicago, IL, USA). In fact, we tested when two CD curves are statistically significantly different by performing a non parametric test (Mann-Whitney). We tested both the curves consisting of all the phantom details together, and also the subset of data including also large details (with diameter greater 0.7 mm). A p-value of less than 0.05 was considered to indicate a statistically significant difference between two curves.

3.3.2. Results

Figure 46 shows the response of the system for different acquired conditions. We fitted the experimental data with the logarithmic function shown in the plots. We can note that the system has a logarithmic behavior for both the investigated beams, as most of the Computed Radiography systems [8,13,64]. The physical characterization has then been performed on linearized images, according to IEC Standards (IEC-62220-1-2) [1].

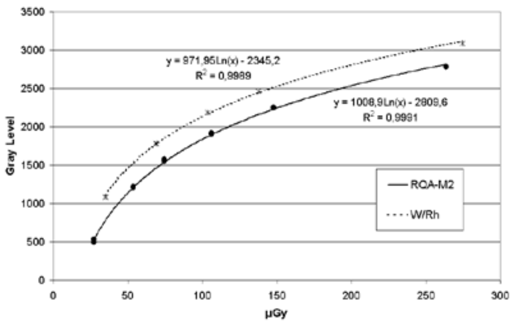

Figure 46. ***Response curves for the two investigated beams (RQA-M2 and W/Rh). In both cases the response is logarithmic and the functions used for fitting are shown within the plot.***

Figure 47A shows the MTF curves measured for RQA-M2 beam on the two orthogonal directions. For calculating the DQE, we then estimated the mean of the MTF along the two orthogonal directions. Figure 47B shows the MTF averaged on the two directions for the two investigated beams. There is also shown a plot of two MTFs collected from published values for two different FPs: a direct conversion one based on a-Se plate, and an indirect conversion based on CsI scintillator.

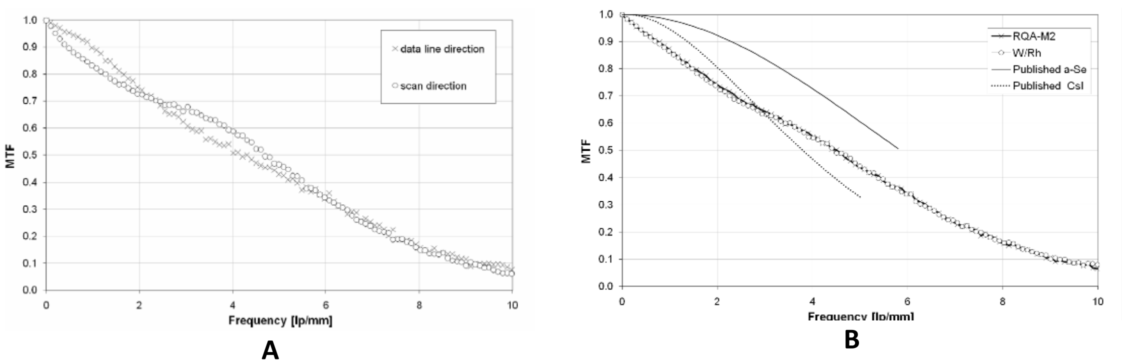

Figure 47. ***MTF estimated with the edge technique for the RQA-M2 beam (A) in the two directions (scan and data line). Some conspicuous variations arise between the two directions, especially for frequencies up to 6 lp/mm. In (B) the MTF resulting from the average on the two directions is shown for the two investigated beams. No noticeable differences are observed between the two MTFs. The plot also shows two MTF collected from published values for two FPs: a direct conversion one based on a-Se plate, and an indirect conversion one based on CsI scintillator.***

The noise components estimated by the RSD analysis are comparable to those obtained with other FPs [2]. In particular, the values achieved by fitting the RSD equation are the following: 0.009, 0.000017, and 0.8, for the Poisson, multiplicative and additive contribution, respectively. However, this variance examination does not provide information about the frequency components of the noise. Figure 48A shows an example of a 2D NNPS for the RQA-M2 beam. The gray-level scale bar connects the NNPS values in mm^2 to the gray level of the image. Figure 48B shows the 1D NNPS estimated along the two orthogonal axes, for the RQA-M2 beam at an exposure of about 150 μGy.

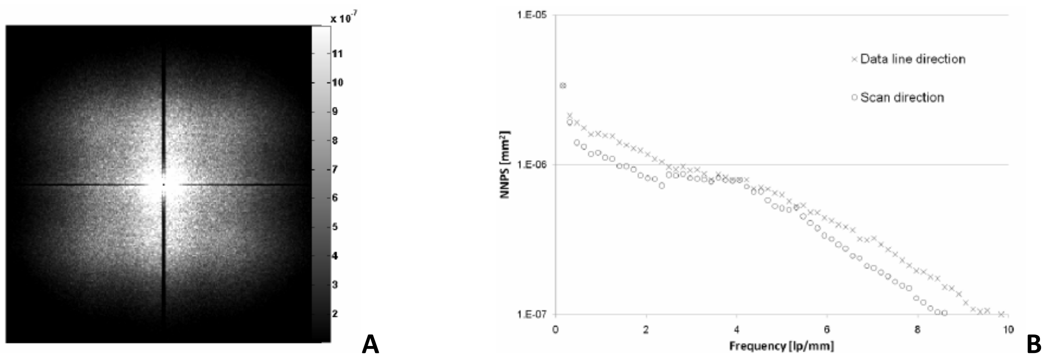

Figure 48. ***2D NPS for the RQA-M2 beam for an exposure of about 150 µGy. It is worth noting that the axes contribution are lowered at almost all the frequencies, and some sort of non-isotropic low-pass filtering seems to have been applied. The same trend can be observed at different exposures and for the other investigated beam. The gray-level bar on the right connects NNPS values in mm2 to the gray level of the image. (B) 1D NNPS for the RQA-M2 beam for the same exposure estimated on the two orthogonal directions.***

Figures 49A and 49B show the 1D NNPS for the two beams at different exposure levels. These 1D values have been calculated from the 2D spectra along a radial line at a direction of 45° and are considered for the subsequent DQE calculation.

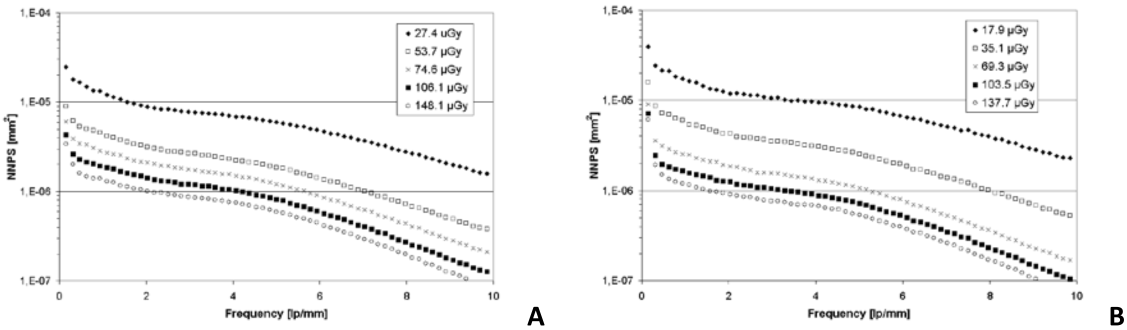

Figure 49. ***NNPS for the RQA-M2 (A) and the W/Rh (B) beam at five different exposures. 1D NNPS was computed along a radial line of the 2D NNPS. The W/Rh beam shows a slight better performance than the RQA-M2 one, when considering the same exposure.***

In order to assess the uniformity of the noise response, we calculated the NNPS by means of five different ROIs, located at various positions within the plate. The *Center* ROI is the same used in calculating the NNPS shown in Figure 50. Other four ROIs located in the proximity of the four corners of the image, named Top-Left, Top-Right, Bottom-Left, and Bottom-Right were selected, as shown in Figure 50A. We measured the exposure for each ROI separately. In fact, a maximum variation of about 20% among the exposures of the five ROIs has been observed.

The difference in the radiation field is explained by the heel effect, the increased photon path length through the window of the tube, as well as the inverse square reduction.

Figure 50B illustrates the product of NNPS multiplied by air kerma, measured for each ROI separately. In this way, we considered only variation due to the detection system. In fact, the fluctuations among the different ROIs are confined to a maximum of 3%.

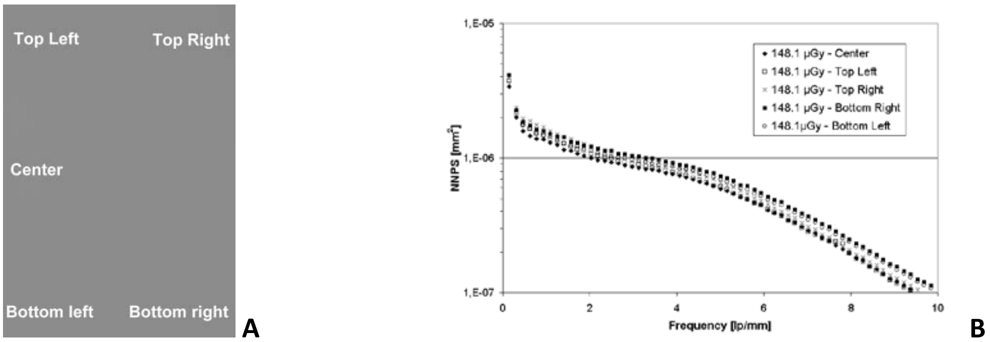

Figure 50. The NNPS has been computed in five different ROIs within the image as shown in (A): top left, top right, center (the same ROI used for estimating the NNPS shown in Figure 49), Bottom Left, and bottom right. The product of NNPS multiplied by air kerma provide very small differences among the different locations (B).

For a strictly quantum-noise limited system, the product of the NNPS multiplied by the exposure (air kerma) should remain constant, for all the exposures. It is thus possible to estimate the quantum noise limited condition, observing the value of such a product. Figures 51A and 51B show a plot of this product for the two investigated beams.

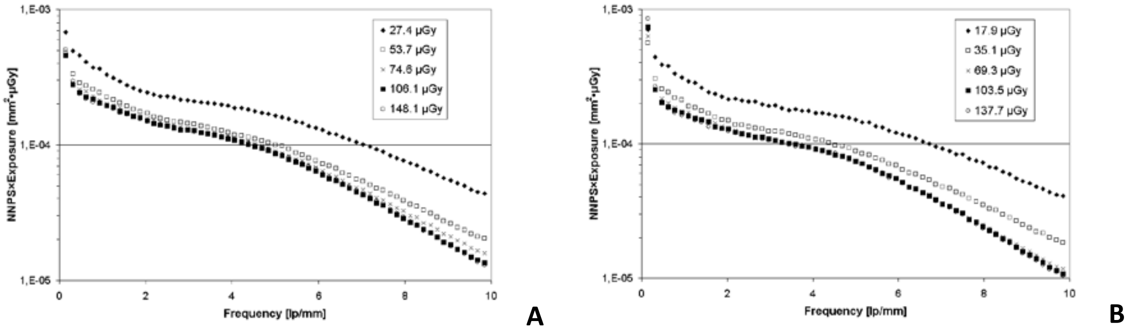

Figure 51. NNPS multiplied by air kerma for the RQA-M2 (A) and W/Rh (B) beams. This product should be independent from the exposure, for a strictly quantum noise limited detector.

In Figure 52 we compare the product of NNPS multiplied by exposure for the two investigated beams at an exposure of about 150 µGy. The W/Rh beam shows a slightly better noise performance, with respect to the RQA-M2 one. Figure 52 also shows some published data of two FPs for digital mammography.

The new data come from two different FPs: the first based on a a-Se detector, and the other one based on an indirect CsI scintillator. These data were estimated in the same experimental conditions (same X-ray beam and similar exposure values).

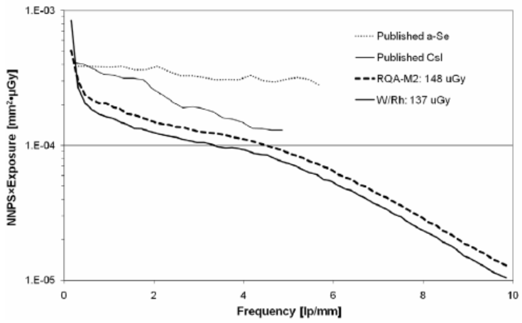

Figure 52. Comparison of the multiplication between NNPS and air kerma for the two analyzed beams for an exposure of about 140 µGy . The W/Rh beam shows a slightly better performance, with respect to the RQA-M2 one. Published data of two FPDs for digital mammography are also reported (a direct conversion detector based on a-Se and an indirect conversion one based on CsI scintillator).

In Figures 53A and 53B the DQE results for the two beams at various exposure values are plotted. This system shows a maximum DQE of about 70% for RQA-M2 and nearly 80% for W/Rh.

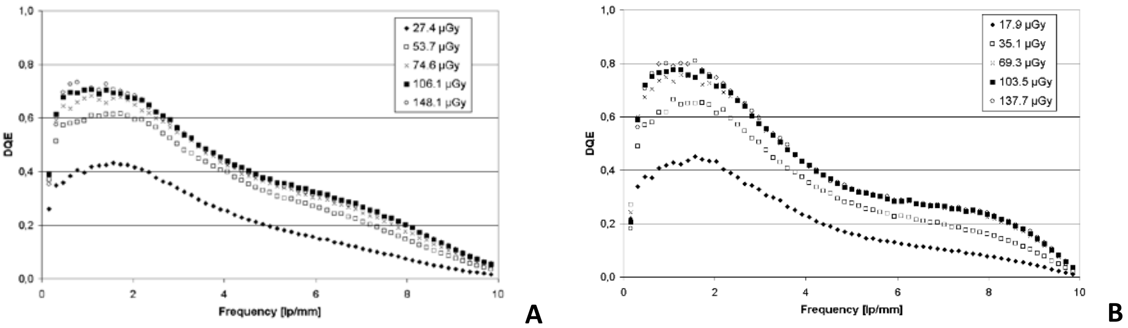

Figure 53. DQE for the RQA-M2 (A) and the W/Rh (B) beam at five different exposures. The W/Rh beam shows a better performance, with respect to the RQA-M2 one also in terms of DQE.

Figure 54 shows the DQE estimated separately on the two orthogonal axes for the RQA-M2 beam at an exposure of about 150 µGy.

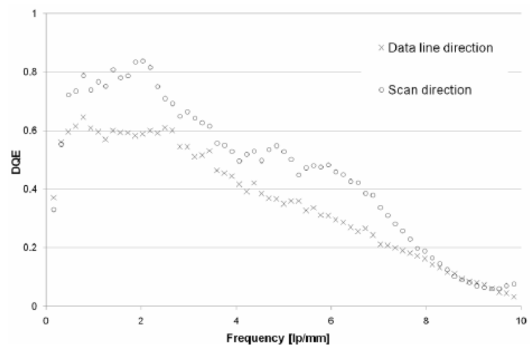

Figure 54. DQE for the RQA-M2 beam at an exposure of about 150 µGy estimated on the two orthogonal directions. Some differences arise especially at low frequencies.

Figure 55 depicts the CD curves obtained by human observers for the RQA-M2 and the W/Rh beams at an exposure of about 70 µGy. Figure 55 also shows a CD curve obtained from published values as one of the best outcomes from other FFDM systems. This curve was obtained in the same experimental conditions (X-ray beam RQA-M2, same exposure) and analyzed by human observers with the same software and visualization parameters (magnification, window/level).

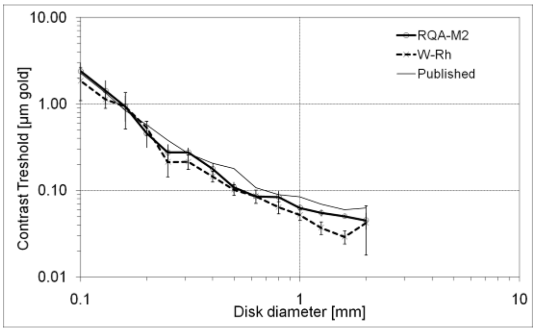

Figure 55. ***CD curves obtained by human observers for the two investigated beams at an exposure of about 70 µGy. We also plotted a comparison with a CD curve obtained in the same experimental conditions, which represents one of the best published values for FFDM systems. The error bars correspond to ± 1 standard error from the mean.***

Figure 56 illustrates a comparison of CD curves obtained by human observers, automatic methods and the Rose theoretical model for the RQA-M2 beam at an exposure of about 70 µGy. As expected, the automatic reading led to lower contrasts than those detected by human observers. In fact, both the CDMAM Analyser software and the CDCOM results fitted with the Weibull function give a nearly identical response.

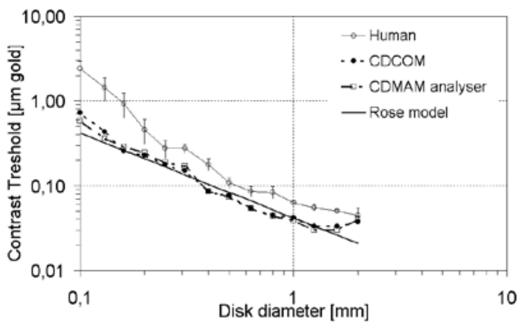

Figure 56. ***Comparison of the CD curves for the RQA-M2 beam at an exposure of about 70 µGy. We plotted the curves obtained by human observers, using two automatic methods (CDCOM and CDMAM Analyser), and with the theoretical Rose model (as described in Eq.4). The error bars correspond to ± 1 standard error from the mean. The automatic readers give a remarkable better response than that from human observers in the entire range of diameters.***

Finally, Table 8 reports the results of the CDMAM evaluation, in terms of the figures COR, IQF, and IQF_{inv} for the two investigated beams, both from human readings and from those achieved with CDCOM. It is worth remarking that in comparing the two beams no clear difference emerges. However, the W/Rh beam seems to provide a slightly better visibility than the RQA-M2 spectrum, both for human observers and for CDCOM data, especially in terms of COR. The reported values from human readers and for CDCOM analysis are better than those from other FFDM systems in similar conditions [19,81].

		Human Readers	CDCOM
RQA-M2	**COR [%]**	*58±3*	*74*
	IQF [mm·μm]	*22±3*	*11*
	IQFinv [mm μm]$^{-1}$	*4.6±0.7*	*8.8*
W/Rh	**COR [%]**	*63±4*	*79*
	IQF [mm·μm]	*19±2*	*11*
	IQFinv [mm·μm]$^{-1}$	*5.5±0.6*	*8.8*

Table 8.Values of Correct Observation Ratio (COR) and Image Quality Figure (IQF) from the human reading and the automatic reading with CDCOM.

3.3.3. Discussion

The MTF of the AMULET system presents not negligible differences between the two directions (with a maximum of about 10%), especially for frequencies up to 6 lp/mm. The MTF averaged on the two directions is almost identical for the two analyzed beams. Comparing the MTF results with published values, we can note that the AMULET's MTF despite the smaller pixel size is worse than those from other FFDM systems with a-Se plates (with a maximum difference of about 20%), whereas it is fairly comparable with the MTF obtained with FPs based on scintillation phosphors [20].

It is worth noting that the 2D noise spectrum presents very low values along the principal axes. These values are visualized in black in Figure 48A and appear along the entire axes, apart from a neighbor of the origin. The NNPS along the two axes is on average about one order of magnitude lower than the noise of the neighbor frequencies. Usually, in FPs based on a-Se, a higher noise is found along one or both axes. However, the readout of the AMULET system is completely different from other FPs. The noise contribution along the axes is lowered through a filtering process by software. This filtering is integrated in the reading step and users have no control on it. This process is designed to remove banding non-uniformities in vertical and horizontal directions. Besides, the system appears to have a slight difference behavior between the two directions. In fact, the trend of the NNPS is slightly different, since the noise in the scan direction has a great drop at low frequencies (up to 2 lp/mm), whereas it remains essentially constant for frequencies in the range 2-4 lp/mm. For frequencies greater than 4 lp/mm the noise in the two directions basically decreases with similar trend. This behavior is very similar to the one observed for the MTF calculated on the two directions, even if in that case the differences were less pronounced. The difference of the noise in the two directions reaches a maximum of about 30%.

The W/Rh beam shows a slight better performance than the RQA-M2 one, in terms of NNPS, when considering the same exposure. Further, the AMULET unit demonstrates a NNPS decreasing with frequency, whereas systems based on direct conversion generally present NNPS values fairly flat. By comparing these NNPS values with published data for FFDM systems, it turns out that the AMULET exhibits better noise outcomes, since its NNPS is lower for almost the entire range of frequencies. This confirms that the optical readout provides better noise characteristics, with respect to the readout employed in FPs. In fact, AMULET does not present an additive noise lower than other FPs, as resulting from the RSD analysis. Nevertheless, NNPS results suggest that most of the noise is confined at very low frequencies. We'd like to remark that the lower noise cannot be attributed to an increased thickness of the a-Se layer, since the AMULET detector has a PCL with a thickness of less than 200 μm, whereas other systems based on a-Se have thicknesses equal or greater to 200 μm. We note that the product of the NNPS multiplied by the exposure is almost constant for most of the exposures, except the lowest ones. In fact, the system quantum noise limit seems to be positioned at about 50-60 μGy and 40-45 μGy for the RQA-M2 and the W/Rh beams, respectively. To our knowledge, these values are pretty comparable to the quantum noise limit of other FPs. It is worth noting that the AMULET's NNPS values are up to 2-3 times lower than those from FFDM systems based on direct-conversion detectors and at the mean time noticeably better than FPs based on scintillators. In particular, the improvement of the noise properties with respect with other FPs based on a-Se increases as the frequency increases.

The increased DQE outcomes of the W/Rh beam is mainly due to the better noise characteristics of this beam, since the MTF is nearly identical to the RQA-M2 one. The fact that the use of tungsten beams can improve the image quality, with respect to the traditional molybdenum beams agrees well with other studies [82]. In particular, Hajdok et al have investigated the dependence of the Swank factor on X-ray energy and found out that a drop on the *Swank factor* (and consequently on the DQE) occurs at the K edge (i.e. about 12 keV for Selenium). This drop is due to backscatter escape of K-fluorescent photons and is responsible of an increase of the NNPS at this energy. Above this energy this drop is recovered continuously, giving rise to an improvement of the DQE as the energy increases. This suggest that more energetic spectra (e.g. with W/Rh) might produce higher quality images that the traditional molybdenum beams In fact, many digital systems are moving towards spectra with W/Rh anode/filter combinations, since this can improve the image quality, or alternatively, reduce the dose [83,84,85]. To our knowledge, the DQE results obtained with AMULET are better than most of the published values for clinical FFDM systems [14,18,22,28,86]. We believe that the very good behavior of the AMULET unit in terms of DQE is due to the combination of the good spatial resolution available for direct-conversion detectors, together with the excellent noise characteristics achievable with the optical readout. The quantum noise limited condition can also be assessed observing the exposure at which the DQE starts to decrease. These limits result to be about 50-60 μGy for RQA-M2 and about 40-45 μGy for W/Rh and agree with those estimated with the product of NNPS and air kerma.

By estimating the DQE at the two orthogonal direction, it is possible to notice that some differences arise, as a consequence of the variation on the MTF and NNPS, as already noted. These dissimilarities are marked especially at low frequencies, where a maximum difference of about 20% can be observed.

Despite its better DQE, no clear improvement emerges for the W/Rh beam and the difference between the CD curves obtained with the two beams is not statistically significant. However, in some cases W/Rh appears to provide a slightly better response than the RQA-M2 does, especially for large details. In fact, for details with a diameter greater than 0.7 mm the two curves are statistically different with $p<0.02$. The comparison with published values demonstrates that the AMULET unit is able to provide a statistically significant better response for details with diameter greater than 0.35 mm ($p < 0.02$). For small details, results agree well with the best published. We believe that the good noise characteristics of this system help observers to improve the visibility of details, since, as stated by Saunders *et al.* "the quantum noise appears to be the dominant image quality factor in digital mammography, affecting radiologist performance" [87].

The CD curve obtained with automatic methods agrees very well with the theoretical curve obtained by the Rose model. As also noted by other authors, this model matches with human data except for small details, where the effects of the human visual system become important and a more comprehensive model should be adopted for describing human observer results. The automatic reading results are comparable with those obtained on similar conditions for other FFDM systems.

In this paper we presented a physical and psychophysical characterization of a novel FFDM clinical unit based on a direct-conversion detector with optical readout. The AMULET system showed an MTF of about 45% at 5 lp/mm. This result is slightly worse than other FFDM systems with a-Se plates, but comparable to the MTF obtained with FPs based on scintillation phosphors. On the other hand, thanks to the optical reading, the novel system presented a NNPS decreasing with frequency and up to 2-3 times lower than the one obtained with FFDM systems based on a-Se detector and also noticeably better than FPs based on scintillators. The combination of the good spatial resolution and the excellent noise characteristics allows achieving a DQE better to those published for clinical FFDM systems. In fact, AMULET demonstrated a DQE of about 70% and nearly 80% for the RQA-M2 and W/Rh beams, respectively. The investigated system presented a quantum noise limited condition comparable to other systems. In fact, these limits resulted to be about 50 μGy and 40 μGy for the RQA-M2 and W/Rh beams, respectively. The psychophysical analysis basically confirmed the excellent behavior of the AMULET unit. Indeed, considering CD curves obtained by human observers, the investigated system presented better responses to those published for other FFDM systems. Also the COR and IQF values estimated for human readers and for automatic analysis with CDCOM software were better that those obtained on other FFDM systems in similar conditions.

The objective of this study is to compare the quality of clinical images of this new system with a gold standard CsI based FP detector.

3.3.4. A clinical comparison

To verify the AMULET physical and psychophysical characterization's result we compare AMULET's images to those from the gold standard FP that is the well known CsI based GE Senographe DS (GE DS) [18].

The clinical evaluation is made by comparing a set of 130 clinical studies (about 500 projections). The study population consists of patients which underwent mammography with the AMULET unit and have previously, within a maximum of 18 months, had mammography with GE DS. The image set characteristics are described as follows:

✓ The distribution of the compressed breasts thicknesses for the investigated patients is basically Gaussian, with a mean of 47.4 mm and standard deviation of 12.7 mm
✓ The patient mean age is 54 years (standard deviation 11 years)
✓ The breast density distribution such as in Breast Imaging Reporting and Data System (BI-RADS) classification [88] (1:almost entirely fat, 2:scattered glandular tissue, 3:heterogeneously dense and 4:extremely dense) is illustrated in Figure 57A

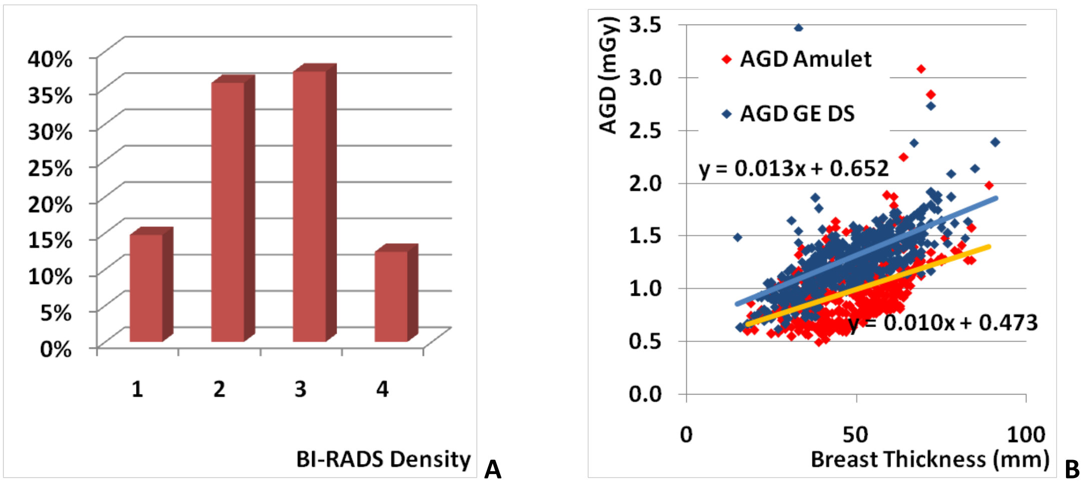

Figure 57. A) Density BI-RADS classification. B) AGD distributions for both systems.

For both the systems the automatic exposure control (AEC) standard calibration was used (Mo/Rh and Rh/Rh for GE DS and W/Rh for AMULET); average glandular doses (Eq. 12) were calculated for both systems and shown in Figure in 57B. The exposure conditions in terms of AGD was 0.97 $\pm$ 0.30 mGy and 1.29 $\pm$ 0.35 mGy for AMULET and GE DS, respectively.

The clinical comparison was achieved in terms of five different image quality features:

✓ contrast in fatty tissue
✓ contrast in fibro-glandular tissue
✓ overall sharpness impression
✓ overall noise impression
✓ and overall image quality

and the images were rated by three experienced radiologists independently.
For each paired examination all images were viewed on dedicated monitor (5 MP, 600 cd/m^2) and the image quality differences, for each image quality features, were scored with a 7-point scoring [88] scale as shown in Table 9.

Descriptor	Score
AMULET is much better than GE DS	3
AMULET is better than GE DS	2
AMULET is slightly better than GE DS	1
AMULET is similar to GE DS	0
GE DS *is slightly better than AMULET*	-1
GE DS *is better than AMULET*	-2
GE DS *is much better than system AMULET*	-3

Table 9.Image quality difference criteria and scores

Figure 58 illustrates the results for the average values of the five features used for achieving the clinical comparison. Despite the nearly 25% AGD reduction Amulet achieved a better score for all the analyzed features.

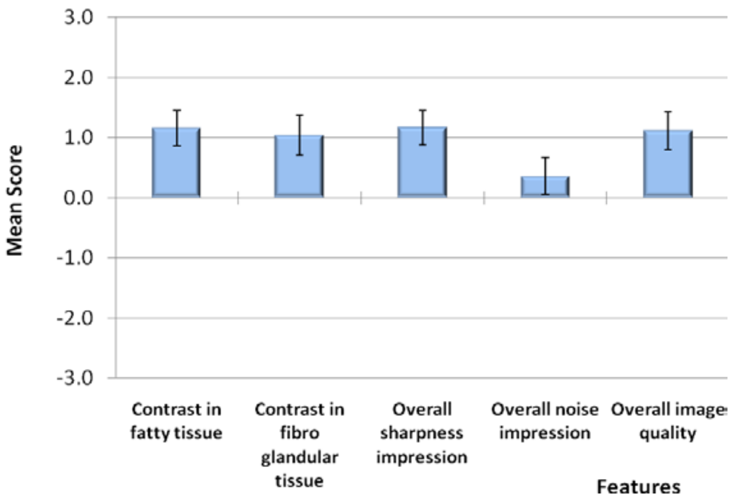

Figure 58. Results of the comparative study

The bar plot in Figure 59 shows the result scores for all the features used in the comparison.

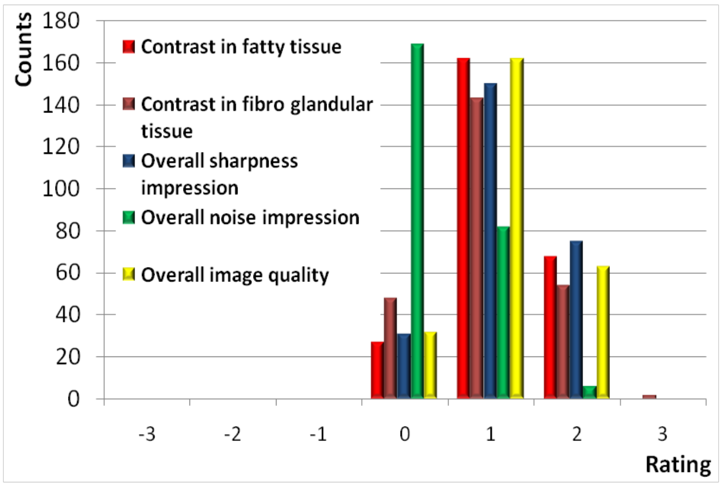

Figure 59. Results distribution for each analyzed feature

The major outcome achieved by our experiment is that the use the new technology, thanks to the optical switch, provides considerable improvements, most likely due to the excellent noise characteristics. One can take advantage of this improvement both for reducing AGD (about 25%) and for improving image quality, in terms of contrast, sharpness and noise characteristics, with respect to the FP gold standard.

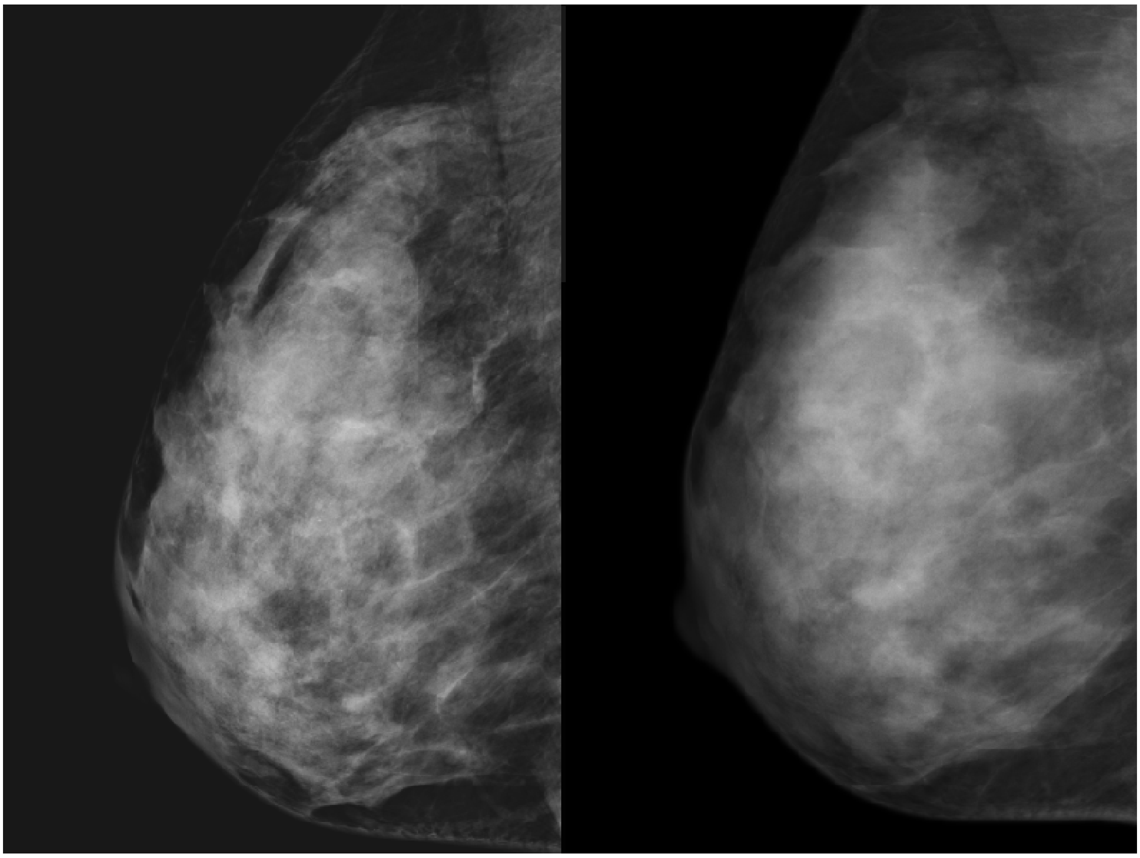

Figure 60. An example of LL exposure: AMULET's on the left and GE DS's on the right.

3.4. CLINICAL COMPARISON BETWEEN SCREEN FILM AND DUAL-SIDE CR SYSTEM IN MAMMOGRAPHY

Abstract

Digital mammography systems, thanks to a physical performance better than conventional screen-film units, have the potential of reducing the dose to patients, without decreasing the diagnostic accuracy. The purpose is to achieve a physical and clinical comparison between two systems: a screen-film plate and a dual side computed radiography system (CRM; FUJIFILM FCR 5000 MA).

The system's physical performance was tested by means of a quantitative analysis, with calculation of the modulation transfer function, detective quantum efficiency and contrast detail analysis; subsequently the results were compared with those achieved using a screen-film system (SFM; Eastmann Kodak MinR-MinR 2000). A ROC analysis was then performed on 120 paired clinical images obtained in a cranio-caudal projection with the conventional SFM system in standard exposure conditions and also with the CRM system working with a dose reduced by 35% (average breast thickness: 4.3 cm; mean glandular dose: 1.45 mGy). CRM clinical images were interpreted both in hard-copy and in soft-copy.

The ROC analysis reveals that the performances of the two systems (SFM and CRM with reduced dose) are nearly similar ($p>0.05$): the diagnostic accuracy of the two systems, when valued in terms of the area underneath the ROC curve, was found to be 0.74 for the SFM, 0.78 for the CRM (Hard Copy) and 0.79 for the CRM (Soft Copy).

The outcome obtained from our experiments shows that the use of the dual side CRM system is a very good alternative to the screen film system.

In this section is presented a comparison of a mammography dedicated dual side reading computed radiography (CRM) system with a conventional screen-film system (SFM), still the most widespread and recognized as the gold standard in mammography practice. The initial comparison has been achieved at about the same dose [89]. After that, a further comparison between the same CRM images used in the previous case and CRM images acquired at a reduced dose was accomplished.

3.4.1. Materials and Methods

The physical performance levels of SFM and CRM systems were assessed through quantitative analysis using physical characterization and contrast detail analysis. Subsequently, a Receiver Operating Characteristic (ROC) analysis was performed on a set of pairs of clinical images from a cranio-caudal view, obtained first with conventional SFM in standard exposure conditions, and thereafter with a CRM with a dose reduced by 35%.

We considered two systems, the first being the mammography-dedicated FCR 5000 MA Plus CRM unit (FUJIFILM Corporation, Tokyo, Japan). A unique feature of this system is that the storage phosphor ($BaFBr:Eu^{2+}$; pixel size: 50 μm) has a transparent support and a reading device that can detect emissions from both sides of the image plate to improve image quality [12]. This system has been approved in U.S. for full field digital mammography application.

For the physical characterization and the phantom analysis the post-processing has been used in FIX-MODE screen processing, with parameters S = 139 (sensitivity) and L = 2 (latitude). The response curve of the CRM system was determined by exposing the detector to a wide range of uniform X-ray exposures. Due to the logarithmic response of the system, all the image data used for the physical measurements were linearized by means of the fitted response function. The digital images from the CRM unit were also printed by a FUJIFILM DPL laser printer (pixel size: 50 m) and displayed on a dedicated monitor (EIZO FC-2090, 2048×1536 pixel, 8 bit and max. luminance 650 cd/m^2, EIZO Nanao Corporation, Hakusan Japan).

The second system considered was a Kodak MinR-MinR2000 SFM system (Eastman Kodak Company, Rochester, N.Y., USA). The X-ray source used throughout the study was a “Sophie” mammography unit (Planmed, Helsinki, Finland). A mammography-dedicated Kodak Miniloader Day-Light attached to a MinR processor (120 s, 35.0 °C) was used (Kodak Wratten, Eastman Kodak Company, Rochester, N.Y., USA). The clinical mammography unit and the CR receptor used undergo all the regular quality assurance checks, according to the European Reference Organisation for Quality Assured Breast Screening and Diagnostic Services (EUREF) guidelines [78]. In particular, measurements about the radiographic generation unit, the image receptor, the image quality and the image presentation were performed with the procedures and the frequency suggested by the guidelines. The AEC of the mammography unit was calibrated for the film-screen cassettes. The same setup has been used for the CR system, except for changing the exposure time, when the “low dose” condition is needed.

During the clinical trial 120 women were enrolled, as part of the conventional study, by means of a dual exposure of the same breast obtained in a cranio-caudal view with the conventional SFM in standard exposure condition and the CRM working with a 35% reduction in dose, as in the contrast detail analysis. The pairs of images were acquired in sequence without removing the compression paddle. Each woman signed an informed consent form approved by the institutional review board and the investigation was approved by the ethics committee of the Hospital. Four experienced radiologists independently assigned a Breast Imaging Reporting and Data System (BIRADS) category [88]to the SFM and CRM images using the range R1-R5. The gold standard for cases classified R4 and R5 was histological examination, while for the others the mammographic biennial follow-up was used. The set of images used consists of 34 images classified in the range R3-R5 by the radiologists panel, and 86 images classified as R1 or R2. Most of the images contain masses, microcalcifications or architectural distortions. In particular 39 masses (27 without calcifications, 4 with calcifications, 6 lymph nodes, and 2 oil-cysts), 62 calcifications (29 surgical, 19 spread, 7 clusters, and 7 vascular), and 46 architectural distortions (43 surgical, and 3 radial scar) have been considered.

To assess the image quality of the two systems, their spatial resolution and efficiency were evaluated by calculating the modulation transfer function (MTF) and detective quantum efficiency (DQE) [14,15,70], using the standard quality beam IEC RQA-M2 [76] (28 kV Mo-Mo, additional filtration: 2 mm Type 1199 Al).

Films were digitized using a high-resolution digitizer (Epson Expression 1680-Pro, Seiko Epson Corporation, Nagano, Japan) with an optical resolution of 1600 dpi × 3200 dpi. A fully characterization of the scanner in terms of MTF and NPS was obtained, according to the procedure described [90]. This characterization was used to correct results presented for the screen-film. The spatial resolution of the scanner was assessed using a test film pattern (Sine Patterns, Rochester, N.Y., USA). The noise characterization of the scanner was achieved using a set of optical gelatin filters (Kodak Wratten, Eastman Kodak Company, Rochester, N.Y., USA).

In this work the pre-sampling MTF was measured by using the slit technique: an oversampled Line Spread Function (LSF) was obtained using a 10 µm tantalum slit. Exponential fitting of the oversampled LSF was performed, in order to reduce the effect of noise in the tails. The MTFs presented are the average of those obtained along the two orthogonal axes.

DQE describes how the signal to noise ratio is distributed across the system in relation to spatial frequency. DQE was measured at different exposures and was calculated using Eq.3.

The HVL thicknesses (mm Al) were estimated from logarithmic interpolation of the measured exposure values. From tabulated data we calculated the photon fluence at the average X-ray energy considered, and the number of photons per unit of area at the measured exposure was then calculated. In view of the complexity of the analogue image digitization procedure, the DQE of the conventional system was calculated for an exposure of about 100 µGy, corresponding to an optical density of reference of 1.2 for the screen-film systems [91].

To assess the contrast-detail characteristic, we used the CDMAM 3.4 phantom developed in Nijmegen (Artinis Medical Systems B.V., Arnhem, The Netherlands). This phantom permits determination of threshold contrast (object thickness) as a function of object diameter. The results are plotted as a contrast-detail curve, presenting the observed threshold contrast for a defined x-ray exposure as a function of object size. The CDMAM consists of a matrix of squares (16 rows and 16 columns), each square containing two identical gold disks of known thickness and diameter. One disk is placed in the center and the second in a randomly chosen corner. The observer has to indicate the corner where the eccentric disk is located. The phantom covers a range of object sizes and thicknesses representing possible lesions in the breast. The object diameters range between 60 microns and 2 mm, whereas the thicknesses range between 0.03 and 2 microns of gold, resulting in a radiation contrast range of about 0.5-30% at standard mammography exposure conditions. Within a row, the disk thickness is constant with logarithmically varying diameter. The contrast-detail curve can be viewed as the “separation” limit between the two image conditions where details are visible or invisible.

Contrast-detail analysis: SFM (Standard Dose) vs CRM (Standard Dose). In this initial analysis, the phantom was exposed using both systems in accordance with the conditions specified by the manufacturer for analogue images, i.e. 28 kV (Mo-Mo) 40 mm of PMMA, anti-scatter grid, compression paddle off and a dose calculated to ensure that the mean optical density of the analogue image would correspond to 1.2 plus fog (approximately 100 µGy at the detector). Even if this optical density value is lower than those recommended by some screening programs (e.g. the NHS Breast Screening Programme), other studies suggest the optimum optical density can differ from that range and should be determined for each film-screen combination and processing condition [92]. These authors find that the optimum optical density was 1.25 for a film-screen similar to the one used in the present paper. Four images were produced for each condition and the results obtained are the average of the curves obtained from the light box readings of four skilled readers, repeated twice at least 7 days apart.

Contrast-detail analysis: CRM (Standard Dose) vs CRM (Low Dose). This second analysis aimed to quantify the reduction in perceptibility noted when the digital analysis obtained in the previous phase was compared with an equivalent obtained with a dose 35% lower. Various recent studies [93,94,95] have demonstrated that with digital mammography units it is feasible to reduce the dose within the range 30%-40% (and in some cases up to 50%), with respect to screen film systems. First, we intended to test if a reduction within that range was practicable on phantoms. After that, in the next section we assessed whether the same reduction could be achievable on clinical images, without affecting the diagnostic accuracy. Since this comparison was between two digital images, the reading was made on the computer screen, and in order to assist the operator in evaluation of the CDMAM image and reduce the statistical error in the evaluation process, a graphical user interface (GUI) similar to those described in 2.2.2. but specifically developed for CDMAM analizing. The software allows reading and recording the linearized image phantom files generated, while an operator chooses the vertex where he guesses the additional target is supposed to be clicking on one of four keys. The software is freely available at http://www.df.unibo.it/medphys/.

Four experienced operators compared two CRM system exposure conditions (four images per condition), the first (105 µGy) corresponding to the optimal exposure of the phantom for a mammographic screen-film system (standard dose), and the second (70 µGy) corresponding to a dose reduced by 35% (“low dose”).

In the perceptibility “transition region,” each target evaluation was repeated 20 times by each observer, in order to reduce the intra and inter operator statistical error and to define the contrast-detail curve we used the computation methodology proposed by Suryanarayanan [96]. In this case, the CDMAM images were evaluated by fixing to pre-defined values display parameters such as zoom, brightness and contrast.

ROC analysis. Each CRM clinical image was interpreted in both softcopy (SC) and hardcopy (HC), and both sets of HC images were viewed on a dedicated light box with a luminance of 4000 cd/m^2. To avoid the reading order effect, the SFM and CRM images were interpreted in random order (fewer than 40 different images each session).

The ROC analysis was logged using RocKit software developed by Charles E. Metz at the department of Radiology of the University of Chicago [97]; the area under the ROC curve (AUC) was calculated to compare the systems. The statistical difference between the curves obtained was calculated by means of an analysis of variance test.

The post-processing algorithm settings were fixed at the same value for all the ROC analysis at the following values: GA:1.4; GC:T; GT:1.40; GS:-0.08; MRB:C; MRT:P; MRE:0.8; MDB:E; MDT:F; MDE:0.8. These parameters define the gradation processing (respectively: *rotation amount*, *rotation centre*, *gradation type*, *density shift*), the spatial frequency processing, and the dynamic range control.

3.4.2. Results

Physical characterization. Figures 61A and B contains the results obtained from calculation of the MTF and DQE. While returning a lower MTF, due to the spread of the stimulating laser within the phosphor layer throughout the frequency range, the digital system always had a higher DQE. The DQE of the CRM system was found to decrease with increasing exposure due to an increased relative contribution of CR system noise. It is likely that the granular structure of the storage phosphor contributed to increased noise with increasing exposure at all frequency and that large area non-uniformity contributed significantly to decreasing DQE values at low frequency.

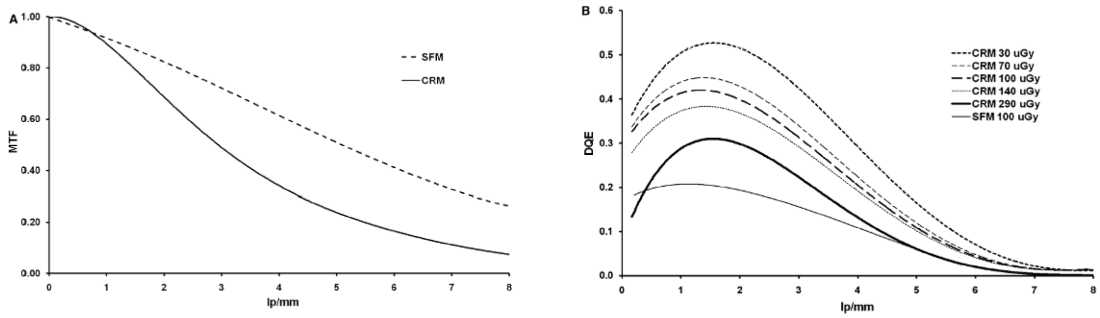

Figure 61. A) MTF: SFM and CRM systems (28 kV Mo-Mo). B) DQE: SFM and CRM systems (28 kV Mo-Mo).

Contrast-detail analysis: SFM(Standard Dose) vs CRM(Standard Dose). This analysis (Figure 62) reveals that with the same exposure conditions, the digital system always gives a better response for details larger than 150 µm in size. Conversely, the digital system gives a worse response for details smaller than 150 microns. These results agree very well with others published for comparing the same FUJIFILM CR system to similar screen-film combinations [98,99].

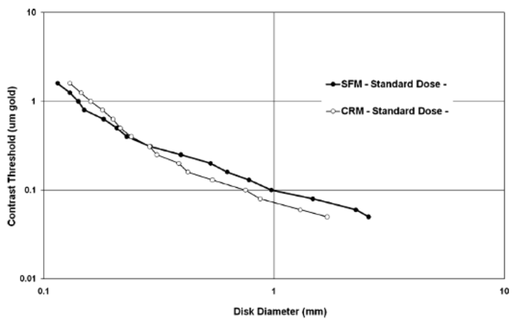

Figure 62. Contrast detail curves: SFM vs CRM (standard dose).

Contrast-detail analysis. CRM (Standard Dose) vs CRM (Low Dose). Figure 63 shows the curves generated by the averages of the readings of four expert readers, who assessed the two sets of four images acquired with the two different detector exposures of 105 µGy (Standard Dose) and 70 µGy (Low Dose) respectively. As expected, the curve relating to the exposure of 70 µGy (lower performance) is higher, but there is no statistically significant difference (Mann-Whitney) compared to the curve for the standard dose.

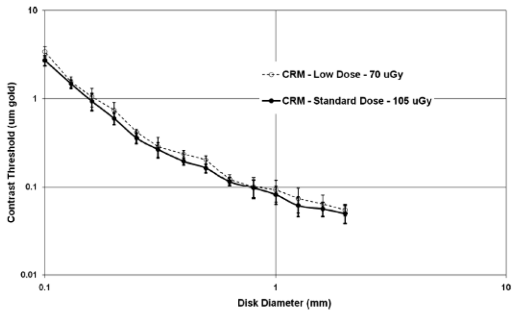

Figure 63. Contrast detail curves for the CRM system: Standard Dose vs Low Dose.

ROC analysis. The distribution of the thicknesses of the compressed breasts for the investigated patients is basically Gaussian with mean 4.3 cm and standard deviation 1.2 cm. Figures 64 illustrates the exposure conditions in terms of average glandular dose, (Eq.12) [100,101] for the SFM and the CRM systems respectively, calculated by the X-ray source output.

The average of the AGD distributions (SFM=2.22 mGy; CRM 1.44 mGy. Figure 64A and 64B reveals that the average dose used with the digital system is 35% lower than with the screen-film system.

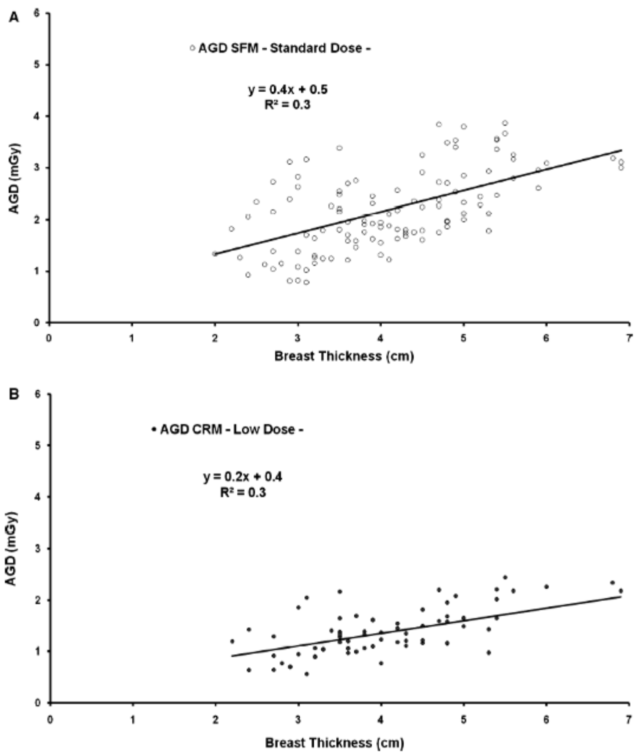

Figure 64. Contrast detail curves for the CRM system: Standard Dose vs Low Dose (A) and Average glandular dose distribution vs breast thickness for the CRM system (B).

The results of the ROC investigation of the two diagnostic systems are shown in Figure 65, with a distinction between the hard copy and soft copy readings for the digital system.

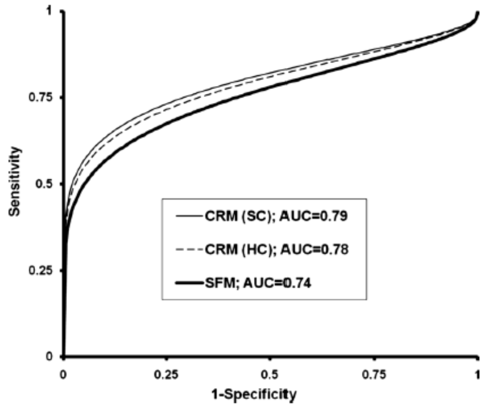

Figure 65. ***ROC curves for the SFM and CRM systems: also shown are the values of the area under the curves (AUC).***

The differences in the areas underneath the ROC curves (AUC) are not statistically significant (ANOVA: $p>0.05$); in other words, when CRM is used with a 35% reduction in dose the curves show that the diagnostic performance of the two systems is substantially equivalent.

3.4.3. Discussion

In conventional systems, the response function which defines the degree of blackening of the film in relation to the incident radiation on the detector mainly depends on the development conditions and on the characteristics of the screen-film complex. These features intrinsically determine the doses of radiation needed to obtain the highest possible diagnostic content in the image produced. On the other hand, in digital systems the user is able to obtain images of different appearance, and thus of different diagnostic content, within a broad range of administered doses therefore compared to film. Digital techniques offer significant advantages in terms of management, especially the post-processing, archiving and transfer of images.

This work aims to perform a clinical comparison between a CRM unit and a conventional SFM system, first with the same exposure conditions and then with reduced dose to the patient. To this end, it has been necessary to deepen our knowledge of the detector's intrinsic performance capabilities, and to obtain quantitative information concerning the optimal exposure condition.

The physical characterizations of the two systems has been developed in terms of spatial resolution (MTF) and contrast resolution (DQE); in particular, as related also in other studies [14], we found that the DQE of a CR system other than being greater than the DQE of the conventional SFM system has the property or returning decreasing values for increasing doses. Subsequently the contrast detail analysis were used for two main aims. In the first place to verify that the perceptive performance of the CRM system (using the default post processing settings) is at least comparable to the SFM system in the same exposure condition, as also reported by other studies [102,103]. Secondly, to investigate the loss of perceptive performance linked to the reduction of the incident dose to the detector. It should be emphasized that in the second contrast detail analysis, the images produced by the digital system were interpreted without the aid of the display tools typical of this technology, i.e. zoom, brightness and contrast, which tend to improve perceptive performance, especially for small-sized details [104]. The idea behind keeping fixed the window-level is to provide the same setting under all viewing conditions to all readers, without too much worry about the absolute performance that can be gained. We did not focus our attention on obtaining the best absolute results in term of visibility of details. Rather, we were more interested in the comparison between the contrast-detail results at the two dose levels considered.

In the clinical context the ROC analysis shows that the areas under the ROC curves for CRM (both hard copy and soft copy) were found to be basically equivalent to the screen-film method in diagnostic terms [105]. This confirms that an improved CR's DQE, compared to the conventional system, could be used to reduce the dose administered, as reported in literature for other full field digital mammography systems [106]. Other authors [107,108] have shown that the AEC can be calibrated for a better use of CR systems. This optimization could further reduce the dose, by selecting harder X-ray spectra, with respect to the screen-film systems. It is worth nothing that in our case with the CR system we were able to obtain a comparable clinical image quality with a 35% dose reduction, without performing any specific optimization about the X-ray beam. Thus, in principle a further reduction in dose could be achievable with the CR system, if an appropriate calibration of the AEC would be performed. Obviously for a CRM system the matching with an AEC system is of great importance in the clinical practice, and therefore such matching needs to be customized, according to the clinical situation.

The results obtained reveal a reassuring compatibility between phantom study and ROC curves, therefore stressing the importance of preliminary studies for successful optimization of a digital system. In this work, all images were acquired on the same mammography unit: CR technology is fully compatible with conventional Bucky tables and allows the acquisition of nearly identical images, since even the compression can remain fixed. This condition, not always achievable, offers the ideal situation for comparing both kinds of images.

A limitation of this study is that specific investigation could be required to establish whether the correlation between phantom study and clinical evaluations continues to apply in breasts with a particular configuration. A comparative feature analysis study, using appropriately selected features, such as inhomogeneous background, could provide this specific information. Another limitation of the presented study is that the number of patients enrolled is not very high. An investigation with more patients could help to improve the statistical significance of the diagnostic performance.

In conclusion, the comparison achieved in this work suggests that the use of the dual side CRM system is a very good alternative to the screen film system. In fact, the CRM is able to provide a diagnostic performance equivalent to SFM, with a 35% reduction in dose to patients.

4. CHAPTER 4: QUALITY ASSURANCE PROGRAMS

Optimization and standardization of image quality is largely based on the equipment quality and setup. The scope of quality assurance (QA) programs is to guarantee the high level of efficiency of the overall diagnostic procedure while the quality control (QC) is intended to verify the best digital images level obtainable through an acceptable patient doses, monitoring every performance such as that one that can be defined, measured and controlled.

Digital radiography depends on a number of factors such as the X-ray source, automatic exposure control, detector -just to name a few in the image production chain - hence the need of QC to get the technical optimum just as radiographers technicians and medical physicists need be involved in equipment selection, acceptance and image quality assessment.

QC employs well established procedures, measurement setup and dedicated tools (e.g. phantoms and software). Compared to those of screen film the digital radiography QC methods benefit of the full potential of digital and quantitative evaluation of image quality and of the availability of simple software to implement the data analysis. QC can be quantitative or qualitative. In the quantitative QC phantoms exposures are used to get numerical parameters linked to, e.g., noise or resolution, whereas qualitative QC is achieved through the subjective assessment - on images displayed on dedicated monitors [109] – of features such as low contrast detectability or resolution.

The increasing sophistication and resolution of modern medical imaging device leads to an increasing of difficulties in management of the assessment and quality assurance of the quick systems turnover. The large number of technological and physical approach for each imaging modalities proposed by each vendor are so different from one another that each new purchase requires a significant resources deployment to optimize the performances. Researchers and equipment vendors need to work collaboratively to develop the quantitative protocols for imaging, scanner calibrations, and robust analytical software that will lead to the routine inclusion of quantitative parameters in the diagnosis and therapeutic assessment of human health. Existing guideline for using and con trolling the new technologies do not attain nor the specific level of each appliance nor the proper insight needed in most of practical situations. In such a state, the day to day job of applying guidelines rules (whenever they exist) is a very difficult one, even for the qualified personnel in the health services.

4.1. QC Protocols

Several guidelines have been proposed to standardize QA programs such as those issued by the *American Association of Physicists in Medicine*[110], the *American College of Radiology* [111], and by the *European Reference Organization for Quality Assured Breast Screening and Diagnostic Services* (EUREF) [112] that are quite widespread in North America and Europe and include specifications of the CR, DR and FFDM's QC directed to the physical and technical matters and to the related dosimetry. Useful information related to digital mammography can be found in the ACRIN DMIST trial [113] which is a multi centre (45 different FFDM units) clinical trial designed to compare the accuracy of digital versus screen film mammography in a screening population. In this trial great attention has been paid to ensure the optimal operational consistency of the equipment - recommendations are issued by Yaffe et al. [114].

The imaging chain of digital radiography (and also of digital mammography) is formed by several parts such as the X-ray source, the AEC, the detector, the image processing and the image presentation, each of them - excluding the last two - can be probed independently, so most QC evaluate each step separately through specific sets of tests (such as in Table 10). Image quality standard (limit value) and periodicity must be established to guarantee high technical quality.

X-ray SOURCE	AEC	DETECTOR
Focal spot size	Short term reproducibility	Response function
Tube output linearity	Long term reproducibility	Noise evaluation
Tube output rate	Thickness compensation	Homogeneity
Tube output reproducibility	Tube voltage compensation	Bad pixel
Tube voltage accuracy	Average glandular dose	Ghost image
Tube voltage reproducibility		Artifacts
Half Value Layer		Threshold contrast visibility

Table 10. Some quality control parameters linked to the X-ray source, the automatic exposure control and the detector's performances.

The definition of the limiting value for each measured parameters is the main trade off implied in quality assurance programs in digital radiography. Many approaches are commonly used to define these values and they all adopt the following criteria:

1) verify that digital detector performs at least as well as conventional screen film does

2) obtain the optimal system's physical and clinical performance achievable with its specific technology and then verify that the performances level holds over long term period. Constancy testing is meant to keep high image quality over time constantly comparing the measurement values consistency with those had in the commissioning evaluation acceptance test.

4.2. Phantoms

Long term reproducibility tests are fundamental in evaluating the time stability of an imaging system which can be verified using simple test objects, usually named phantoms, which includes details simulating lesion type (several type have been developed for specific task such as in Figures 66).

A specific phantom type developed for contrast details analysis is commonly used for acceptance testing (Figure 66A). Other types have been developed for daily or weekly check in a reference setup acquisition (Figure 66B, 66C). The image quality of the phantom exposures can be evaluated in qualitative or quantitative way. In qualitative analysis the phantom's images are scored by a human observer, using image quality criteria based on detail visibility. For quantitatively analysis several automatic software have been recently developed [115] (Figure 66A, 66B) given that digital images, true to computer analysis, support objective and quantitative indices (such as described in section 2.2.2.).

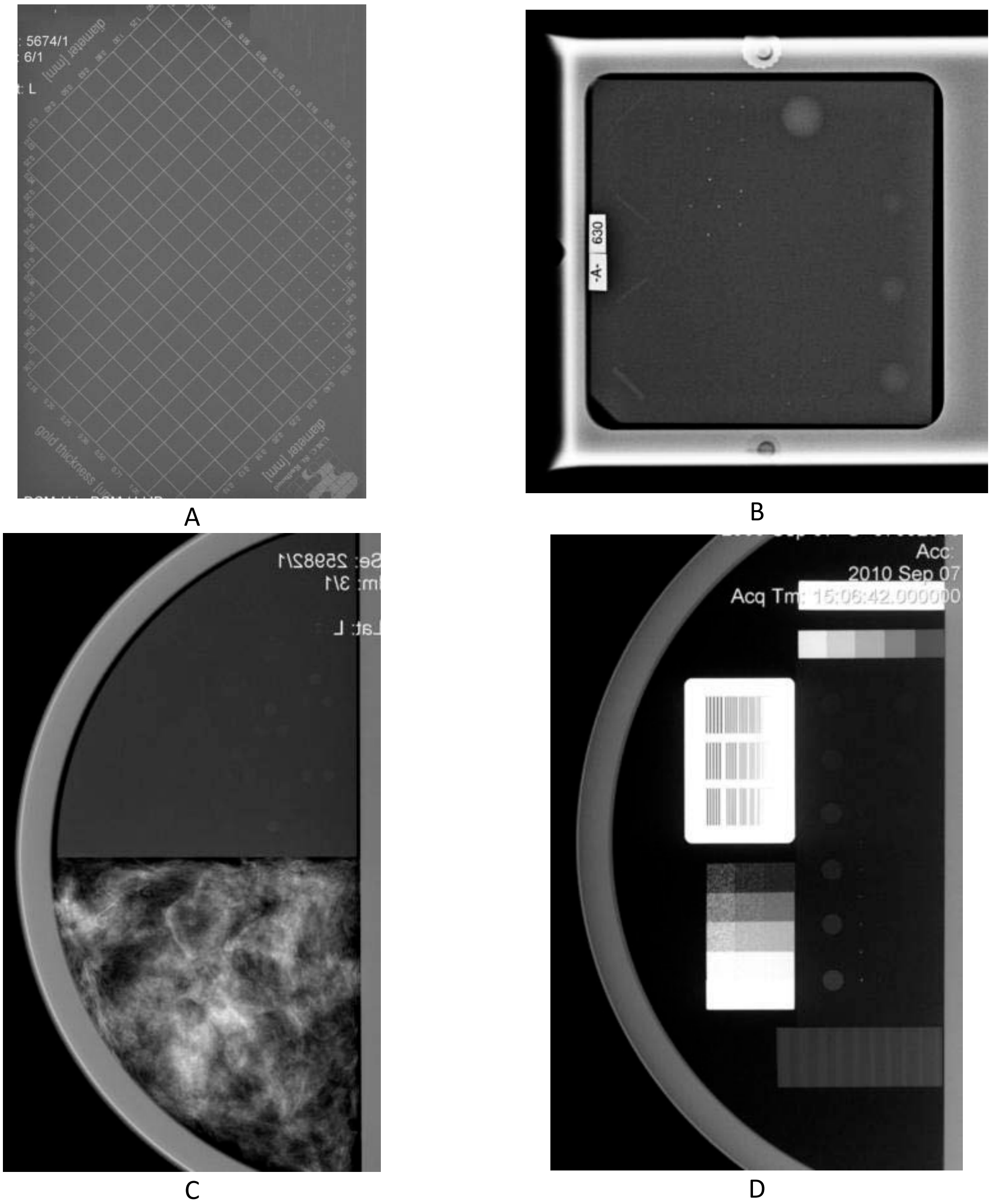

Figure 66. Some phantom's mammographic images: A) the CDMAM contrast detail phantom (Artinis), B) the ACR Accreditation phantom, C) the TOR MAM phantom (Leeds test object) and D) the TOR MAX phantom (Leeds test object).

Quantitative analysis significantly improves measurements reproducibility overcoming problems inherent in human scoring, such as the eventual inconsistence of a specific reader or variability among different readers due to subjective different thresholds decision – at the mean time reducing the resources employed.

4.3. Mammography: AEC setup and Average Glandular Dose MG

The average glandular dose (AGD) is the reference term for radiation dose assessment in mammography or rather the average absorbed dose in the glandular tissue in a uniformly compressed breast.

AGD and not Esak is linked to the biological effect's dose. AGD value depends on X-ray beam quality (HVL), breast thickness and composition. If breast thickness and composition are unknown, AGD can be referred to the standard breast. Many papers address the AGD evaluation in mammography [116,117,118], which, according to Dance et al. [100], is defined as:

$$AGD(mGy) = Esak(mGy) \cdot g \cdot c \cdot s \qquad \text{Eq.12}$$

where:

Esak is the air kerma (mGy) at the upper surface of the breast evaluated without back scatter,

- ✓ "g" is the incident air kerma to AGD conversion factor,
- ✓ "c" corrects for any difference in breast composition from 50% glandularity,
- ✓ "s" corrects for any difference due to the use of an X-ray spectrum different from Mo/Mo.

To optimize the dose an automated exposure control system is used to ensure the optimal exposure of the image receptor and compensating for breast thickness and composition.

4.4. A plugin for digital detector characterization

In this section a software developed by the Medical Imaging Group at University of Bologna for assisting users in achieving a physical characterization of an X-ray digital imaging system and in performing the most common image quality checks is presented. The software has been implemented as an ImageJ [119] plugin (based on Java platform). In this way, all the functionalities of the ImageJ suite can be used with our software. Further, users (staff working in radiological departments, such as medical physicists, physicians, engineers) are facilitated, since the plugin is integrated in a suite widespread and it is familiar for most of the physicists of the medical imaging community. The availability of such a software will allow the radiological departments and the technical correlated departments to benefit of a freeware, accurate and flexible set of software procedures. These procedures could help to avoid that people from each radiological departments spend a lot of time to produce by themselves similar tools or procedures. Further, also departments with no expertise in some specific procedures or lacking human resources able to implement such software can access to these tools for free. Finally, this could help to spread out a sort of standardization of all the procedures and techniques for most of the quality assurance checks.

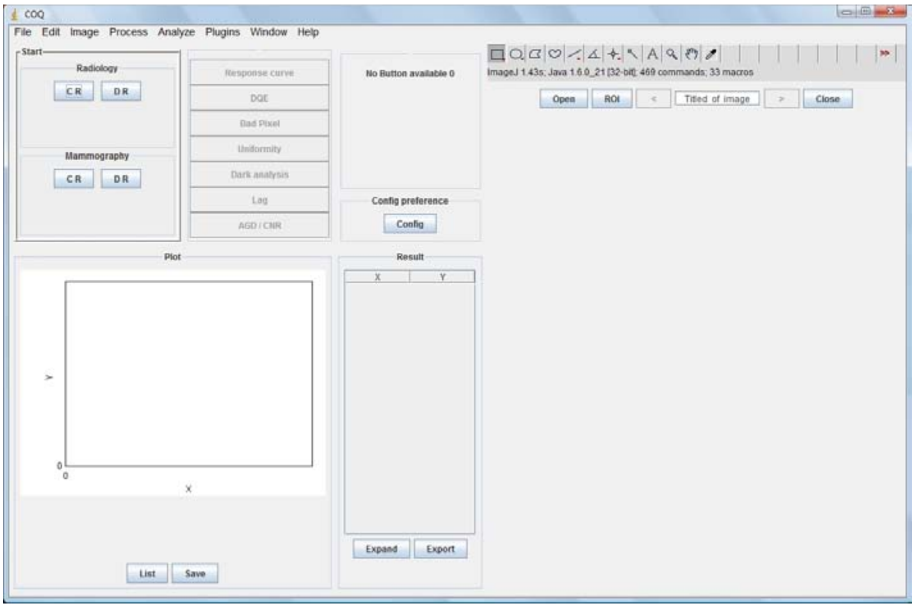

Figure 67. Main window of the ImageJ plugin developed for performing the physical analysis and the image quality checks.

The software developed can be used with images coming from different modalities (radiology, mammography) and assists users in calculating various physical parameters such as the response curve, Modulation Transfer Function (MTF), Noise Power Spectra (NPS), Detective Quantum Efficiency (DQE). In particular, the MTF can be estimated both with the slit and the edge techniques. Some parameters can also be estimated for achieving an image quality control of the investigated system. Results can be displayed as text and graphical plots and can be exported for further processing. All the operations can be done in a very easy and friendly way, thanks to the strict interconnection with the ImageJ framework. The software was designed in conformity of the following strategies:

✓ platform independence: this guarantees a more easy and wider distribution of the software

✓ modularity: it means that essential parts of the project are independent and can be replaced by another implementation without changing code. This will help upgrades and/or personalization of the program

✓ configurability: it means that an user can configure many parts of the software to better fit his needs

This software is freely available and can be downloaded at the website http://www.df.unibo.it/medphys/. As in Figure 67 the window covers all the screen and can be divided in three sections. The first one (upper left) contains the buttons for choosing the operations that the user want to perform. The second one (right) displays the image (or images stack) used for achieving the results of the chosen operation. The third one (lower left) shows the results obtained, both in textual and graphical way. Users can configure some options (e.g. the possibility of opening more than one image at the same time, using data in external files for computing some parameters, and others), by using the Config button. In the following is described the main functions implemented in the plugin, divided into two classes: physical characterization parameters and image quality checks. At this point, four different classes of functions are implemented, according to the two analyzed modalities (mammography and general radiography) and two technologies (direct radiography and computed radiography). Most of the functions are the same for all the four options, whereas some specific issues are considered for each of the option (e.g. the beam spectra tabulated for mammography are different to those used in general radiography).

The first outcome that can be achieved is the response function of the system. To this end, some flood images at various exposure levels shall be acquired, in a range of exposures compatible with clinical conditions. A suitable fitting function can be estimated with the plugin, chosen among the most common one (see Figures 68 and 69). The fitted function can be used as conversion function, in order to obtain a linearized image, with respect to the exposure. When the conversion function is already known, users can directly insert its parameters through a dialog window.

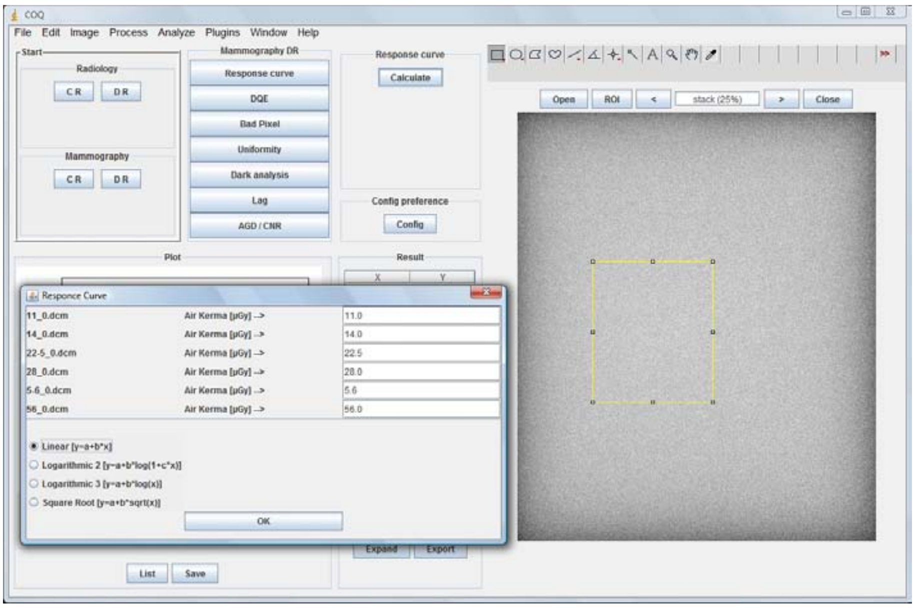

Figure 68. ***Example of the calculation of the response curve. Users must provide a set of good images, and associate to each one the correct exposure value, using the window shown on the left. Here, users can also choose some fitting functions, for fitting the data at the various exposure values.***

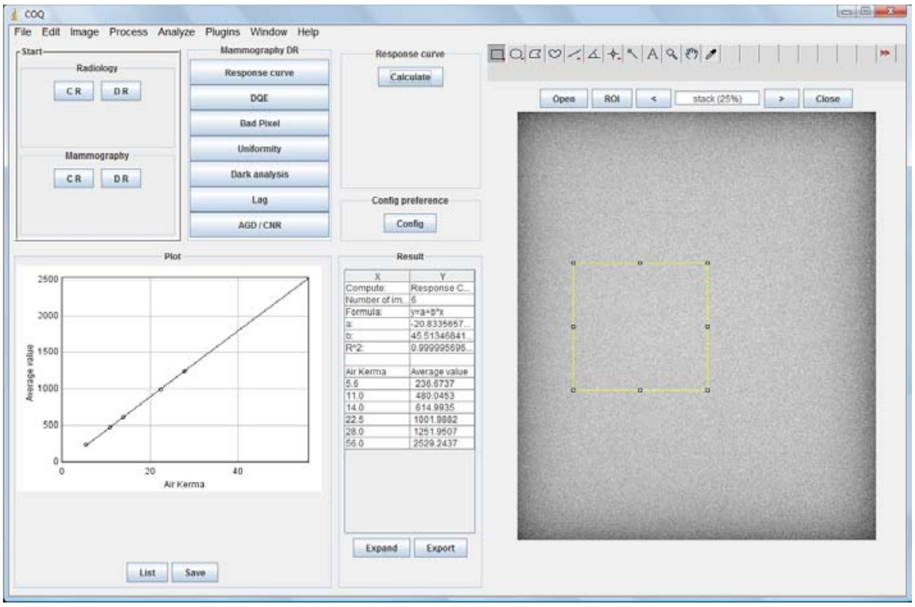

Figure 69. Example of the calculation of the response curve. The experimental data and the fitted curve are shown on the left.

MTF, NPS and DQE can be estimated by using suitable images. MTF can be calculated both with slit camera and edge techniques. Users must just select an ROI over the part of the image which contains the detail useful for estimating the MTF (slit or edge). For estimating NPS, some flood images at the same exposure must be acquired and opened as a stack. The NPS is calculated on windows extracted from the selected ROI. The DQE is finally achieved by selecting properly the X-ray beam used and inserting the correct exposure value. In all cases results are provided in various ways: as graphical plots, as tables, and can be saved as text files.

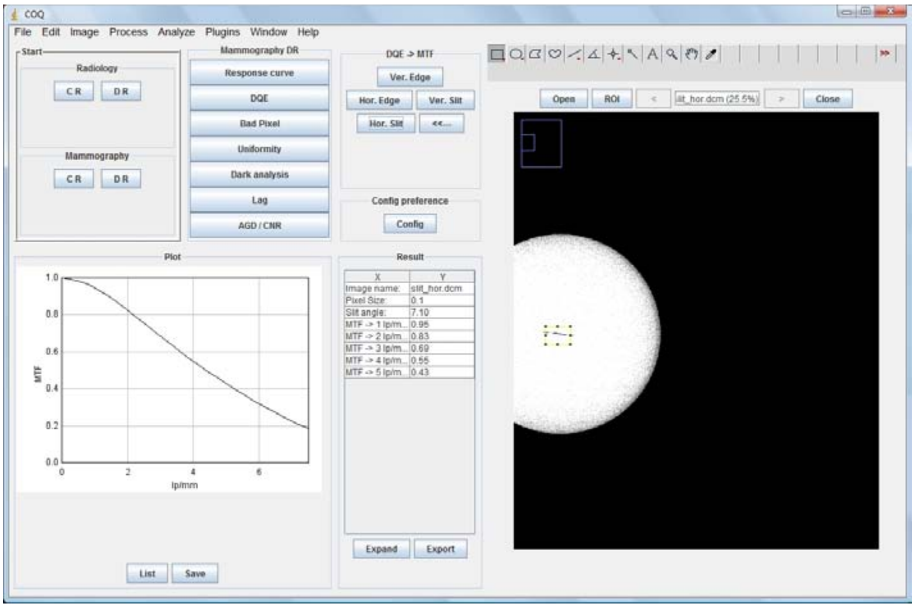

Figure 70. Example of MTF calculation with a slit camera (image on the right), and with the MTF results shown as a plot (MTF curve on the left) and in a textual way.

The set of quality control procedures implemented are basically derived from the IEC standards. The plugin includes the computation of the following features: defective pixel analysis, uniformity (global and local), dark analysis, and lag (multiplicative and additive). The first analysis aims to determine the accuracy of the defective pixels/lines correction in the preprocessing stage. The uniformity test is performed for testing the flat field correction implemented in a digital system. The dark analysis has the purpose of assessing the intrinsic noise of the system. Finally, lag is used for evaluating the artifacts due to previous exposures to the detector. For each of the estimated parameter, a threshold can be set, for assessing whether the system response is acceptable or not. More details about the image quality procedures implemented in the plugin can be found in one of our papers. For mammography we are also finalizing an analysis which aims to correlate image quality to the dose to patient. To this end, we implemented the estimation of the AGD and CNR.

5. CONCLUSIONS

This thesis provides two major results: in the first place a detailed and updated description of the most recent digital detection technologies used in radiological department is presented together with a score of experimental results - both in terms of physical and psychophysical evaluation - from some of the most promising technologies.

In second place many procedures are presented which have been developed to provide, in a simple way, the due technical characterizations through user friendly software tools.

Both results are of great interest in radiological hospital setting for the so-called health technology assessment i.e. in equipment management and optimization and in device acquisition planning.

A very nice quality image:

An interesting mistake…..

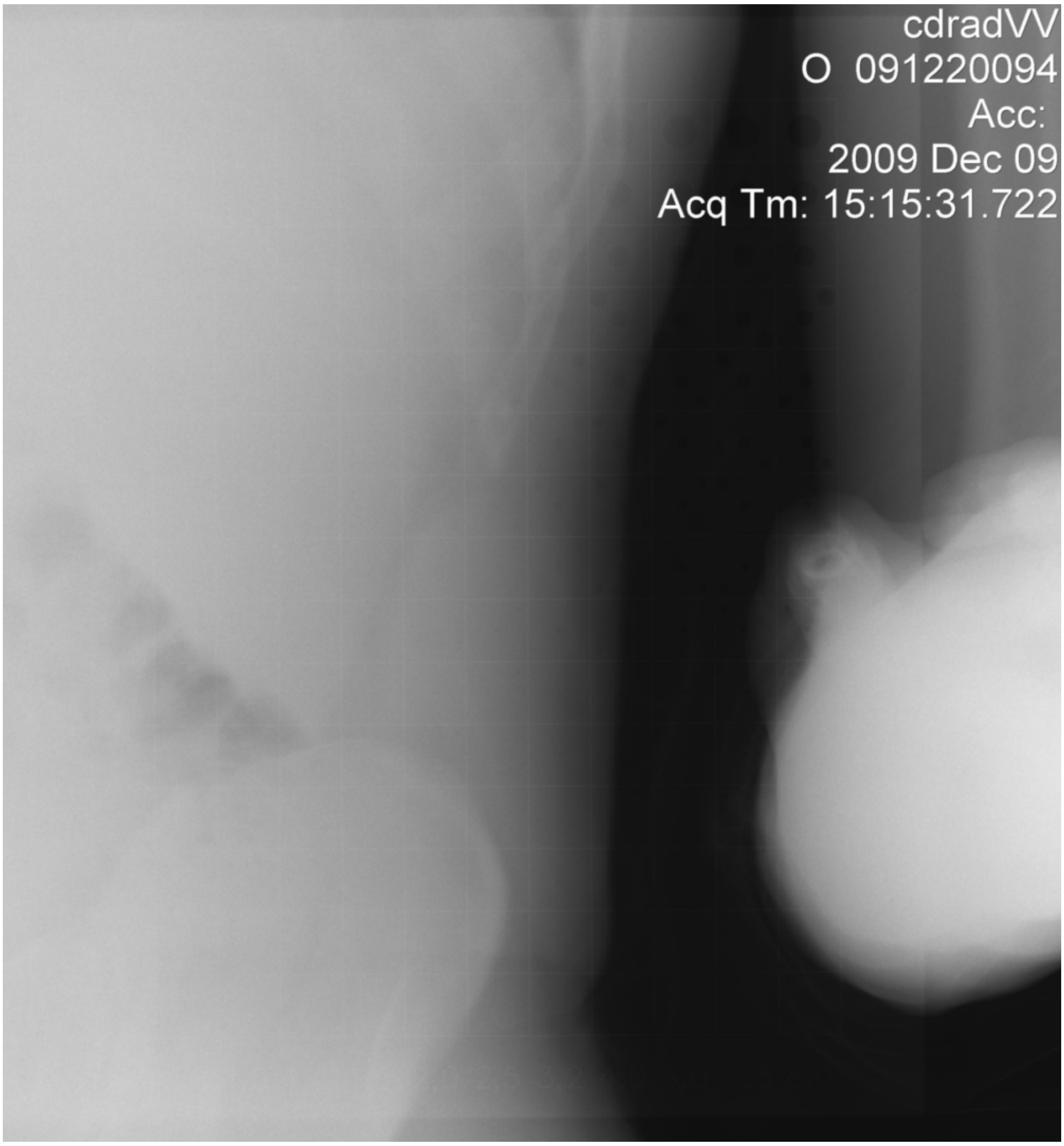

6. REFERENCES

[1] International Electrotechnical Commission, Medical electrical equipment - Characteristics of digital X-ray imaging devices - Part 1-2: Determination of the detective quantum efficiency - Detectors used in mammography (IEC-62220-1-2, Geneva, Switzerland) (2007)

[2] N.T. Ranger, E. Samei, J.T. Dobbins III and C.E. Ravin, "Assessment of detective quantum efficiency: intercomparison of a recently introduced international standard with prior methods", Radiology (243), 785-795 (2007)

[3] L. Lanca, A. Silva, "Digital radiography detectors – A technical overview: part 2" Radiography (15) 134-138 (2009)

[4] H. Roehrig, E. Krupinski, and T. Yu, "Physical and psycho-physical evaluation of digital systems for mammography" Proc. SPIE (2436) 124-134 (1995)

[5] R. Aufrichtig, "Comparison of low contrast detectability between a digital amorphous silicon and a screen-film based imaging system for thoracic radiography" Med. Phys. 26(7) 1349-1358 (1999)

[6] E. D. Pisano and M J. Yaffe, "Digital Mammography", Radiology (234), 353–362 (2005)

[7] Syllabus Advances in Breast Imaging: Physics, Technology, and Clinical Applications Categorical Course in Diagnostic Radiology Physics (2004)

[8] J.A. Rowlands, "The physics of computed radiography," Phys, Med. Biol. (47), R123-R166, (2002)

[9] S. Rivetti, N. Lanconelli, R. Campanini, M. Bertolini, G. Borasi, A. Nitrosi, C. Danielli, L. Angelini and S. Maggi, "Comparison of different commercial FFDM units by means of physical characterization and contrast-detail analysis," Med. Phys. 33 (11), 4198-4209, (2006)

[10] S. Rivetti, B. Canossi, R. Battista, N. Lanconelli, E. Vetruccio, C Danielli, G. Borasi, P. Torricelli "Physical and clinical comparison between a screen-film system and a dual side reading mammography dedicated computed radiography system", Acta Radiol.,(10) 1109-1118, (2009)

[11] K. Takahashi, "Fuji Computed Radiography technical review N° 14: Imaging Plate"

[12] K.A.Fatterly and B. A. Schueler, "Performance evaluation of a dual side read dedicated mammography computed radiography system", Med. Phys. 30 (7), 1843-1854 (2003)

[13] A. Mackenzie and I.D. Honey, "Characterization of noise sources for two generations of computed radiography systems using powder and crystalline photostimulable phosphors," Med. Phys. 34 (8), 3345-3357 (2007)

[14] S. Rivetti, N. Lanconelli, M. Bertolini, G. Borasi, D. Acchiappati and A. Burani, "Comparison of different Computed Radiography systems: physical characterization and contrast detail analysis", Med. Phys. 37 (2), 440-448 (2010)

[15] G. Borasi, A. Nitrosi, P. Ferrari and D. Tassoni, "On site evaluation of three flat panel detectors for digital radiography", Med. Phys, 30(7), 1719-1731 (2003)

[16] J. A. Rowlands and J. Yorkston, "Flat panel detectors for digital radiography", Handbook of Medical Imaging Vol. 1, Ch. 4, edited by J. Beutel, H. L. Kundel and R. L. Van Metter, SPIE Press (2000)

[17] S. Vedantham, A. Karellas, S. Suryanarayanan, D. Albagli, S. Han, E.J. Tkaczyk, C.E. Landberg, B. Opsahl Ong, P.R. Granfors, I. Levis, C.J. D'Orsi and R.E. Hendrick, "Full breast digital mammography with an amorphous silicon-based flat panel detector: Physical characteristics of a clinical prototype", Med. Phys., 27 (3), 558-567 (2000)

[18] C. Ghetti, A. Borrini, O. Ortenzia, R. Rossi and P.L. Ordonez, "Physical characteristics of GE Senographe Essential and DS digital mammography detectors," Med. Phys. 35 (2), 456-463, (2008)

[19] N. Lanconelli, S. Rivetti, P. Golinelli, R. Sansone, M. Bertolini and G. Borasi, "Physical and psychophysical characterization of a GE Senographe DS clinical system," Proc SPIE 6510, 65104K, (2007)

[20] R.S. Saunders Jr, E. Samei, J.L. Jesneck and J.Y. Lo, "Physical characterization of a prototype selenium-based full field digital mammography detector," Med. Phys. 32 (2), 588-599, (2005)

[21] G. Hajdok, J.J. Battista, and I.A. Cunningham, "Fundamental X-ray interaction limits in diagnostic imaging detectors: frequency-dependent Swank noise," Med. Phys. 35 (7), 3194-3204, (2008).

[22] B. Lazzari, G. Belli, C. Gori, and M. Rosselli Del Turco, "Physical characteristics of five clinical systems for digital mammography," Med. Phys. 34 (7), 2730-2743, (2007).

[23] J.A. Rowlands, D.M. Hunter, and N. Araj, "X-ray imaging using amorphous selenium: a photoinduced discharge readout method for digital mammography," Med. Phys. 18 (3), 421-431, (1991).

[24] J.A. Rowlands and J.E. Taylor, "Design of a laser scanner for a digital mammography system," Med. Phys. 23 (5), 755-758, (1996).

[25] N. Rezsnik, P.T. Komljenovic, S. Germann, and J.A. Rowlands, "Digital radiography using amorphous selenium: photoconductively activated switch (PAS) readout system," Med. Phys. 35 (3), 1039-1050, (2008).

[26] G. Pang, W. Zhao, and J. Rowlands, "Digital radiology using active matrix readout of amorphous selenium: geometrical and effective fill factors," Med. Phys. 25 (9), 1636-1646, (1998).

[27] K. Irisawa, K. Yamane, S. Imai, M. Ogawa, T. Shouji, T. Agano, Y. Hosoi and T. Hayakawa, "Direct-conversion 50 μm pixel-pitch detector for digital mammography using amorphous selenium as a photoconductive switching layer for signal charge readout", Proc. SPIE 7258, 72581I (2009)

[28] S. Rivetti, N. Lanconelli, M. Bertolini, G. Borasi, P Golinelli and E. Gallo, “Physical and psychophysical characterization of a novel clinical system for digital mammography”, Med. Phys. 36 (11), 5139-5148 (2009)
[29] G. M. Besson et al., “Design and evaluation of a slot-scanning full-field digital mammography system,” Proc. SPIE 4682, 457–468 (2002)
[30] Z. Jing, W. Huda, J. K. Walker, and W. Y. Choi, “Detective quantum efficiency of a CsI:Tl scintillator based scanning slot X-ray detector for digital mammography,” Proc. SPIE 3336, 583–591 (1998)
[31] J. G. Mainprize, N. L. Ford, S. Yin, T. Tumer, and M. J. Yaffe, “A slot scanned photodiode-array/CCD hybrid detector for digital mammography” Med. Phys. 29 (2) 214-225 (2002)
[32] S. Z. Shen, A. K. Bloomquist, G. E. Mawdsley and M. J. Yaffe, “Effect of scatter and an antiscatter grid on the performance of a slot-scanning digital mammography system” Med. Phys. 33 (4) 1108-1115 (2006)
[33] J. Lai, C. C. Shaw, W. Geiser and Lingyun Chen, “Comparison of slot scanning digital mammography system with full-field digital mammography system” Med. Phys. 35 (6) 2339-2346 (2008)
[34] M. Aslund and B. Cederstrom “Physical characterization of a scanning photon counting digital mammography system based on Si-strip detectors”, Med. Phys. 34 (6),1918-1925 (2007)
[35] Fredenberg, M. Hemmendorff, B. Cederstrom, M Aslund and M. Danielsson, “Contrast-enhanced spectral mammography with a photon-counting detector” Med. Phys. 37 (5) 2017-2029 (2010)
[36] S. R. Amendolia, M. G. Bisogni, P. Delogu, M. E. Fantacci, G. Paternoster, V. Rosso and A. Stefanini, “Characterization of a mammographic system based on single photon counting pixel arrays coupled to GaAs X-ray detectors” Med. Phys. 36 (4) 1330-1339 (2009)
[37] D. M. Marsh, J. F. Malone, “Methods and materials for the measurement of subjective and objective measurements of image quality” Radiat. Prot. Dosimetry (94) 37-42 (2001)
[38] J. T. Dobbins, E. Samei, N. T. Ranger, Y. Chen, “Intercomparison of methods for image quality characterization. II. Noise power spectrum” Med Phys. (33) 1466-1475 (2006)
[39] H. Fujita, K. Doi, and M. L. Giger, “Investigation of basic imaging properties in digital radiography. 6. MTFs of II–TV digital imaging systems” Med. Phys. 12 (6) 713-720 (1985)
[40] R. Shaw, “The equivalent quantum efficiency of the photographic process” J. Photogr. Soc. (11) 199-204 (1963)
[41] International Electrotechnical Commission, Medical electrical equipment - Characteristics of digital X-ray imaging devices - Part 1-2: Determination of the detective quantum efficiency - (IEC-62220, Geneva, Switzerland) (2005)
[42] A. Rose, ‘‘A unified approach to the performance of photographic film, television pickup tubes and the human eye’’ J. Soc. Motion Pict. Eng. 47 273–294 (1946)
[43] A. Rose, ‘‘The sensitivity performance of the human eye on an absolute scale’’ J. Opt. Soc. Am. 38 196-208 (1948)
[44] R. F. Wagner and D. G. Brown, ‘‘Unified SNR analysis of medical imaging systems’’ Phys. Med. Biol. 30 489-518 (1985)
[45] L. Loo, K. Doi, and C. E. Metz, “A comparison of physical image quality indices and observer performance in the radiographic detection of nylon beads” Phys. Med. Biol. 29 837-856 (1984)
[46] E. Burgess, F. L. Jacobson, and P. F. Judy, “Human observer detection experiments with mammograms and power-law noise” Med. Phys. 28 419-437 (2001)
[47] W. E. Smith and H. H. Barrett, “Hotelling trace criterion as a figure of merit for the optimization of imaging systems” J. Opt. Soc. Am. A 3 717-725 (1986)
[48] K. J. Myers and H. H. Barrett, “Addition of a channel mechanism to the ideal observer model” J. Opt. Soc. Am. A 4 2447-2457 (1987)
[49] M. J. Tapiovaara, “SNR and noise measurements for medical imaging: II. Application to fluoroscopic x-ray equipment” Phys. Med. Biol. 38 1761-1788 (1993)
[50] A. Pascoal, C.P. Lawinski, I. Honey, and P. Blake, “Evaluation of a software package for automated quality assessment of contrast detail images - comparison with subjective visual assessment,” Phys. Med. Biol. 50, 5743-5757 (2005)
[51] A. Nitrosi, M. Bertolini, G. Borasi, A. Botti, A. Barani, S. Rivetti, and L. Pierotti, “Application of QC_DR Software for Acceptance Testing and Routine Quality Control of Direct Digital Radiography Systems: Initial Experiences using the Italian Association of Physicist in Medicine Quality Control Protocol,” J Digit Imaging (doi: 10.1007/s10278-008-9150-z) (2009)
[52] N. Karssemeijer and M. A. O. Thijssen, “Determination of contrast-detail curves of mammography systems by automated image analysis,” Proceedings of the IWDM (Elsevier, New York, 1996), pp. 155–160 (1996)
[53] N.W. Marshall, “A comparison between objective and subjective image quality measurements for a full-field digital mammography system,” Phys. Med. Biol., 51, 2441-2463 (2006).
[54] M. J. Tapiovaara, and M. Sandborg, “How should low-contrast detail detectability be measured in fluoroscopy” Med. Phys 31 2564-2576 (2004)
[55] CE Metz “Basic principles of ROC analysis”. Semin Nucl Med;8:283–98 (1978)
[56] Wald A. Statistical decision functions. New York: Wiley; (1950)

[57] JA Swets. “ROC analysis applied to the evaluation of medical imaging techniques”. Invest Radiol.;14:109–21 (1979)
[58] DA Turner “An intuitive approach to receiver operating chararcteristic curve analysis” J Nucl Med.;19:213–20 (1978)
[59] CE Metz “Quantification of failure to demonstrate statistical significance: the usefulness of confidence intervals” Invest Radiol.;28:59–63 (1993)
[60] Obuchowski, NA: Research activities: ROC analysis. (http://www.bio.ri.ccf.org/html/rocanalysis.html)
[61] E. Samei, M.J. Flynn, and D.A. Reimann, “A method for measuring the presampled MTF of digital radiographic systems using an edge test device,” Med. Phys. 25, 102-113 (1998).
[62] U. Neitzel, S. Günther-Kohfahl, G. Borasi, and E. Samei, “Determination of the detective quantum efficiency of a digital x-ray detector: Comparison of three evaluations using a common image data set,” Med. Phys. 31, 2205-2211 (2004).
[63] E. Samei and M.J. Flynn, “An experimental comparison of detector performance for computer radiography systems,” Med. Phys. 29 (4), 447-459 (2002).
[64] L. Riccardi, M.C. Cauzzo, R. Fabbris, E. Tonini, and R. Righetto, “Comparison between a built-in “dual side” chest imaging device and a standard “single side” CR,” Med. Phys. 34, 119-126 (2007).
[65] P. Monnin, Z. Holzer, R. Wolf, U. Neitzel, P. Vock, F. Gudinchet, and F.R. Verdun, “An image quality comparison of standard and dual-side read CR systems for pediatric radiology,” Med. Phys. 33, 411-420 (2006).
[66] K.A. Fetterly and B.A. Schueler, “Performance evaluation of a computed radiography imaging device using a typical “front side” and novel “dual side” readout storage phosphors,” Med. Phys. 33, 290-296 (2006)
[67] K. Shimada, H. Yasuda, S. Arakawa, T. Kuwabara, A. Takasu, Y. Iwabuchi, and M. Katou, “Comparison in image quality and noise component of columnar phosphor plate and powder phosphor plate,” Proc. SPIE 6510, 651044 (2007).
[68] S. Wirth, M. Treitl, M.F. Reiser, and M. Körner, “Imaging Performance with Different Doses in Skeletal Radiography: Comparison of a Needle-structured and a Conventional Storage Phosphor System with a Flat-Panel Detector,” Radiology 250, 152-160 (2009).
[69] P. Monnin, D. Gutierrez, S. Bulling, D. Lepori. J.F. Valley, and F.R. Verdun, “Performance comparison of an active matrix flat panel imager, computed radiography system, and a screen-film system at four standard radiation qualities,” Med. Phys. 32, 343-350 (2005).
[70] Borasi, E. Samei, M. Bertolini, A. Nitrosi, and D. Tassoni, “Contrast-detail analysis of three flat panel detectors for digital radiography,” Med. Phys. 33, 1707-1719 (2006).
[71] J.M. Fernandez, J.M. Ordiales, E. Guibelalde, C. Prieto, and E. Vano, “Physical image quality comparison of four types of digital detector for chest radiology,” Radiat. Prot. Dosimetry. 129, 140-143 (2008)
[72] M. Körner, M. Treitl, R. Schaetzing, K.J. Pfeifer, M. Reiser, and S. Wirth, “Depiction of low-contrast detail in digital radiography: comparison of powder- and needle-structured storage phosphor systems,” Invest Radiol.41, 593-599 (2006)
[73] E. Samei and M.J. Flynn, “An experimental comparison of detector performance for direct and indirect digital radiography systems,” Med. Phys. 30 (4), 608-622 (2003)
[74] K. Bacher, P. Smeets, L. Vereecken, An De Hauwere, P. Duyck, R. De Man, K. Verstraete, H. Thierens, “Image Quality and Radiation Dose on Digital Chest Imaging: Comparison of Amorphous Silicon and Amorphous Selenium Flat-Panel Systems,” AJR 187 (3), 630-637 (2006)
[75] F. Nariyuki, S. Imai, H. Watano, T. Nabeta, and Y. Hosoi, “New development of large-area direct conversion detector for digital radiography using amorphous selenium with a C60-doped polymer layer,” Proc. SPIE 7622, 762240-762240-7 (2010)
[76] International Electrotechnical Commission, “Medical diagnostic x-ray equipment–Radiation conditions for use in the determination of characteristics,” IEC-61267, Geneva, Switzerland (2003)
[77] A.E. Burgess, “The Rose model, revisited,” J. Opt. Soc. Am A. 16, 633-646 (1999)
[78] P. Monnin, D. Gutierrez, S. Bulling, D. Lepori. J.F. Valley, and F.R. Verdun, “Performance comparison of an active matrix flat panel imager, computed radiography system, and a screen-film system at four standard radiation qualities,” Med. Phys. 32, 343-350 (2005)
[79] Roehrig, E. Krupinski, and T. Yu, "Physical and psycho-physical evaluation of digital systems for mammography" Proc. SPIE (2436) 124-134 (1995)
[80] K.W. Jee, L. E. Antonuk, Y. El-Mohri, and Q.H. Zhao, “System performance of a prototype flat-panel imager operated under mammographic conditions,” Med. Phys. 30, 1874-1890 (2003).
[81] N. Lanconelli, S. Rivetti, P. Golinelli, M. Serafini, M. Bertolini, and G. Borasi, “Comparison of human observers and CDCOM software reading for CDMAM images,” Proc SPIE 6515, 65150E, (2007).
[82] G. Hajdok, J.J. Battista, and I.A. Cunningham, “Fundamental x-ray interaction limits in diagnostic imaging detectors: Frequency-dependent Swank noise”, Med. Phys. 35, 3194-3204 (2008).
[83] P. Bernhardt, T. Mertelmeier, and M. Hoheisel, “X-ray spectrum optimization of full-field digital mammography: Simulation and phantom study”, Med. Phys. 33, 4337-4349 (2006).
[84] J.M. Oduko, K.C. Young, O. Gundogdu, and A. Alsager, “Effect of Using Tungsten-Anode X-Ray Tubes on Dose and Image Quality in Full-Field Digital Mammography”, Lect. Notes Comput. Sc. 5116, 522-529 (2008).

[85] P. Baldelli, N. Phelan, and G. Egan, "Effect of Anode/Filter Combination on the Dose and Image Quality of a Digital Mammography System Based on an a-Se Detector", Lect. Notes Comput. Sc. 5116, 716-723 (2008).
[86] P. Monnin, D. Gutierrez, S. Bulling, D. Guntern, and F.R. Verdun, "A comparison of the performance of digital mammography systems," Med. Phys. 34 (3), 906-914, (2007).
[87] R.S. Saunders Jr., J.A. Baker, D.M. Delong, J.P. Johnson, and E. Samei, "Does image quality matter? Impact of resolution and noise on mammographic task performance," Med. Phys. 34 (10), 3971-3981, (2007).
[88] Van Ongeval et Al, "Evaluation of the diagnostic value of a CR system by comparison of hard copy images with SFM: results of a prospective clinical trial" Eur Radiol, 16: 1360–1366, (2006).
[89] M aumlhringer, S Reineck, A Perniok, K Kruumlger, Andermahr J, Rubbert A, et al. "Digital amorphous silicon flat-panel detector radiography at different exposure doses versus mammography film: possibility of radiation dose reduction in detecting rheumatologic bone defects. Acta Radiol ;49:157–66 (2008)
[90] F R Verdun, M Pachoud, P Bergmann, Buhr "Assessment of radiographic screen-film systems: a comparison between the use of a microdensitometer and a film digitizer" Radiat Prot Dosimetry 114:208–13 (2005)
[91] G. Borasi et Al."Valutazione della qualità di sistemi radiografici schermo-pellicola: principi fisici e metodi di misura" Radiol Med;32:807–14 (1990)
[92] BJ McParland, MM Boyd, K.Al Yousef "Optimizing optical density of a Kodak mammography film-screen combination with standard-cycle processing" Br J Radiol;71:950–3 (1998)
[93] G Gennaro , C di Maggio "Dose comparison between screen/film and full-field digital mammography". Eur Radiol;16:2559–66 (2006)
[94] U Fischer, KP Hermann, F Baum "Digital mammography: current state and future aspects" Eur Radiol;16:38–44 (2006)
[95] T Svahn, B Hemdal, M Ruschin, DP Chakraborty, I Andersson et Al. "Dose reduction and its influence on diagnostic accuracy and radiation risk in digital mammography: an observer performance study using an anthropomorphic breast phantom". Br J Radiol;80:557–62 (2007)
[96] Suryanarayanan S, Karellas A, Vedantham S, Ved H, 16. Baker SP, d'orsi cJ. Flat-panel digital mammography systems: contrast-detail comparison between screen-film radiographs and hard-copy images. Radiology;225:801–7 (2002)
[97] E. Metz "ROC methodology in radiologic imaging" Invest Radiol;21:720–3, (1986)
[98] KP Herman, S Obenauer, A Zach-Enk, grabbe E. "A new CR based system for high resolution mammography: experi-mental analysis of low contrast detectability" in: Peitgen Ho, editor. digital mammography: IWDM 2002 – 6th inter-national Workshop on digital Mammography; 2002 June 22–25; Bremen, germany. Berlin: Springer; p. 111–3 (2003)
[99] RE Van Engen, WJH Veldkamp, lJ Ostveen, M Thijssen, N Karssemeijer "Image quality of a dual side reading Fuji computed mammography system compared to the GE FFDM system and a film/screen mammography system" Peitgen Ho, editor. Digital Mammography: IWDM 2002 – 6th inter-national Workshop on digital Mammography; 2002 June 22–25; Bremen: Springer; p. 155–7 (2003)
[100] D.R. Dance, C.L. Skinner, K.C. Young, J.R. Beckett, C.J. Kotre, "Additional factors for the estimation of mean glandular breast dose using the UK mammography dosimetry protocol", Phys Med Biol 45, 3225–3240 (2000)
[101] K Young, H Bosmans, M Thijssen. "The European protocol for the quality control of the physical and technical aspects of mammography screening. in: European guidelines for breast cancer screening. Fourth edition. Luxembourg: European commission; (2006).
[102] B Heddson, K Rönnow, M Olsson, D Miller "Digital versus screen-film mammography: A retrospective comparison in a population-based screening program" Eur J Radiol; 64:419-25 (2007).
[103] R Bonardi, D Ambrogetti, S Ciatto, E Gentile, B Lazzari, P Mantellini, et al. "Conventional versus digital mammography in the analysis of screen-detected lesions with low positive predictive value". Eur J Radiol; 5:258-63 (2005)
[104] Young KC, Cook JH, Oduko JM, Bosmans H. "Comparison of software and human observers in reading images of the CDMAM test object to assess digital mammography systems". In: Flynn MJ, Hsieh J, editors. Medical Imaging 2006 Proc. SPIE, Vol. 6142, 614206 (2006)
[105] S Obenauer , Hermann KP, Schorn C, Fischer U, Grabbe E. "Full-field digital mammography: dose-dependent detectability of breast lesions and microcalcinosis". Rofo; 172:1052-6 (2000)
[106] KP Hermann, Obenauer S, Marten K, Kehbel S, Fischer U, Grabbe E. Average glandular dose with amorphous silicon full-field digital mammography: clinical results. Rofo; 174:696-9 (2002)
[107] KC Young, Oduko JM, Bosmans H, Nijs K, Martinez L. "Optimal beam quality selection in digital mammography" Br J Radiol; 79:981-990 (2006)
[108] K Satoh, Kuwabara T, Yasuda H, Arakawa S. Optimization of image quality and average glandular dose in CR mammography, In: Hsieh J, Flynn MJ, editors. Medical Imaging 2007: Physics of Medical Imaging; 2007 Feb 17-22; San Diego, CA, USA. Proc. SPIE, Vol. 6510, 65104H (2007)
[109] S Rivetti, N Lanconelli, "Contrast detail performance analysis in medical displays", Hospital Imaging & Radiology Europe Vol 5 No 2 - Summer (2010)
[110] http://www.aapm.org/

[111] ACR, “Practice guideline for determinants of image quality in digital mammography”, Res. 35 (2007) (http://www.acr.org/)
[112] EUREF, “European guidelines for quality assurance in breast cancer screening and diagnosis. Fourth Edition”, EUREF (2006) (http://www.euref.org/)
[113] K. Bloomquist, M. J. Yaffe, E. D. Pisano, R. E. Hendrick, G. E. Mawdsley, S. Bright, S. Z. Shen , M. Mahesh, E. L. Nickoloff, R. C. Fleischman, M. B. Williams, A. D. A. Maidment, D. J. Beideck, J. Och, J. A. Seibert, “Quality control for digital mammography in the ACRIN DMIST trial: Part I”, Med. Phys. 33 (3) 719-736 (2006)
[114] M. J. Yaffe, A. K. Bloomquist, G. E. Mawdsley, E. D. Pisano, R. E. Hendrick, L. L. Fajardo, J. M. Boone, K. Kanal, M. Mahesh, R. C. Fleischman, J. Och, M. B. Williams, D. J. Beideck, A. D. A. Maidment, “Quality control for digital mammography: Part II recommendations from the ACRIN DMIST trial”, Med. Phys. 33 (3) 737-752 (2006)
[115] G Gennaro, F Ferro, G Contento, F Fornasin and C di Maggio, “Automated analysis of phantom images for the evaluation of long-term reproducibility in digital mammography”, Phys. Med. Biol. (52) 1387–1407 (2007)
[116] M. Boone, T. R. Fewell, R. J. Jennings, “Molybdenum, rhodium, and tungsten anode spectral models using interpolating polynomials with application to mammography”, Med. Phys. 24 (12) 1863-1874 (1997)
[117] A. Okunade, “Method for the evaluation of a average glandular dose in mammography”, Med. Phys. 33 (4) 1153-1164 (2006)
[118] G. Gennaro and C. di Maggio, “Dose comparison between screen/film and full-field digital mammography”, Eur Radiol 16: 2559–2566(2006)
[119] http://rsb.info.nih.gov/ij/